DOTTORATO DI RICERCA IN CHIMICA

Convenzione tra

UNIVERSITÀ DEGLI STUDI DI TRIESTE

e

UNIVERSITÀ CA' FOSCARI DI VENEZIA

CICLO XXX

ULTRAFINE PARTICLES IN WORKING ENVIRONMENT AND AMBIENT AIR: REAL-TIME MEASUREMENTS, CHARACTERIZATION AND EVALUATION OF EXPOSURE ROUTES

Settore scientifico-disciplinare: **CHIM/01**

DOTTORANDA
ELENA BARACCHINI

COORDINATORE
PROF. MAURO STENER

SUPERVISORE DI TESI
PROF. GIANPIERO ADAMI

ANNO ACCADEMICO 2016/2017

Table of contents

SECTION 1

SECTION 3

Abstract

Ultrafine particles (UFPs) are released in ambient air from natural and anthropogenic sources, but certain workplace conditions are responsible for the unintentional emission of this kind of particles as well.

The small size and corresponding large specific surface area of UFPs and nanoparticles (NPs) are responsible for the great biological activity per given mass. Other specific characteristics of UFPs such as number concentration, shape, agglomeration state and chemical composition play an important role in determining toxicity and reactivity. Even though UFPs represent a major concern in terms of human exposure, at the moment there is no legal threshold for controlling them in ambient air, while there are some guidelines regarding workplaces.

The aim of this thesis is to measure and characterise UFPs that can be found in working environments and ambient air and, afterwards, explore possible exposure routes.

UFPs emissions from three kinds of industrial processes were investigated in real working conditions by means of real-time measurements of number concentration and size, morpho-chemical characterisation and quantitative analysis of metals in airborne and deposited particles.

We demonstrated that iron/manganese oxide nanoparticles are the most representative particles released during steel automatic gas tungsten arc welding (GTAW).

Moreover, despite respecting the American Conference of Governmental Industrial Hygienists (ACGIH) limits for respirable aluminium, we found that oxy-fuel welding and the die casting production cycle of aluminium-based products involve the release of UFPs

with a chemical composition coherent with the raw materials. From our findings surfaces and skin contamination seems to be a secondary source of exposure to UFPs, suggesting a possible increased risk in workers mainly for inhalation exposure.

Regarding the evaluation of the presence of UFPs in ambient air, a study was performed in proximity of an industrial "hot spot" in Servola district in Trieste where an integral cycle steel plant is located. Particle number concentration (PNC) in the range 10-300 nm in "Servola" site was about twice higher than "background" values. Moreover, an increase of PNC corresponding to a decrease of the particle size and vice versa was observed. In the particulate matter, agglomerates of nanoparticles containing Fe, Zn and Mn were observed by means of a transmission electron microscope coupled with an energy-dispersive X-ray analytical system (TEM-EDS). The contribution of Fe concentration in the PM_1 and, in particular, in the particle fraction below 250 nm seems to be not negligible. This result is highly significant from a toxicological point of view. Servola district is densely inhabited and people live very close to the integrated steel plant that is a relevant emission source.

Afterwards, nanoparticles compatible with those found in the aforementioned studies were tested *in vitro* using the method of static Franz diffusion cells in order to explore possible exposure routes. In particular, dermal and meningeal absorption of Al_2O_3NPs and $MnFe_2O_4$NPs respectively were investigated leaning, in both cases, towards a reassuring absorption profile in physiological conditions.

Riassunto

Le particelle ultrafini (UFPs) sono rilasciate in aria ambiente da fonti naturali e antropiche, ma anche alcune attività lavorative sono responsabili dell'emissione accidentale di questo tipo di particelle.

Le piccole dimensioni e la corrispondente elevata area superficiale delle UFPs e delle nanoparticelle (NP) sono responsabili della loro rilevante attività biologica. Altre caratteristiche specifiche delle UFP come la concentrazione in numero, la forma, lo stato di agglomerazione e la composizione chimica svolgono un ruolo importante nel determinarne la tossicità e la reattività. Anche se le UFPs rappresentano una delle maggiori preoccupazioni in termini di esposizione umana, attualmente non esistono limiti di legge per il loro monitoraggio in aria ambiente, mentre sono previste solo alcune linee guida in ambito occupazionale.

Lo scopo di questa tesi è misurare e caratterizzare le UFPs presenti in aria ambiente e in alcuni contesti lavorativi e, successivamente, valutare possibili vie di esposizione.

Sono state studiate, in condizioni di lavoro reali, le emissioni di UFPs da tre tipi di processi industriali eseguendo misurazioni in tempo reale della concentrazione in numero e delle dimensioni, caratterizzazione morfologica e chimica e analisi quantitativa dei metalli presenti nelle particelle aerodisperse e depositate.

Abbiamo dimostrato che le nanoparticelle costituite da ossido di ferro/manganese sono le particelle più rappresentative tra quelle rilasciate durante il processo automatico di saldatura dell'acciaio con tecnica di saldatura ad arco con elettrodo di tungsteno sotto protezione di gas inerte (GTAW).

Inoltre, nonostante i limiti previsti dall'American Conference of Governmental Industrial Hygienists (ACGIH) per l'alluminio contenuto in polveri respirabili, abbiamo evidenziato che, nell'ambito della produzione di prodotti a base di alluminio, il processo di saldatura a fiamma O_2-GPL e il processo di pressofusione sono responsabili dell'emissione di UFPs con una composizione chimica coerente con quella dei materiali di base.

In base ai risultati ottenuti, la contaminazione delle superfici di lavoro e della cute dei lavoratori sembra essere una fonte secondaria di esposizione alle UFPs, suggerendo un possibile aumento del rischio di esposizione nei lavoratori principalmente per via inalatoria.

Per quanto riguarda la valutazione della presenza di UFPs in aria ambiente, è stato effettuato uno studio in prossimità di un "hot spot" industriale nel rione di Servola, a Trieste, dove è situato un impianto di produzione di ghisa a ciclo integrato. È stato evidenziato che la concentrazione in numero di particelle (PNC) nell'intervallo 10-300 nm nel sito "Servola" era circa il doppio rispetto ai valori di "fondo". Inoltre, è stato osservato un aumento in termini di PNC corrispondente ad una diminuzione della dimensione delle particelle e viceversa. Utilizzando la tecnica di microscopia elettronica a trasmissione accoppiata ad un rivelatore a dispersione di energia (TEM-EDS), nel particolato sono stati osservati agglomerati di nanoparticelle contenenti Fe, Zn e Mn.

Il contributo della concentrazione di Fe nel PM_1 e, in particolare, nella frazione di particelle con dimensioni inferiori ai 250 nm, sembra non essere trascurabile. Questo risultato è altamente significativo dal punto di vista tossicologico. Il rione di Servola è densamente popolato e le persone vivono molto vicino all'impianto siderurgico.

Successivamente, nanoparticelle con caratteristiche compatibili con quelle trovate negli studi precedentemente citati, sono state testate *in vitro* usando il metodo delle celle di diffusione di Franz per valutare possibili vie di esposizione. In particolare è stato studiato l'assorbimento cutaneo di nanoparticelle di Al_2O_3 e l'assorbimento attraverso le meningi di nanoparticelle di $MnFe_2O_4$. In entrambi i casi è stato evidenziato un rassicurante profilo di assorbimento in condizioni fisiologiche.

1. Introduction

The term “ultrafine particles” (UFPs) has been traditionally used to describe nanometre-size (< 100 nm) airborne particles that have not been intentionally produced but are the incidental products of natural and anthropogenic processes (Gwinn and Vallyathan, 2006). On the contrary the term “nanoparticles” (NPs) is used to describe nanometre-size engineered particles intentionally produced for various applications. Major differences between ambient UFPs and NPs are the polydisperse nature of the former versus the monodisperse size of the latter, and particle morphology.

1.1 Toxicology of UFPs

The small size and corresponding large specific surface area of UFPs and NPs are responsible for the greater biological activity per given mass compared with larger particles of the same chemistry. This increased biologic activity can be either positive and desirable (e.g., antioxidant activity, carrier capacity for therapeutics, penetration of cellular barriers for drug delivery) or negative and undesirable (e.g., toxicity, induction of oxidative stress or of cellular dysfunction), or a mix of both (Oberdörster et al., 2005). In these terms the same properties that make NPs so attractive for development in nanomedicine and for specific technological applications become a risk factor when NPs interact with cells.

Size, shape, agglomeration state, crystallinity, surface characteristics, inner structure, chemical composition, biopersistence and dose all play an important role in determining toxicity and reactivity (Maynard and Aitken, 2007). The toxicity and adverse health

effects caused by UFPs are heterogeneous and strongly dependent on the sources (Gwinn and Vallyathan, 2006). *In vitro* and *in vivo* studies using concentrated ambient particles (CAPs) and laboratory-made NPs with various chemistries and particle size have shown to create reactive oxygen species (ROS) that are major contributing factor in inflammation and toxicity (Gwinn and Vallyathan, 2006). The exact mechanism by which NPs create ROS is not fully understood yet (Oberdörster et al., 2005). Particle-bound metals may be responsible for production and release of $^{\cdot}OH$ radicals by Fenton-like reactions directly or after cellular reduction. Moreover, the ability of UFPs to localize in mitochondria, redox active organelles, may be linked to the alteration in ROS production interfering with antioxidant defences (Li et al., 2003).

Cytotoxicity was examined for surrogate, manufactured nanoparticulate materials including commercial multi-walled carbon nanotubes (MWCNTs), black carbon (BC) and nano-particulate matter oxides (TiO_2, Al_2O_3 and Fe_2O_3), since all of them are observed in outdoor environment. They were observed to be variously cytotoxic, with cytokine (IL-8) release and ROS production (Murr and Garza, 2009).

1.2 Human exposure

UFPs are released in ambient air from natural and anthropogenic sources but certain workplace conditions generate NPs as well. Even very low concentrations of nanosized materials in the air represent very high particle number concentrations, that is a major concern in terms of human exposure.

Several epidemiologic studies have found associations of ambient UFPs with adverse respiratory and cardiovascular effects resulting in morbidity and mortality in susceptible parts of the population (Oberdörster et al., 2005). Inhalation may be the major route of exposure for NPs, yet ingestion and dermal exposures also need to be considered during manufacture, use, and disposal of engineered nanomaterials.

1.2.1 Exposure routes

Portal-of-entry–specific defence mechanisms protect the mammalian organism from harmful materials but these defences may not always be as effective for NPs.

With respect to NPs, exposure routes are extensively discussed in Oberdörster et al. (2005) and references therein.

1.2.1.1 Respiratory tract

There are significant differences between NPs and larger particles regarding their behaviour during deposition and clearance in the respiratory tract.

The fractional deposition of inhaled particles in the three regions of the human respiratory tract (nasopharyngeal, tracheobronchial and alveolar) is reported in Fig.1. This is a model that applies to particles that are inhaled as single particles of a given size and not as aggregates. In each of the three regions significant amounts of a certain size of NPs (1–100 nm) are deposited.

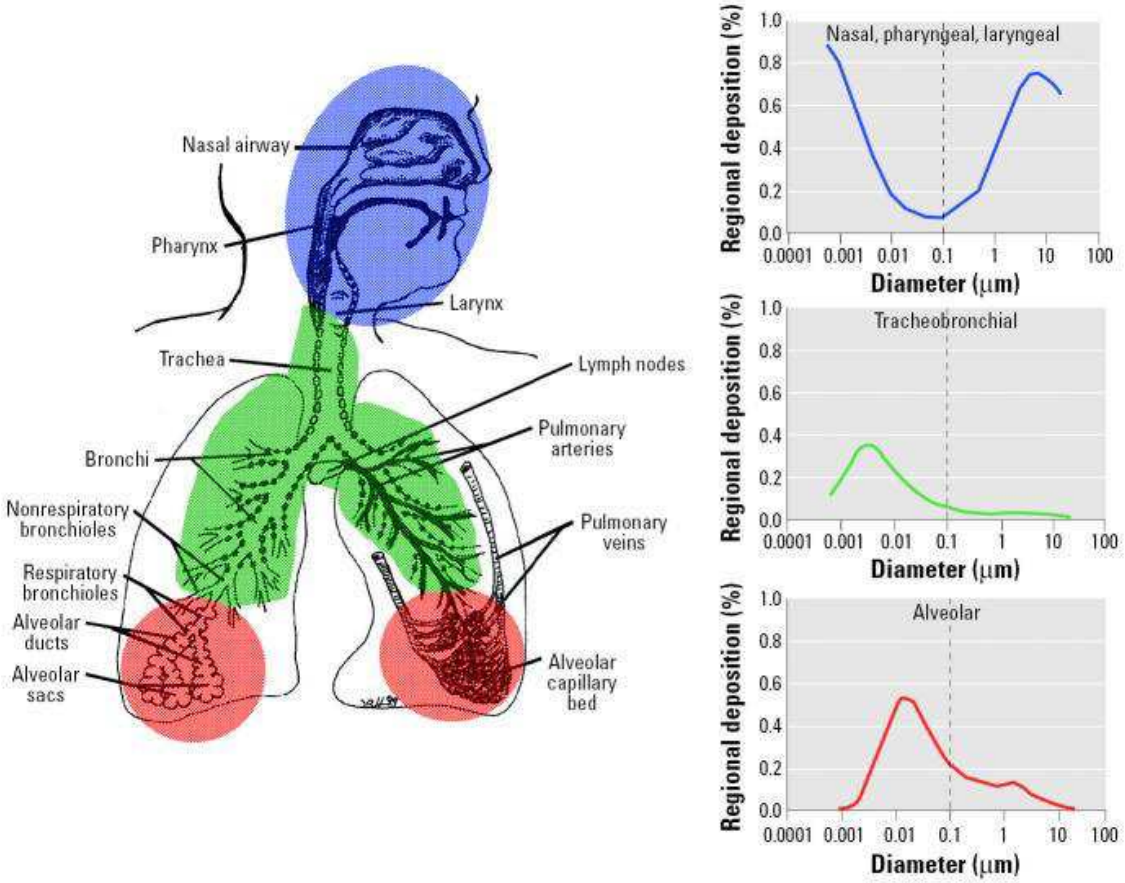

Figure 1 Fractional deposition of inhaled particles in the three regions of the human respiratory tract (Oberdörster et al.,2005).

After the deposition in the respiratory tract, NPs are able to escape specific surveillance mechanisms such as the clearance by alveolar macrophages through phagocytosis. In this way, deposited NPs readily translocate via transcytosis across epithelia into the interstitium and access to the blood circulation directly or via lymphatics reaching other target organs.

The extent of extrapulmonary translocation strongly depends on particle surface characteristics and chemistry, in addition to particle size. Translocation to the blood circulation could provide a mechanism for a direct particle effect on the cardiovascular

system as an explanation for epidemiologic findings of cardiovascular effects associated with inhaled ambient UFPs. Distribution to the heart, kidneys, liver, spleen, bone marrow and other target organs has been reported.

Another translocation pathway for NPs in the respiratory tract involves their uptake by sensory nerve endings embedded in airway epithelia, followed by axonal translocation to ganglionic and central nervous system (CNS) structures. Studies revealed that the olfactory nerve and olfactory bulb (see Fig.2) are indeed portals of entry to the CNS for intranasally instilled nanosized particles such as MnO_2 NPs. Collectively, these kinds of studies have pointed out that the olfactory nerve pathway should also be considered a portal of entry to the CNS for humans under conditions of environmental and occupational exposures to airborne NPs.

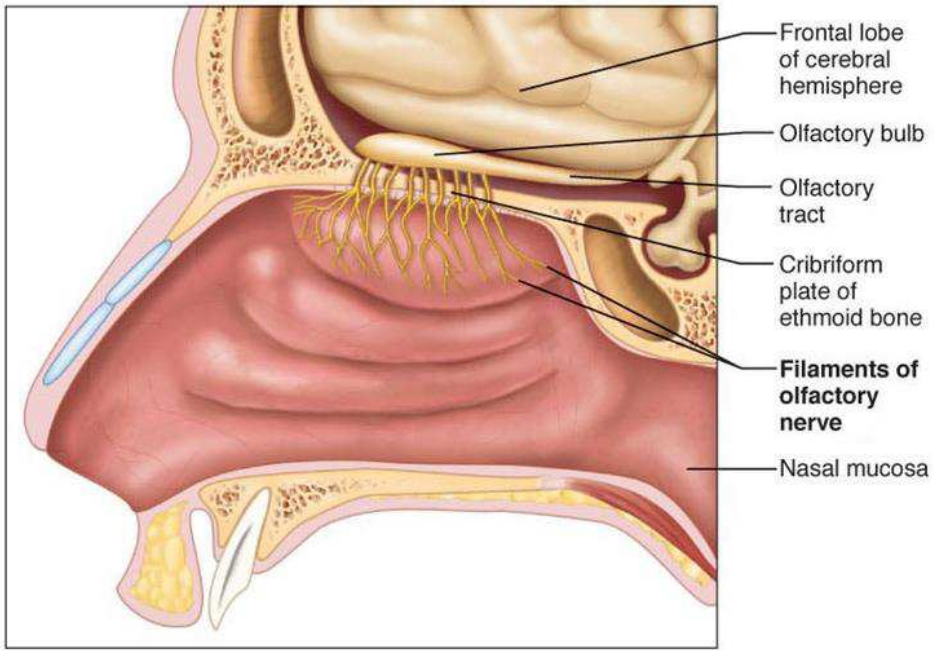

Figure 2 Representation of the connection between the nasal mucosa and the CNS.

1.2.1.2 Gastrointestinal tract

NPs cleared from the respiratory tract via the mucociliary escalator can subsequently be ingested into the gastrointestinal (GI) tract. Alternatively, nanomaterials can be directly ingested, for example if contained in food or water or if used in cosmetics or as drugs or drug delivery devices. When ingested, systemic uptake via lymph into the organism can occur, but most are excreted via feces.

1.2.1.3 Skin

The skin can be divided into three main components: the stratum corneum (SC), the epidermis and the dermis. The SC is responsible for two of the major functions of the skin: it forms the main permeability barrier and maintains water homeostasis. The epidermis has a thickness of typically 50–150 μm and is principally constituted of keratinocytes which differentiate as they migrate toward the SC. The dermis, with a thickness of 600–3000 μm, is a strong connective tissue, mostly comprised of collagen, with a variety of specialized structures (Rawlings et al., 1994).

Percutaneous absorption describes the transport of chemicals from the outer surface of the skin both into the skin and into systemic circulation (EHC 235, 2006). This is often divided into:

• penetration that is the entry of a substance into a particular layer or structure, such as the entrance of a compound into the stratum corneum;

• permeation that is the penetration through one layer into a second layer that is both functionally and structurally different from the first layer;

• absorption that is the uptake of a substance into the skin lymph and local vascular system and in most cases will lead to entry into the systemic circulation (systemic absorption).

The SC represents the main physical barrier for any substance permeating throughout the skin. This means that passing the SC represents the rate limiting step for the diffusion process. It is thought that the permeation through the SC occurs mainly by passive diffusion. Nanoparticles are thought to penetrate the skin through two possible routes: the intercellular route, following the lipid channels between the corneocytes to deeper skin layers and the appendage route (hair follicles, sweat glands).

Skin uptake of nanoparticles could lead to systemic absorption and adverse health effects.

The percutaneous uptake of different kinds of nanoparticles has been evaluated both *in vitro* and *in vivo* mostly in case of intact human skin (Baroli, 2010; Labouta et al., 2013). Due to the great number of variables affecting dermal absorption of nanoparticles, the data found in literature are often contradictory.

One main difference should be made between metal and non-metal NPs. Both kinds have a secondary NPs size which is given after interaction in physiological media, and allows a size-dependent skin penetration: NPs ≤ 4 nm can penetrate and permeate intact skin, NPs size between 4 and 20 nm can potentially permeate intact and damaged skin, NPs size between 21 and 45 nm can penetrate and permeate only damaged skin, NPs size > 45 nm cannot penetrate nor permeate the skin. Other aspects play an important role, mostly for metal NPs, i.e. dissolution in physiological media, which can cause local and systemic effects, the sensitising or toxic potential and the tendency to create aggregates (Larese Filon et al., 2015). An extensive review of literature on nanoparticles dermal absorption was made by Crosera and coworkers (2009).

1.3 Risk assessment and regulations

In order to perform a scientifically based risk assessment and then establish justifiable procedures for risk management, it is necessary to characterise human exposures in terms of physicochemical nature, aggregation state, and concentration (number, mass, surface area) of engineered nanomaterials and perform *in vivo* and *in vitro* studies accordingly. In *in vivo* studies a large range of doses, which include expected realistic exposures and worst-case scenarios, needs to be considered.

On the other hand, the interpretation of the *in vitro* studies is often difficult because particles of different chemical compositions are tested on different target cells, with different dose levels and end points.

What is the suitable metric to quantify human exposure is still an issue. Some studies have shown that particle surface area and number concentrations appear to be better predictors for NPs-induced inflammatory and oxidative stress responses. Moreover, on the basis of what said before, also size, shape, agglomeration state, crystallinity, surface characteristics, inner structure, chemical composition, biopersistence and dose play an important role in determining toxicity and reactivity.

Therefore determining the size-resolved chemical composition of particles is crucial in quantifying their potential deleterious effects on human health.

Currently there is no legal threshold for controlling number concentrations of UFPs in ambient air, just some guidelines for workplace air. Present mass-based regulations for atmospheric particulate matter are insufficient for their control (Kumar et al., 2010). Nevertheless, it is acknowledged that mass based particle concentration limits do not effectively control the smaller particles (Oberdörster et al., 2005).

2. Aim of the thesis

Ultrafine particles are released in ambient air from natural and anthropogenic sources but also certain workplace conditions are responsible for the unintentional emission of this kind of particles.

Even very low concentrations of nanosized particles in the air represent very high particle number concentrations that is a major concern in terms of human exposure.

The small size and corresponding large specific surface area of UFPs and NPs are responsible for the great biological activity per given mass. Other specific characteristics of UFPs such as shape, number concentration, agglomeration state and chemical composition play an important role in determining toxicity and reactivity (Maynard and Aitken, 2007).

The aim of this thesis is to measure and characterise UFPs that can be found in working environments and ambient air and, afterwards, explore possible exposure routes. This can help to enhance knowledge on diseases that may be related to this kind of exposure.

In the working environment, several sources of metal-containing UFPs with relevant toxicological effects can be found. In this thesis UFPs emission from three kinds of industrial processes will be investigated. Results of real-time measurements of number concentration and size, morpho-chemical characterisation and quantitative analysis of metal content of airborne and deposited particles will be presented in the first section of this work (Section 1).

In the second section (Section 2), similar evaluations on the presence of airborne ultrafine particles in proximity of an industrial “hot spot” in Trieste where an integral cycle steel

plant is located will be reported. A “background” site, where UFPs emission from anthropogenic sources was expected to be minimum, will be used to make a comparison.

Afterwards nanoparticles compatible with those found in these studies will be tested *in vitro* in order to explore possible exposure routes. In particular, in the third section (Section 3) dermal and meningeal absorption will be investigated using the method of static Franz diffusion cells (Franz, 1975).

3. Sampling and characterisation techniques

3.1 Sampling devices

3.1.1 Samplers for respirable dust

According to ISO-CEN (Organization for Standardization - European Committee for standardization) definition (CEN, 1993), respirable particles are those that can penetrate the non-ciliated airways and gas-exchange region of the lungs. They are estimated as those particles passing a sampling device with a 50% collection efficiency at 4 μm (Fig.3).

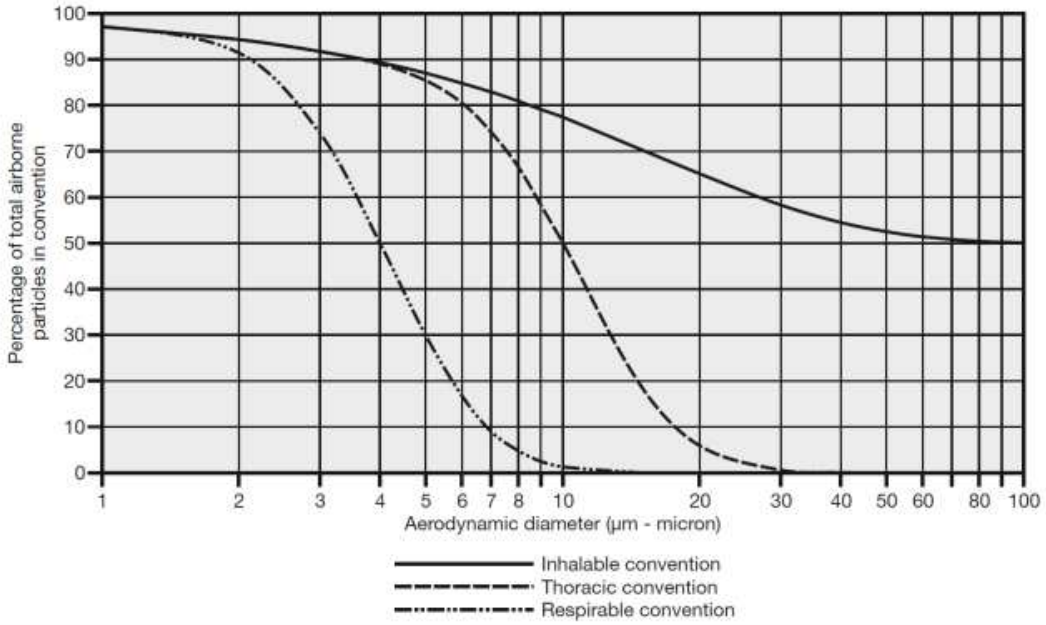

Figure 3 The inhalable, thoracic and respirable conventions as percentages of total airborne particles according to EN 481:1993.

All exposure limits in the work environments are based on personal exposure. In this work two samplers for respirable dust were used. These samplers have to be clipped in the worker's breathing zone (zone within a 0.3 m radius of a worker's nose and mouth)

and connected to an air sampler pump that provides the required flow rate. Air is drawn through a filter membrane placed inside the sampler, which traps the solid particulate e.g. dust, aerosols and fibres. Filters can be weighed and further analysed by means of different technique to have data about the amount of contaminant measured against the volume of air or the period of exposure.

The personal SKC Plastic Cyclone sampler (model no. 225-69) for respirable dust is designed to have a 50% cut-point of 4 μm at 2.2 L min^{-1}. This means that particles smaller than 4 μm are collected with an efficiency greater than 50%. The SKC GS-3 Cyclone sampler (model no. 225-103) for respirable dust is designed to have a 50% cut-point of 4 μm at 2.75 L min^{-1}.

3.1.2 Cascade impactor

The SKC Sioutas Cascade Impactor (model no. 225-370) (Misra et al., 2002) consists of four impaction stages (A, B, C, and D) and an after filter allowing the separation and collection of airborne particles in five size ranges according to aerodynamic diameter: < 0.25 μm (after filter), 0.25–0.50 μm (Stage D), 0.5–1.0 μm (Stage C), 1.0–2.5 μm (Stage B), and 2.5–10 μm (Stage A). Particles above each cut-point are collected on a 25-mm filter in the appropriate stage. Particles below the 0.25 μm cut-point of the last stage are collected on a 37-mm after filter. We used MCE filters (porosity 0.8 μm) but the choice of the membrane (PTFE, quartz, glass fibre) depends on the kind of analysis that will be performed on the samples. The impactor is used with the Leland Legacy Sample Pump (SKC) or any other pump capable of maintaining a constant flow rate of 9 L min^{-1}. The Sioutas Cascade Impactor is a personal sampling device. It clips onto a worker's collar in

the breathing zone and the pump clips onto the worker's belt. For area sampling, the impactor can be attached to a tripod or clipped in an appropriate location. The Sioutas Impactor may be also used for ambient outdoor sampling only if wind speed is < 5 mph (8 km h^{-1}). Size-fractionated samples can be analysed gravimetrically, chemically, and microscopically.

3.1.3 Portable particle counter

The Miniature Diffusion Size Classifier (DiSCmini) is a simple instrument based on unipolar charging of the aerosol, followed by detection in two electrometer stages (Fierz et al., 2011). A schematic overview of the instrument is given in Fig. 4. Aerosol is first charged in a standard positive unipolar diffusion charger, which imparts an average charge ($\bar{q}$) on the particles that is approximately proportional to the particle diameter (d). $\bar{q}$ is usually fitted with a power-law function [1] (Fierz et al., 2002; Jung et al., 2005):

$$\bar{q}(\mathrm{d}) = \mathrm{c}\mathrm{d}^{x} \quad [1]$$

where x≈1.1 for this charger; c is a constant determined in the instrument calibration. $\bar{q}$ is practically independent of particle composition, but slightly higher for agglomerated particles than for compact particles (Wang et al., 2010). After charging, excess ions are removed in an ion trap. The charged particles then flow through a so-called diffusion stage, which consists of an electrically insulated stack of stainless steel screens connected to a sensitive electrometer. Some of the particles are captured in this stage and generate a current $I_{diffusion}$, while the remaining particles flow into a second stage that is equipped with a HEPA filter. Here, all particles are captured, and a current I_{filter} is measured with an electrometer. The ratio (R) $I_{filter}/I_{diffusion}$ is a measure of the average particle size,

because smaller particles undergo larger Brownian motion, and are therefore more likely to be captured in the diffusion stage. The exact relation between R and the particle size is determined during the instrument calibration, and a corresponding calibration curve is stored on the instrument. From this calibration curve the particle size is determined, and then the particle number can be easily calculated using equation [1]: the measured total current $I_{total} = I_{filter} + I_{diffusion}$ is given by the flow rate (Φ) in the instrument, the average charge per particle and the particle number concentration (N) as:

$$I_{total} = N\bar{q}(d_p)\Phi \qquad [2]$$

By substituting equation [1] for $\bar{q}$ and solving for N, the particle number concentration is obtained. The DiSCmini is calibrated using quasi-monodisperse NaCl aerosol. Standard calibration covers the size range from 20 to 240 nm. During the calibration, the DiSCmini is operated in parallel with a condensation particle counter (CPC). The two stage currents I_{filter} and $I_{diffusion}$ are recorded along with the CPC number concentration. After the calibration process, calibration constants are obtained and then stored on the instrument to display particle diameters and concentrations online.

DiSCmini operates with a flow rate of 1 L min^{-1} and is designed to detect particles in the size range 20-700 nm (optimal measurement range 10-300 nm) and particle concentrations between 10^3– 10^6 particles cm^{-3}. The accuracy is ±30% in size and number typical; ± 500 particles cm^{-3} absolute in number.

Like most simple aerosol instruments, it is nonspecific: specific engineered nanoparticles cannot be distinguished from the ubiquitous background aerosol. While such a distinction can usually be performed only with more complex offline methods, experimental results correspond fairly well (usually within 20%) to traditional instruments: scanning mobility

particle sizer (SMPS), CPC, P-TRAK (ultrafine particle counter) (Fierz et al., 2011; Meier et al., 2013). Naturally, the DiSCmini is less accurate than these instruments but it is designed as small sized, lightweight, easy to use with a built-in rechargeable battery and can store data to a standard SD-card, so that it can be used for personal exposure monitoring.

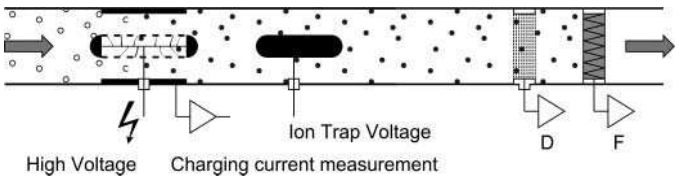

Figure 4 A schematic overview of the DiSCmini (Fierz el al., 2011).

3.2 Characterisation techniques

3.2.1 Transmission electron microscopy

Among any characterisation technique, transmission electron microscopy (TEM) is the most powerful to get information on nano-objects. It can provide detailed information such as size, shape structure and crystallinity of particles (Egerton, 2005; Goodhew et al., 2001).

TEM overcome the limitation of light microscopes for imaging very small objects, thanks to their higher resolution.

A typical transmission electron microscope consists of a vertical column in which the electron beam passes from an electron source at the top, through the specimen and down to the bottom of the column where the image is formed and revealed. The column is held

under ultra-high vacuum conditions in order to reduce the scattering of the electron beam by gas atoms. Electromagnetic coils that function as lenses are positioned around the column along its length and work in a similar way as the optical lenses do in a light microscope. Apertures of different diameters can be inserted into the electron beam at several positions along the column. This is done in order to select part of the beam excluding the contribution of the rest. There are two common types of electron sources, that are characterised by the way in which electron beam is generated (thermionic emission source or field emission gun).

After electrons are produced, they are focused and accelerated by an electrostatic field and they enter into the TEM column. The strength of this field determines the kinetic energy of the electron beam.

The condenser apertures and the lens system select the electrons and focus them in a parallel beam, setting the beam diameter to a desired value. Then the electron beam passes through the specimen, which is mounted on the specimen holder. The incident beam interacts with the internal crystal structure of the sample and emerges as a set of diffracted and non-diffracted (transmitted) beams. These beams are again focused by the objective lens on the Back Focal Plane (BFP). In this plane, diffraction pattern is formed.

There are basic TEM operations to allow both to select a specific area of the specimen to contribute to the diffraction pattern and to reduce the intensity of the diffraction pattern reaching the screen. There are two ways to perform this operation: either the beam is made smaller, or an aperture is inserted above the specimen so that only the electrons passing through it may hit the specimen. Usually the second way is applied: this operation is called Selected-Area Diffraction (SAD).

After the diffraction pattern area is selected, it is possible to perform the two most basic imaging operations in the TEM. It is possible to form the image in the TEM by using the central spot or some of the scattered electrons. If the direct beam is selected, the resultant image is called bright field (BF) image, while if scattered electrons of any form are selected, the resultant image is called dark-field (DF) image.

Inelastic interactions of the beam electrons with the specimen stimulate the emission of X-rays that are characteristic of the element constituting the sample. If an X-ray detector is present X-ray photons are collected and number of counts plotted against their energy (eV) to give a spectrum. This allows qualitative and quantitative data on the elemental composition of the area of the sample illuminated by the beam. For this reason, TEM is generally coupled with X-ray energy dispersive spectroscopy (EDS) to get morpho-chemical data.

3.2.2 Scanning electron microscopy

Scanning electron microscopy (SEM) is a type of electron microscopy that produces images of a sample by scanning it with a focused beam of electrons (Egerton, 2005; Goodhew et al., 2001). The information is derived from the interactions between accelerated electrons emitted by the SEM source and the atoms constituting the sample. The dissipation of energy of the impact produces a variety of signals. These signals are: secondary electrons (that actually produce SEM images), backscattered electrons (BSE), diffracted backscattered electrons (that are used to determine crystal structures and orientations of minerals), photons (characteristic X-rays that are used for elemental analysis), visible light (cathodoluminescence–CL), and heat. Secondary electrons show

morphology and topography on samples, while backscattered electrons are useful for illustrating contrasts in composition in multiphase samples.

In a typical SEM, an electron beam is emitted from an electron gun (a heated tungsten filament or a field emission gun). The electron beam is focused by condenser lens to a spot about 0.4-5 nm in diameter, and finally deflected by scanning coils or deflector plates, in order to raster scan the sample surface. Magnification in a SEM can be controlled over a range of about six orders of magnitude from 10 to 500,000 times. Magnification results from the ratio of the dimensions of the raster on the specimen and the raster on the display device. It is therefore controlled by the scanning coils, the deflector plates, and not by objective lens power as in optical and transmission electron microscopes.

For conventional imaging in SEM, specimens must be electrically conductive, at least at the surface, and electrically grounded to prevent the accumulation of electrostatic charge at the surface, scanning faults and image artifacts. This can be achieved by sputter coating the sample with a conductive film.

One of the advantages of the technique, with respect to TEM, is the absence of pre-treatment or a relatively simple procedure with reducing possibilities of artifacts.

The use of SEM-EDS for metal nanoparticles morpho-chemical characterisation is mostly limited by the spatial resolution: usually this technique does not allow the detection of particles with dimensions <50 nm.

4. Nanoparticles absorption through biological membranes

4.1 Theoretical aspects of diffusion

Fick's first law describes the diffusion of compounds across a membrane (Crank, 1975).

For a membrane of thickness h (cm), the flux (mass cm^{-2} h^{-1}) at steady state (Jss) is given by equation [3]:

$$Jss = \frac{DK\Delta C}{h} \qquad [3]$$

where ΔC is the concentration gradient (mass cm^{-3}) of the chemical between the two faces of the membrane, D is the diffusion coefficient (cm^2 h^{-1}) and K is the partition coefficient.

When the infinite dose conditions are applied the steady-state flux Jss can be extrapolated from an *in vitro* experiment. The flux gradually approaches a steady-state value (Jss), whilst the cumulative amount penetrating the membrane increases. Plotting the concentration of the penetrated substance as a function of time, the slope of the linear portion of the graph represents the steady-state flux Jss (Scheuplein and Blank, 1971; Crank, 1975; Dugard, 1977). The permeability coefficient Kp (cm h^{-1}) is obtained as ratio between Jss and the applied dose.

The time required for the permeation rate across a membrane to reach 95% of the steady-state value is approximately 2.3 times the lag time. The lag time (t_{lag}) is the time intercept of the linear portion of the graph in Fig.5.

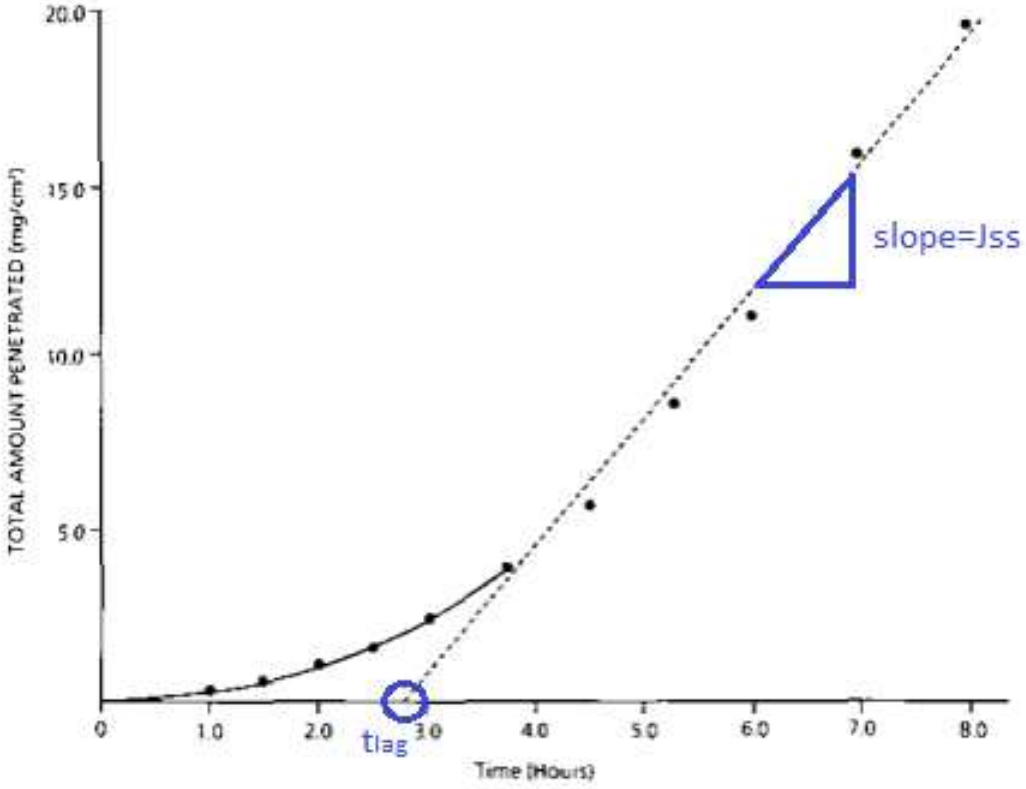

Figure 5 The steady state flux (Jss) and the permeability coefficient (Kp) can be obtained plotting the concentration of the penetrated substance per surface unit against time.

4.2 Franz Diffusion cells method

In vitro methods are commonly used to estimate the penetration and the permeation of chemicals into biological membranes. Regarding the skin, these methods can utilise non-viable skin to measure penetration and permeation but fresh skin is needed to evaluate skin metabolism. The permeability properties of the SC last after excision from the body, allowing a good agreement between *in vivo* and *in vitro* experiments. *In vitro* experiments are usually more convenient than *in vivo* ones, reducing time and costs, originating better reproducibility of results, and less restricted parameter variations, in addition to ethical reasons.

The Franz diffusion cell (Franz, 1975) is one of the most widely used systems for *in vitro* permeation studies. Franz-type diffusion cell systems are relatively simple in design. The chemical of interest dissolved (or dispersed in case of solid particles) in an aqueous solution is usually put in the donor chamber, for example synthetic sweat. The membrane that has to be studied is placed between the donor and the receptor compartment. The receptor fluid (usually saline solution) beneath the membrane is manually sampled by removing aliquots periodically for analysis (Bronaugh and Stewart, 1985). The Franz cell is kept at 32°C (to reproduce *in vivo* conditions) by heated water circulating in a glass jacket.

During the experiment, the receiving solution is continuously stirred (Fig. 6).

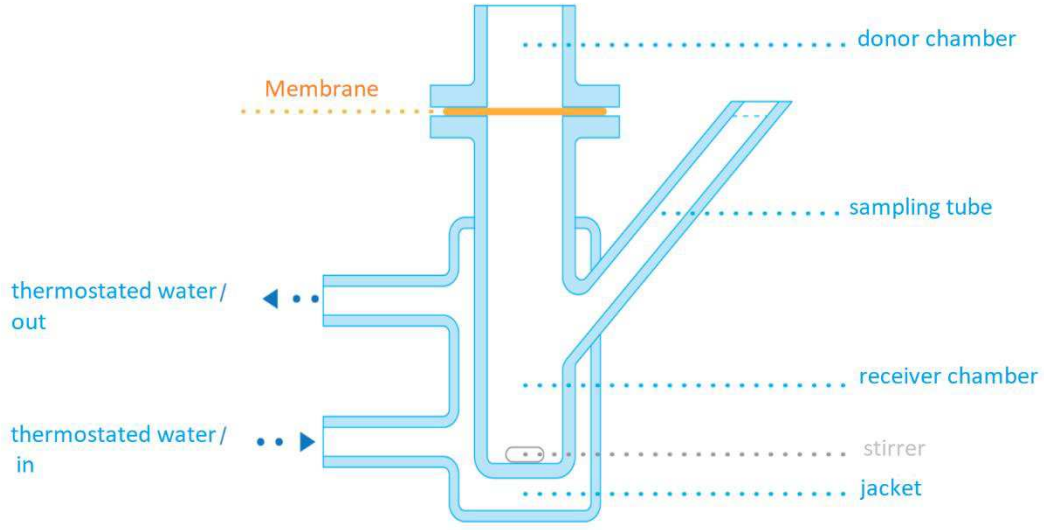

Figure 6 A schematic drawing of a Franz Diffusion Cell.

Several kinds of skin can be used in *in vitro* experiments. Human skin is the "gold standard" and has to be preferred for risk assessment purposes. Since there is reduced availability of human fresh skin, stored skin from human and laboratory animal sources

can be used. Furthermore the use of human skin is subject to national and international ethical considerations (ECETOC, 1993).

Typical human *in vitro* experiments with viable skin involve the use of female abdominal and/or breast skin obtained at autopsy or from cosmetic surgery (Dressler, 1999). Non-viable skin from several anatomical sites of male and female cadavers has also been used. Although viable skin (Bronaugh, 2004) is preferred, especially for metabolism studies, non-viable skin can also be used for certain tests. OECD Test Guideline 428 (OECD, 2004) allows a number of skin types and methods of skin preparation for the measurement of dermal absorption in vitro: (i) full-thickness skin, incorporating the stratum corneum, viable epidermis, and dermis; (ii) dermatomed skin, in which the lower dermis has been removed; (iii) epidermal membranes, comprising the viable epidermis and the stratum corneum; (iv) stratum corneum alone.

For risk assessment purposes studies, full-thickness skin is preferred. It has been recommended that before, and in some cases after the experiment, the barrier integrity of the skin should be checked by physical methods, such as transepidermal water loss or transcutaneous electrical resistance (Davies et al., 2004; OECD, 2004). In literature, there are several studies in which cryopreserved human skin is used. The recommendation of testing skin integrity is even more important when stored skin is evaluated.

In daily life not only intact skin could be exposed to chemicals. For this reason, in literature many in vitro experiments evaluating damaged skin permeation are found (Larese et al, 2009; Baroli, 2010). Usually, in *in vitro* conditions, only the outer layers of stratum corneum are damaged, following a certified protocol, in order to avoid overestimations.

References

Baroli, B., 2010. Penetration of Nanoparticles and Nanomaterials in the Skin: Fiction or Reality? *J. Pharm. Sci*. 99: 21-50.

Bronaugh, R. L. (2004). *Methods for in vitro percutaneous absorption*. In: Zhai, H. & Maibach, H. I. eds. Dermatotoxicology, 6th ed. New York, CRC Press. pp. 520–526.

Bronaugh, R. L. and Stewart, R. F. (1985). Methods for in vitro percutaneous absorption studies V: permeation through damaged skin. *J. Pharm. Sci*. 74(10): 1062–1066.

CEN. European Committee for Standardization. (1993). *Workplace atmospheres: size fraction definitions for measurement of airborne particles* (Report No. BS EN 481:1993). London, England: CEN, British Standards Institute.

Crank, J. (1975). *Mathematics of diffusion*. Oxford University Press. Oxford. pp. 50–51.

Crosera, M., Bovenzi, M., Maina, G., Adami, G., et al. (2009). Nanoparticle dermal absorption and toxicity; a review of the literature. *Int. Arch. Occup. Environ. Health*. 82: 1043-1055.

Davies, D. J., Ward, R. J. and Heylings, J. R. (2004). Multi-species assessment of electrical resistance as a skin integrity marker for in vitro percutaneous absorption studies. *Toxicol. In Vitro*. 18(3): 351–358.

Dressler, W. E. (1999). *Hair dye absorption*. In: Bronaugh, R. L. & Maibach, H. I. eds. Percutaneous absorption: drugs–cosmetics–mechanisms–methodology, 3rd ed. New York, Marcel Dekker. pp. 685–716 (Drugs and the Pharmaceutical Sciences Vol. 97).

Dugard, P. H. (1977). *Skin permeability theory in relation to measurements of percutaneous absorption in toxicology*. In: Marzulli, F. N. & Maibach, H. I. eds. Dermatotoxicology and pharmacology. Washington, DC, Hemisphere Publishing Corp. pp. 525–550 (Advances in Modern Toxicology Vol. 4).

ECETOC (1993). *Percutaneous absorption*. Brussels, European Centre for Ecotoxicology and Toxicology of Chemicals. pp. 1–80 (Monograph No. 20).

Egerton, R.F. (2005). *Physical Principles of Electron Microscopy – An Introduction to TEM, SEM and AEM*. Springer Science.

EHC 235 (2006). Environmental Health Criteria 235. *Dermal Absorption*. World Health Organization.

Fierz, M., Houle, C., Steigmeier, P. and Burtscher, H. (2011). Desing, Calibration, and Field Performance of a Miniature Diffusion Size Classifier. *Aerosol Sci. Technol*. 45: 1-10.

Fierz, M., Scherrer, L. and Burtscher, H. (2002). Real-Time Measurement of Aerosol Size Distributions with an Electrical Diffusion Battery. *J. Aerosol Sci*. (33): 1049-1060.

Franz, T. J. (1975). On the relevance of in vitro data. *J. Invest. Dermatol*. 93: 633-640.

Goodhew, P. J., Humphreys, J. and Beanland, R. (2001). *Electron Microscopy and Analysis*, 3rd edition, Taylor & Francis.

Gwinn, M. R. and Vallyathan, V. (2006). Nanoparticles: health effects-pros and cons. *Environ. Health. Perspect.* 114: 1818–1825.

Jung, H. and Kittelson, D. B. (2005). Characterization of Aerosol Surface Instruments in Transition Regime. *Aerosol Sci. Technol*. 39: 902–911.

Kumar, P., Robins, A., Vardoulakis, S. and Britter, R. (2010). A review of the characteristics of nanoparticles in the urban atmosphere and the prospects for developing regulatory controls. *Atmos. Environ*. 44: 5035–5052.

Labouta, H. I. and Schneider, M. (2013). Interaction of inorganic nanoparticles with the skin barrier: current status and critical review. *Nanomedicine*. 9: 39-54.

Larese Filon, F., Mauro, M., Adami, G., Bovenzi, M. and Crosera, M. (2015) Nanoparticles skin absorption: New aspects for a safety profile evaluation. *Regul. Toxicol. Pharmacol*. 72(2): 310-322.

Larese, F.F., D'Agostin, F., Crosera, M., Adami, et al. (2009). Human skin penetration of silver nanoparticles through intact and damaged skin. *Toxicology*. 255: 33–37.

Li, N., Sioutas, C., Cho, A., Schmitz, D., et al. (2003). Ultrafine particulate pollutants induce oxidative stress and mitochondrial damage. *Environ. Health. Perspect*. 111:455–460.

Maynard, A. D. and Aitken, R. J. (2007). Assessing exposure to airborne nanomaterials: current abilities and future requirements. *Nanotoxicology* 1: 26-41.

Meier, R., Clark, K. and Riediker, M. (2013). Comparative Testing of a Miniature Diffusion Size Classifier to Assess Airborne Ultrafine Particles Under Field Conditions. *Aerosol Sci. Technol*. 47: 22–28.

Misra, C., Singh, M., Shen, S. Sioutas, C., et al. (2002). Development and evaluation of a personal cascade impactor sampler (PCIS). J. Aerosol Sci. 33(7): 1027-1047.

Murr, L. E. and Garza, K. M. (2009). Natural and anthropogenic environmental nanoparticulates: their microstructural characterization and respiratory health implications. *Atmos. Environ*. 43: 2683-2692.

Oberdörster, G., Oberdörster, E. and Oberdörster, J. (2005). Nanotoxicology: an emerging discipline evolving from studies of ultrafine particles. *Environ. Health Perspect*. 113(7): 823-839.

OECD. (2004). Organization for Economic Co-operation and Development. *Skin Absorption: in vitro Method*. Test Guideline, 428.

Rawlings, A. V., Scott, I. R., Harding, C. R. and Bowser, P. A. (1994). Stratum corneum moisturization at the molecular level. *J. Invest. Dermatol*. 103: 731-740.

Scheuplein, R. J. and Blank, I. H. (1971). Permeability of the skin. *Physiol. Rev*. 51(4): 702–747.

Wang, J., Shin, W. G., Mertler, M., Sachweh, B., et al. (2010). Measurement of Nanoparticle Agglomerates by Combined Measurement of Electrical Mobility and Unipolar Charging Properties. *Aerosol Sci. Technol*. 44: 97–108.

SECTION 1

Occupational exposure to ultrafine and submicron particles

The study of UFPs emission during various operations in industrial settings is important to enhance knowledge on occupational diseases that may be related to it.
In the working environment several sources of metal-containing UFPs with relevant toxicological effects can be found.

There are important gaps in the study of occupational exposure to NPs/UFPs in workplace scenarios and at the moment no standardised risk assessment protocol exists (Prodi and Larese, 2016).

In recent years it has been under discussion which metrics would be most relevant to monitor in relation to the exposure to UFPs in workplaces (Brouwer et al., 2004). Mass concentration does not seem to be a sufficient parameter to evaluate health hazard. Number concentration, size distribution, chemical composition and morphological characteristics of UFPs should be considered in the risk assessment.

In this section two studies about the characterisation of ultrafine and submicron particles in working environments are presented.

A critical point in the evaluation of personal exposure in occupational contexts is the necessity of using samplers that are compact and light weight to interfere minimally with normal activities of workers (Lee et al., 2006). For this reason in the two studies of this section all sampling devices used were portable.

The first study focuses on the morpho-chemical characterisation of Gas Tungsten Arc Welding (GTAW) fumes particles by means of TEM-EDS. The aim of the study was to evaluate the differences in terms of size, morphology and chemical characteristics between particles produced by an automatic and a manual GTAW process performed in an automotive plant.

The results of this work have been accepted for publication by the journal *Aerosol and Air Quality Research*.

After this first study a more comprehensive approach was used to assess the exposure of workers to ultrafine and submicron particles in three industrial settings where aluminium was used as raw material in different manufacturing processes. An integrated approach including air monitoring and the evaluation of skin and surface contamination was used in real workplace environments to better understand potential exposure and possible health effects on workers.

1. Ultrafine and submicron particles emission during Gas Tungsten Arc Welding of steel

1.1 Introduction

In the working environment several sources of metal ultrafine particles with relevant toxicological effects can be found. Among these sources the welding fumes are probably the most interesting ones from both a chemical and toxicological point of view (Berlinger et al., 2008). The high temperatures used in welding operations originate fine and ultrafine particles represented by metal oxides, unoxidized metals and compounds, such as fluorides and chlorides (Konarski et al., 2003a). The occupational exposure of welders to (ultrafine) particles with high number concentrations, heterogeneous chemical composition and different reactivity properties may be high, since workers are often very close to the source (Buonanno et al., 2011). Data in literature show that metal oxide NPs identified in lung tissue samples from welders are involved in the development of pulmonary inflammation (Andujar et al., 2014). As reported by McNeilly and co-workers (2004), exposure to welding aerosols produces marked pro-inflammatory effects that are thought to be driven largely by transition metals undergoing redox cycling, resulting in oxidative stress.

Gas Tungsten Arc Welding (GTAW) is the most important technique in terms of occupational exposure because it causes the formation of smaller ultrafine particles compared with other welding techniques (Lehnert et al., 2012; Brand et al., 2013; Miettinen et al., 2016). In addition, GTAW welding has become one of the most popular welding methods in various industrial settings like the automotive one (Buonanno et al.,

2011) because, as reported by Kou (2003), this technique grants the operator greater control over the weld than other welding processes, allowing very clean, strong and higher quality welds.

According to the mechanism of their formation, welding fumes particles can be divided into three categories: (i) ultrafine particles (diameter < 0.1 μm), also called primary particles, formed by condensation from the gas phase; (ii) particles (diameter between 0.1 and 1 μm) which are mainly agglomerates, that are those particles made up of primary particles that adhere together because of electrostatic or van der Waals forces, and aggregates that are clumps of primary particles that have fused together; and (iii) coarse fume particles (diameter > 1 μm) formed by mechanical forces (Jenkins et al., 2005a).

A number of health problems are due to occupational exposure to welding fumes such as metal fume fever, chronic bronchitis, asthma, lung cancer and manganism (Antonini, 2003). Ultrafine particles in welding fumes are considered a risk factor because they are characterised by a large surface-to-volume ratio. In contrast to larger-sized particles, ultrafine particles, when inhaled, are efficiently deposited in all regions of the respiratory tract and, evading specific defense mechanisms, they can translocate out of the respiratory tract and reach blood circulation and other internal organ or central nervous system via nose route causing an increase in cardiovascular diseases and neurological effects (Oberdörster et al., 2005).

Characterising dimensions, shape and composition of welding fumes particles is important to better understand their toxicity and helps to clarify the possible effects of engineered nanoparticles. The comparison with known exposures, such as to welding fumes, permits to bridge effects from traditional to new “nano” exposure.

A transmission electron microscope coupled with an energy-dispersive X-ray analytical system (TEM-EDS) is an effective tool for the analysis of aerosol particles. It can provide a detailed morpho-chemical characterisation (size distributions, shapes, microchemical data and structural information) of welding fumes particles.

Even if various methods have been proposed for direct and indirect particle collection on TEM grids, such as thermophoretic precipitation (Bang et al., 2003), electrostatic precipitation (Miller et al., 2010), and deposition onto a TEM grid of a dissolved part of the filter used to collect the particles (Moroni and Viti, 2009), the most used direct method for sampling welding fumes particles on TEM grids involves impactors (cascade and electrical low pressure impactors).

At the moment few studies have investigated the fumes at the nanometric scale and most of them are focused on gas metal arc welding (GMAW), shielded metal arc welding (SMAW), and flux-cored arc welding (FCAW) fumes, while few studies focus on the gas tungsten arc welding (GTAW) fumes (Jenkins et al., 2005a; Jenkins et al., 2005b; Konarski et al., 2003a; Konarski et al., 2003b; Lehnert et al., 2012; Moroni and Viti, 2009; Sowards et al., 2010; Sowards et al., 2008a; Sowards et al., 2008b; Zimmer and Biswas, 2001).

The particle size distribution, morphology and chemical composition of the welding fumes particles seem to be related to the welding process typology and the welding alloy (Zimmer and Biswas, 2001). An interesting study of Lehnert et al. (2012) found that GTAW generated smaller particles than GMAW, FCAW, and SMAW which generated mainly agglomerates with higher dimensions. The highest mass concentrations were found in FCAW, followed by GMAW and SMAW, whereas mass concentrations for GTAW were frequently not determinable because too low to be detected by weighing

filter samples. Although GTAW appeared with the lowest concentrations in terms of particle mass, larger numbers of small-sized particles, including ultrafine particles, were observed. Brand et al. (2013) reported that GTAW generates a majority of particles at the nanoscale.

Since few studies focus on GTAW fumes particles, even though they are potentially the most hazardous ones in terms of occupational exposure, in this study two different real sources of GTAW fumes particles, collected in an automotive plant, were characterised by means of TEM-EDS and compared to a zone of the plant far from the two sources used as a reference background.

1.2 Materials and methods

1.2.1 Chemicals

All chemicals were ultrapure grade. Nitric acid (≥ 69%), hydrochloric acid (≥ 37%) and hydrofluoric acid (48%) were purchased from Sigma Aldrich (Milan, Italy). Water reagent grade was produced with a Millipore purification pack system (MilliQ® water).

1.2.2 Fume collection procedure

The welding fumes produced during the GTAW process were sampled in a factory operating in the automotive sector. Three indoor sampling zones were set (see Fig. 1.1.1): (i) in proximity of the automatic welder arm (A-GTAW); (ii) next to the operator performing manual welding (M-GTAW); (iii) in a zone of the factory approximately 500 m far from the exposure source, near the offices, used as a reference background (BKD). In each sampling zone, at a distance of 0.5 m to the welding arc for A-GTAW and M-GTAW zones, three air sampler pumps (GilAir Plus, Sensidyne) were set to a flow of 2.2

L min^{-1} and connected each one to a personal SKC Plastic Cyclone sampler (model no. 225-69) for respirable dust (50% cut point for 4 µm aerodynamic diameter if set to a flow rate of 2.2 L min^{-1}) containing two TEM supports (200 mesh copper grids coated with a 20 nm carbon support film, Media System Lab, Italy) to collect particles. TEM grids were placed between the filter support grid and a Mixed Cellulose Ester (MCE) filter membrane (Whatman GmbH, Germany) with 5 µm pore size for two main reasons: the first is to reduce the mobility of TEM grids due to the air flow, the second is to prevent the deposition of particles with size larger than 5 µm that could be collected by the cyclone, even if with an efficiency less than 50%, saturating the TEM grids. Therefore, in each sampling zone, six TEM grids were located. The sampling procedure lasted 20 minutes in each sampling zone.

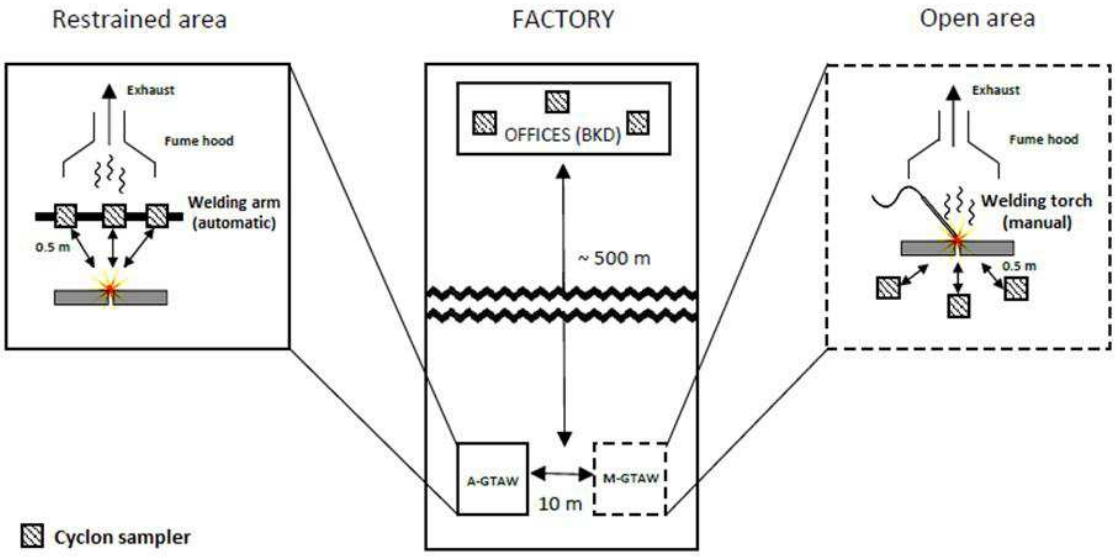

Figure 1.1.1 Schematic representation of the sampling points in the three zones.

1.2.3 Chemical analysis of welding wires

The chemical composition of mild steel welding wires used during the automatic and manual operations was specified by the producer in the datasheet (see Table 1.1.1).

Inductively coupled plasma atomic emission spectroscopy (ICP-AES) was used to verify the chemical composition of wires. The instrument used for analysis was a PerkinElmer Optima 8000 equipped with autosampler S10.

Three independent pieces of each type of welding wire were taken from the batch used during the sampling of fumes.

A mixture of acids 1:3 (v/v) HNO_3: HCl and HF was added to about 40 mg (5 mm) of each welding wire sample, heated till complete dissolution, then diluted to 25 mL with MilliQ water. The obtained solutions were analysed for total iron, manganese, silicon, chromium and copper concentration. Analyses were conducted using a calibration curve, obtained by dilution (range: 0–10 mg L^{-1}) of iron, manganese, silicon, chromium and copper standard solutions for ICP-AES analyses. The limit of detection (LOD) at the operative wavelength for each element was: 0.020 mg L^{-1} for Fe at 238.204 nm, 0.020 mg L^{-1} for Mn at 257.610 nm, 0.050 mg L^{-1} for Si at 251.611 nm, 0.050 mg L^{-1} for Cr at 267.716, 0.020 mg L^{-1} for Cu at 327.393 nm. The precision of the measurements as repeatability (RSD %) for the analysis was always less than 5%.

1.2.4 TEM-EDS investigations

The morphological characteristics, dimensions, crystallinity and chemical composition of the particles were acquired by using a transmission electron microscope (TEM Philips CM12) working at 120 kV, equipped with LaB_6 cathode, double tilt holder, and a 622 SC CDD YAG Gatan Camera, coupled with an energy dispersive X-ray analyser (EDS,

EDAX Genesis 2000, Si(Li) detector, TEM QUANT software). The chemical data were processed with the TEM QUANT software system using default K factors.

Two TEM grids for each of the three personal cyclone samplers placed in each of the three sampling zones, for a total amount of eighteen, were investigated by means of TEM. During TEM grids observation, dimensions of individual particles and aggregation states (agglomerates and aggregates) were collected, for a total amount of more than 750 data. As regards the identification of the aggregation state, in the agglomerates the boundaries between primary particles that form the agglomerate are clearly distinguishable in TEM images while aggregates are clumps of primary particles that have fused together and for this reason their outlines are not clearly defined. TEM images were developed only for the most significant observations and, in that case, the dimensions of particles, agglomerates and aggregates were measured by means of a Vernier scale (without an image processing tool). At the same time, over 500 EDS chemical analyses were performed. Compositional data and morphological shapes were used to identify the compound type. Besides, the obtained EDS spectra were compared with an EDS/SEM database previously made by using samples characterised in detail by other techniques (Fornero et al., 2009).

Data analysis was performed using Excel (Microsoft Office Professional Plus 2010).

In this study the particles observed were grouped according to the chemical composition and aggregation state.

1.3 Results

1.3.1 Results of chemical analysis of welding wires

The results of ICP-AES analysis confirmed the chemical composition of welding wires written in the datasheet as reported in Table 1.1.1.

Table 1.1.1 Chemical composition of welding wires used during the automatic and manual operations as specified in the datasheet and verified by means of ICP-AES analysis. Note: n.d.= not determined.

Wire	% Fe	% Mn	% Si	% Cr	% Cu
Datasheet					
A-GTAW	>90	1-2	<1	<0.5	<0.5
M-GTAW	>90	1-2	<1	n.d.	n.d.
ICP-AES analysis					
A-GTAW	97.87	1.45	0.44	0.05	0.10
M-GTAW	96.85	1.70	0.66	0.03	0.02

1.3.2 Results of TEM-EDS investigations

During TEM-EDS investigations, the chemical composition of the grid must be taken into account. The characteristic peaks due to the material of the grid (C, Cu, Ni and Zn) will be present in each acquired spectra. Sometimes, when the chemical analysis was performed close to border of the grid, a Pt peak due to X-ray emissions from microscope diaphragm appeared. A typical energy dispersive X-ray spectrum of the background of the grid in the case study is reported in Fig. 1.1.2.

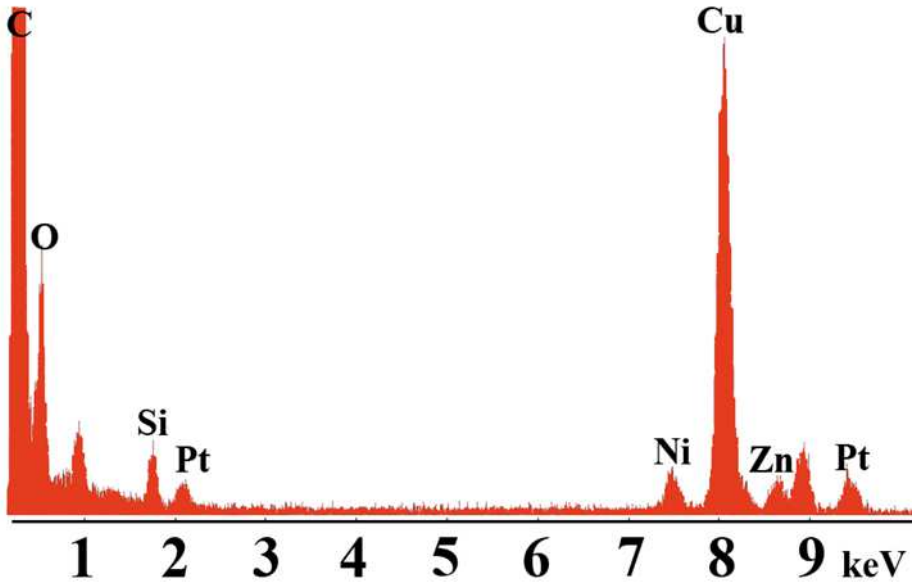

Figure 1.1.2 Typical EDS spectrum of the background of TEM grids in the case study.

A part from the peaks related to the elements that compose the material of the grids, a typical spectrum of the background of the grid showed the peaks related to O and Si. It revealed the presence of silica that was ubiquitous in all the grids collected after the fumes sampling procedure, whereas the signals of O and Si were absent in a typical spectrum of a TEM grid not exposed to the fumes.

The particles observed were grouped according to their chemical composition (Table 1.1.2) because of its significance from an occupational exposure point of view: metal oxides like iron, manganese, cobalt, titanium, aluminum and chromium oxides, and silicates. Silica particles have been demonstrated to persist in the lungs, and this greater pulmonary persistence may contribute to the chronic lung disease (silicosis) that it causes (Brody et al., 1982). From literature it is also known that welding related ultrafine particles (as iron, chromium, and manganese oxides) could be responsible, at least in part, for the pulmonary inflammation observed in welders (Andujar et al., 2014).

Table 1.1.2 Characterisation of the particles found on A-GTAW, M-GTAW and BKD samples. Note: Chemical composition, aggregation state and dimensions revealed by TEM–EDS investigations for automatic and manual gas tungsten arc welding (A-GTAW, M-GTAW).

Chemical elements	Aggregation state	Minimum diameter* (µm)	Maximum diameter* (µm)	Average diameter* (µm) (SD)	Number of particles observed
A-GTAW					
O, Fe, Mn	Agglomerates of particles chainlike	0.014	0.208	0.047 (0.034)	305
O, Fe	Agglomerates of particles chainlike	0.008	0.043	0.021 (0.016)	242
O, Cr	Particles	1.250	1.292	1.276 (0.013)	13
O, Si, (Al, Mg, Fe, K, Na, Ca)	Particles, agglomerates, aggregates	0.230	1.523	0.791 (0.543)	38
M-GTAW					
O, Al, Ti	Super-aggregate	0.317	0.405	0.349 (0.035)	12
O, Fe, Co	Particles in the super-aggregates	0.008	0.061	0.022 (0.015)	51
O, Cr	Aggregates	0.531	2.621	1.434 (0.716)	17
O, Si, (Al, Mg, Fe, K, Na, Ca)	Aggregates	0.328	1.752	0.924 (0.527)	32
BKD					
O, Si, (Al, Mg, Fe)	Particles, agglomerates, aggregates	0.036	2.016	0.537 (0.626)	43

On the grids collected in the zone in which automatic welding was performed (A-GTAW), particles, agglomerates and aggregates of a wide dimensional range were

observed. The most representative particles were constituted by iron/manganese oxide. Nanoparticles with this chemical composition formed agglomerates chainlike as shown in Figs. 1.1.3 and 1.1.4. The equivalent diameter (Feret diameter) (Merkus, 2009) of about 300 particles was measured and the average diameter was 47 nm. The second most represented group in grids was agglomerates of iron oxide nanoparticles chainlike (Fig. 1.1.5) with a mean diameter of 21 nm. Very few are chromium oxide single particles with an average diameter of 1.276 μm. Agglomerates and aggregates of different kinds of silicates were found with average diameter of 0.791 μm.

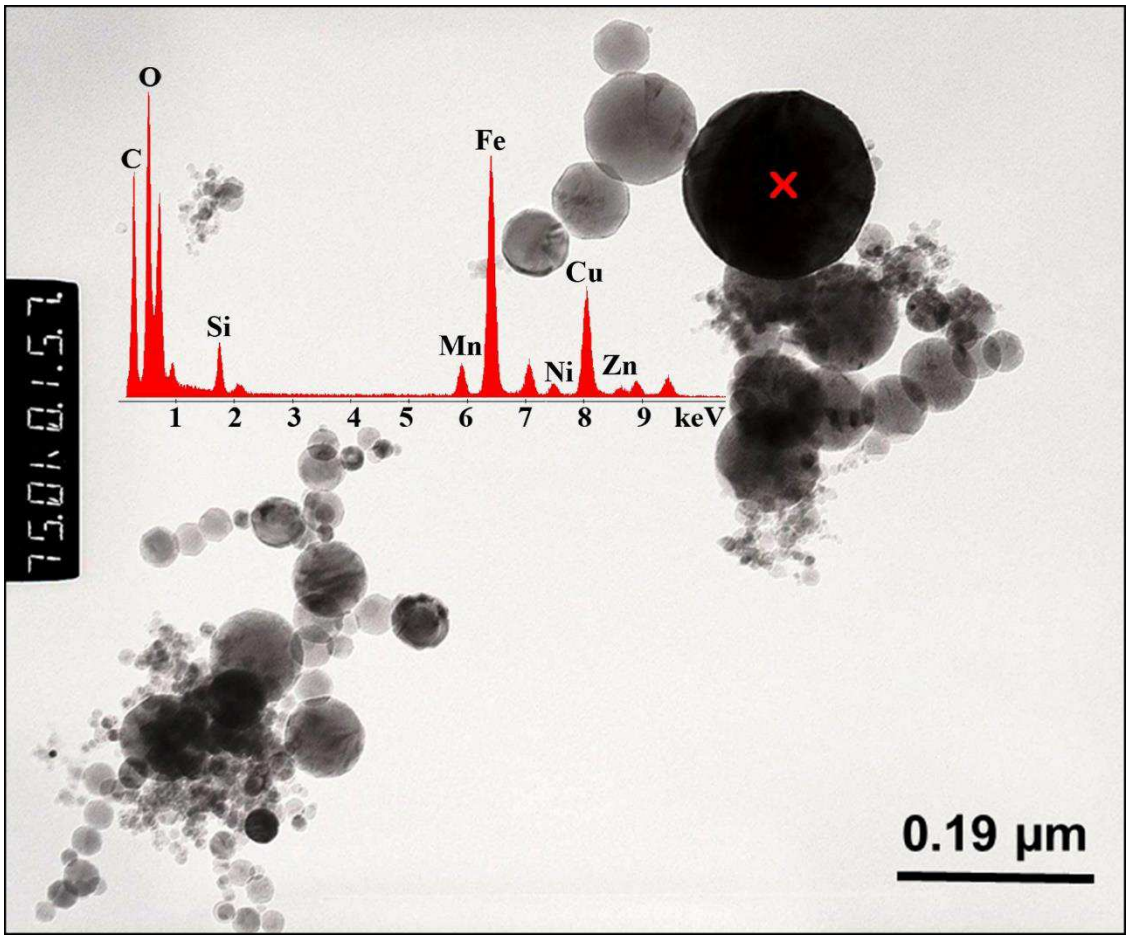

Figure 1.1.3 Representative TEM image and EDS spectrum of an agglomerate found on a A-GTAW sample. Note: Scale bar: 0.19 μm. The colored X in figure represents the center of the microanalysis spot. Spectrum refers to iron/manganese oxide.

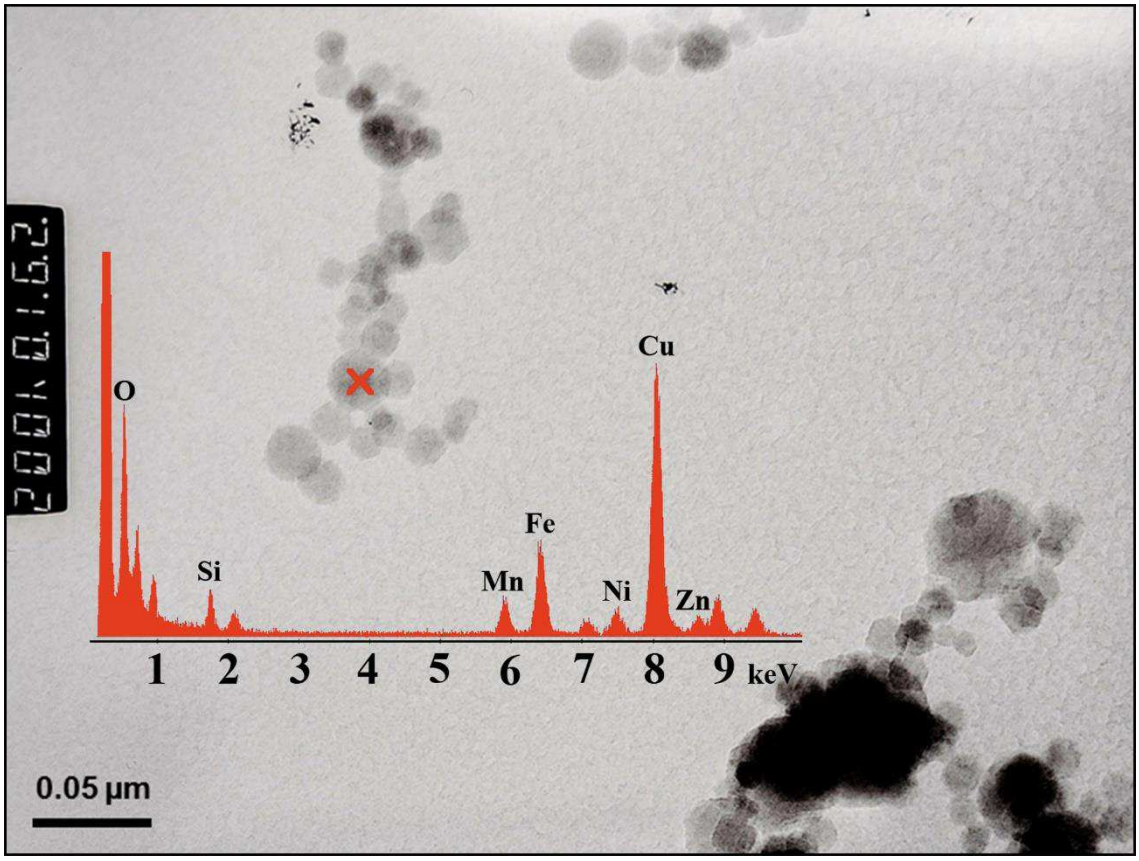

Figure 1.1.4 Representative TEM image and EDS spectrum of an agglomerate found on a A-GTAW sample. Note: Scale bar: 50 nm. The colored X in figure represents the center of the microanalysis spot. Spectrum refers to iron/manganese oxide.

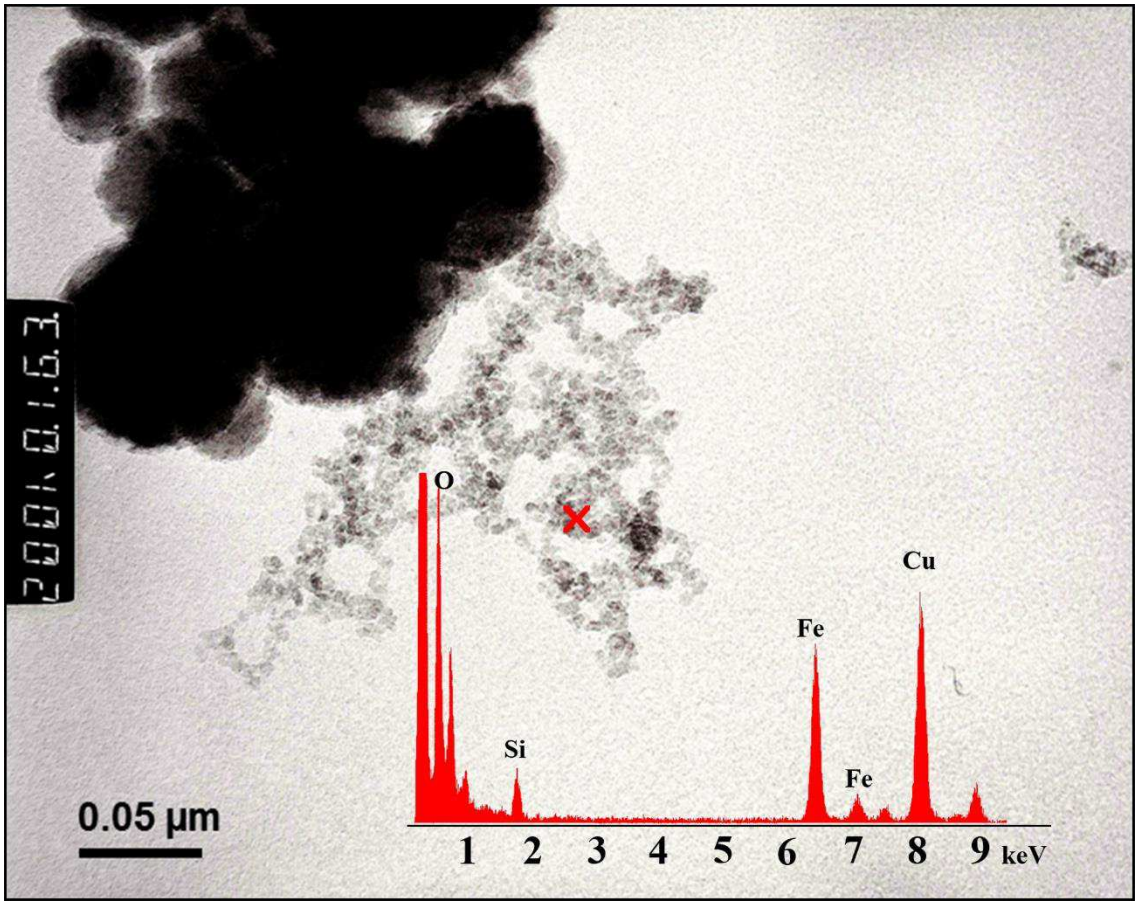

Figure 1.1.5 Representative TEM image and EDS spectrum of an agglomerate found on a A-GTAW sample. Note: Scale bar: 50 nm. The colored X in figure represents the center of the microanalysis spot. Spectrum refers to iron oxide.

On the grids collected in the zone in which manual welding was performed (M-GTAW), three kinds of aggregates were observed. Fig. 1.1.6 shows an example of the first kind of super-aggregates, mainly composed of aluminum and titanium oxides (X-ray spectrum in blue), with an average diameter of 0.349 µm. Inside these super-aggregates some iron and cobalt oxides nanoparticles (X-ray spectrum in red) with an average diameter of 22 nm were observed. The second kind of aggregates (Figs. 1.1.7 and 1.1.8) was composed of chromium oxides and had an average diameter of 1.434 µm. The third kind of aggregates

had an average diameter of 0.924 μm and showed an X-ray spectrum characteristic of different kinds of silicates.

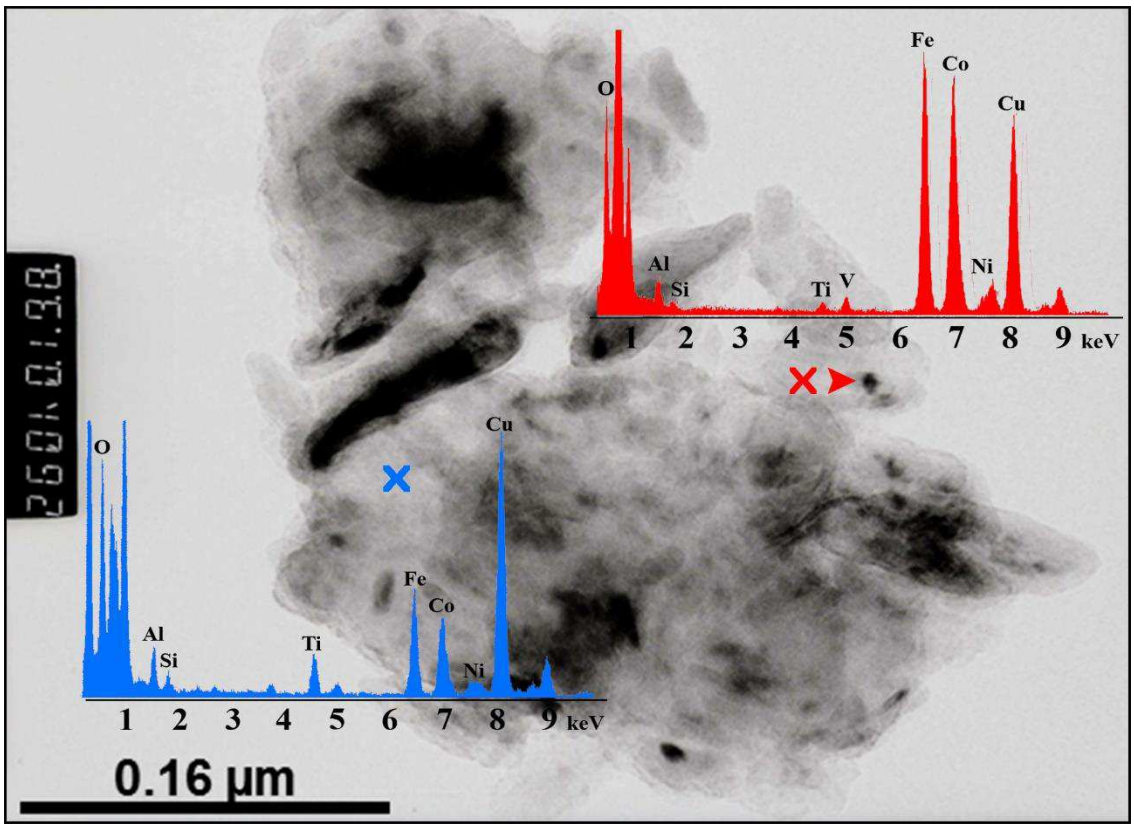

Figure 1.1.6 Representative TEM image and EDS spectra of a super-aggregate found on a M-GTAW sample. Note: Scale bar: 0.16 μm. The colored X in figure represent the centers of the microanalysis spot. Red spectrum refers to iron and cobalt oxides, the blue one refers to aluminum and titanium oxides.

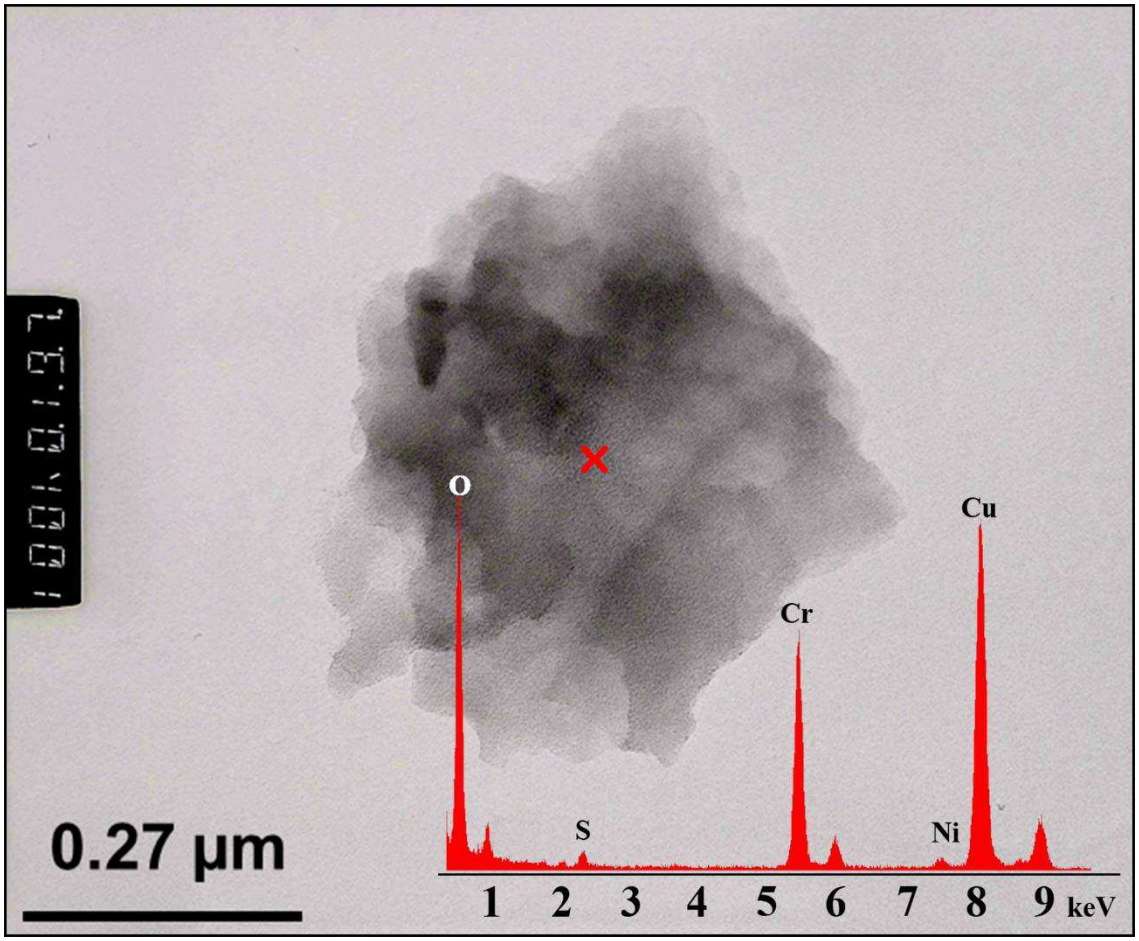

Figure 1.1.7 Representative TEM image and EDS spectrum of an aggregate found on a M-GTAW sample. Note: Scale bar: 0.27 µm. The colored X in figure represents the center of the microanalysis spot. Spectrum refers to chromium oxide.

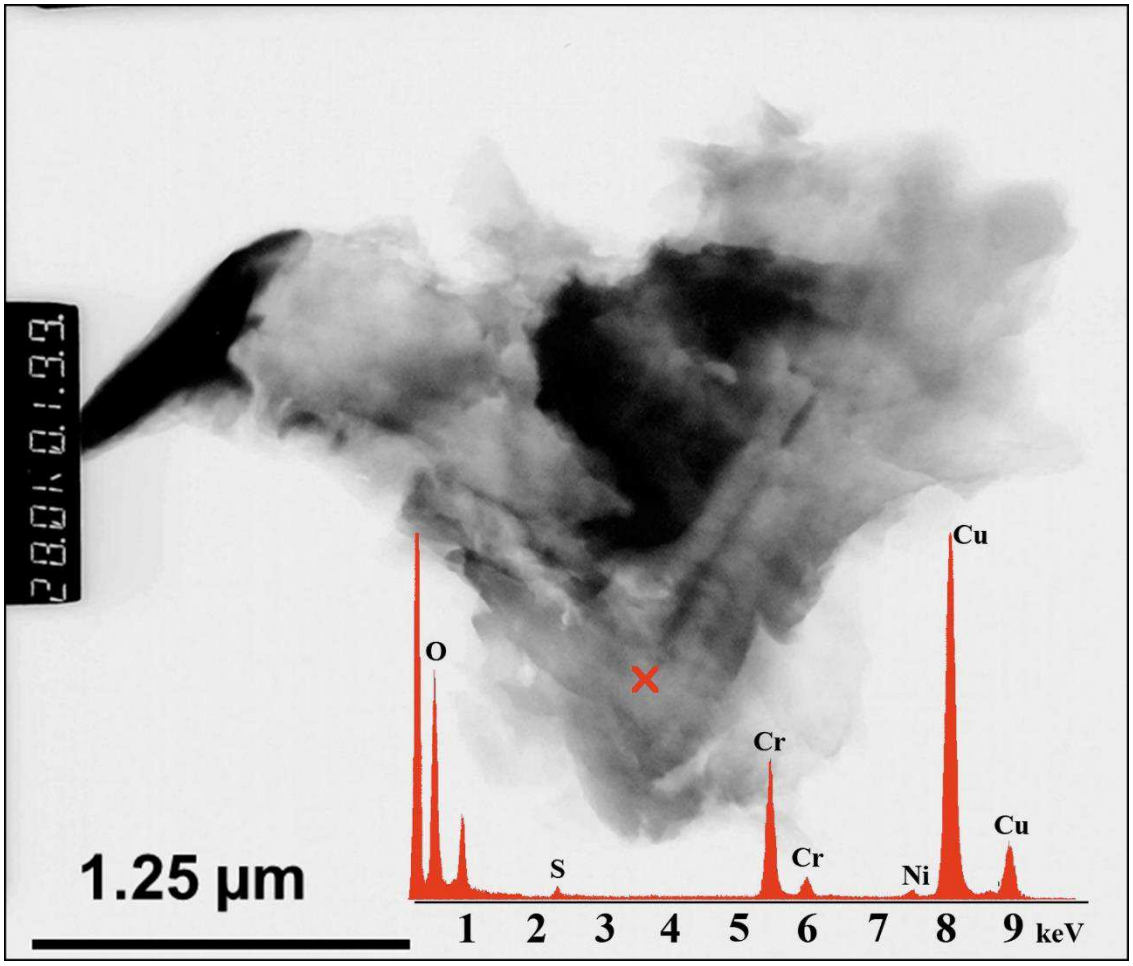

Figure 1.1.8 Representative TEM image and EDS spectrum of an aggregate found on a M-GTAW sample. Note: Scale bar: 1.25 µm. The colored X in figure represents the center of the microanalysis spot. Spectrum refers to chromium oxide.

On the grids collected in the zone far from the welding fumes source (BKD), particles, agglomerates and aggregates were found. Figs. 1.1.9 and 1.1.10 show two examples of aggregates that were probably aluminosilicates (Fig. 1.1.9) and phyllosilicates (Fig. 1.1.10), amorphous and in some cases crystalline. The average diameter of these particles was 0.537 µm.

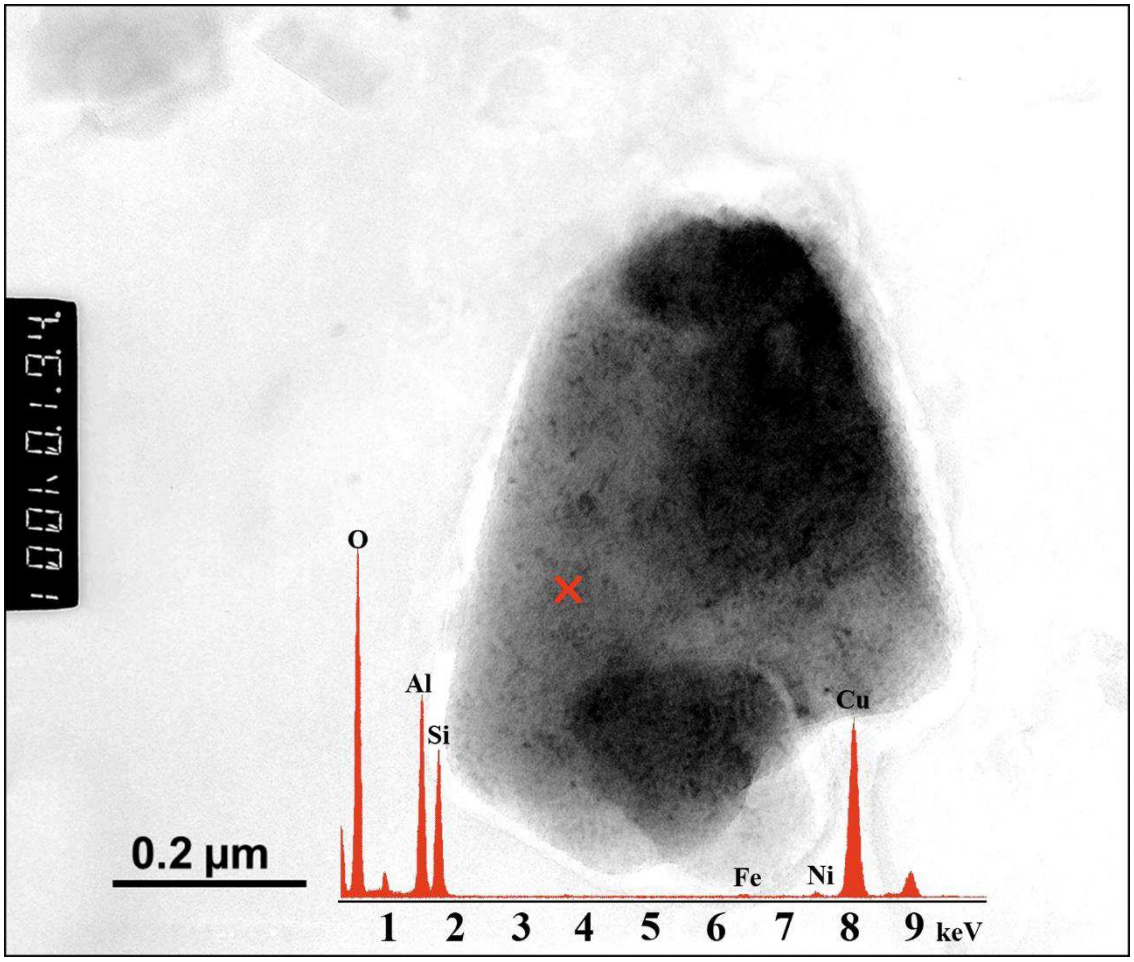

Figure 1.1.9 Representative TEM image and EDS spectrum of an aggregate found on a BKD sample. Note: Scale bar: 0.20 µm. The colored X in figure represents the center of the microanalysis spot. Spectrum refers to an alluminosilicate.

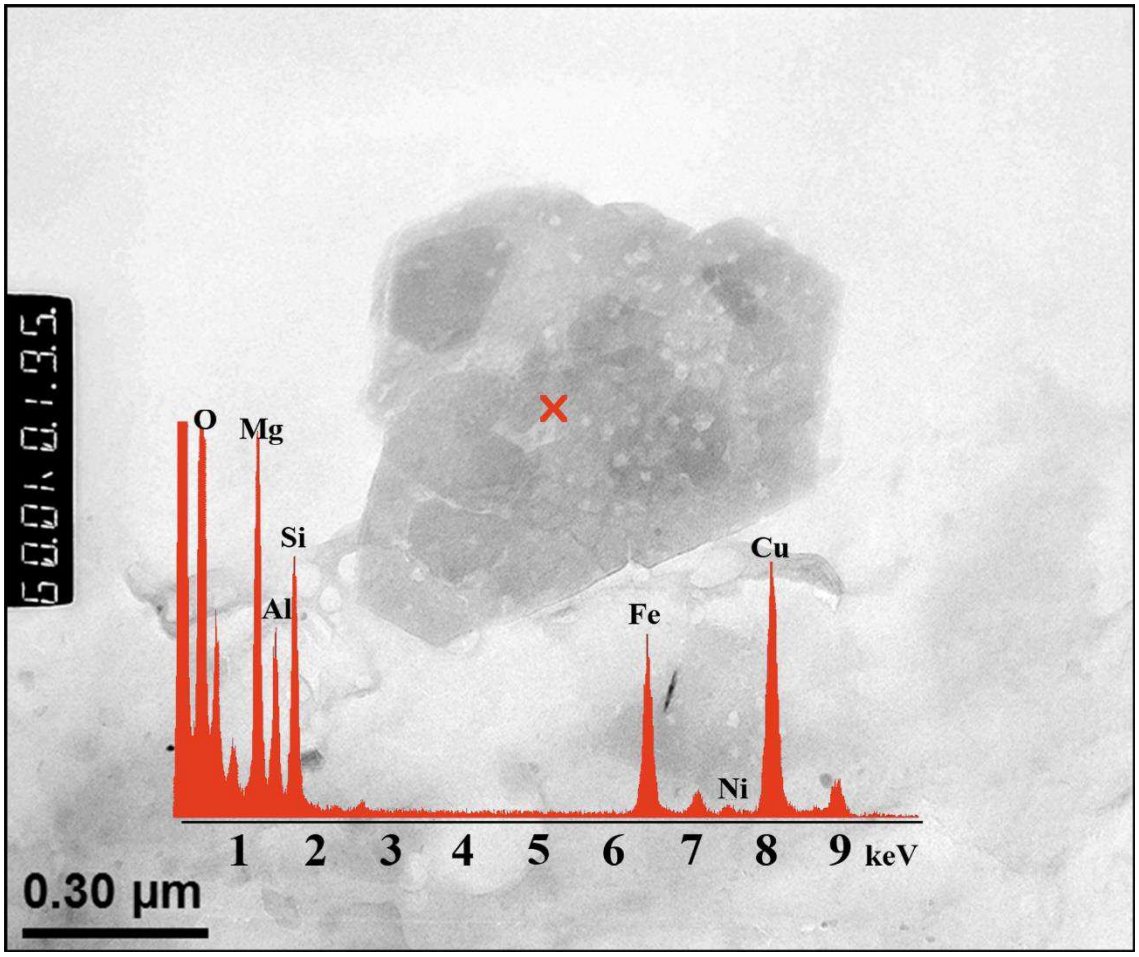

Figure 1.1.10 Representative TEM image and EDS spectrum of an aggregate found on a BKD sample. Note: Scale bar: 0.30 µm. The colored X in figure represents the center of the microanalysis spot. Spectrum refers to a phyllosilicate.

1.4 Discussion

During the GTAW process the aerosol generated is mainly nanosized: Miettinen et al. (2016) reported a geometric mean diameter of 46 nm in the middle of the workshop and lower size near the breathing zone. Similar results were found by Berlinger et al. (2011), Lehnert et al. (2012) and Brand et al. (2013). In our study we went deeply on shape and chemical composition of ultrafine and submicron particles emitted during both automatic

and manual GTAW of steel to clarify their characteristics, finding new data that can help understanding the link between exposure and toxicity for exposed workers.

Analysing automatic GTAW, TEM observations of size and shape of the collected particles are substantially in agreement with previous studies (Berlinger et al., 2011; Graczyk et al., 2016). No individual primary particles in the nanoscale were found. Particles in the ultrafine range were predominantly spherical, in some cases polyhedral, with clearly distinguishable boundaries and formed chainlike agglomerates with fractal geometry. The majority of emitted particles in respirable range was chainlike agglomerates constituted by iron/manganese oxide nanoparticles with size ranging from 14 to 208 nm and a mean value of 47 nm. Despite the low percentage of manganese in wires (<2%), the smallest then more dangerous particles emitted during the welding process contained manganese. About the 90% of iron/manganese oxide particles observed was smaller than 100 nm: about 67% were in the range 0-50 nm, 24% in the range 50-100 nm, only 9% in the range 100-210 nm.

This result is highly significant from a toxicological point of view: it is possible that, after inhalation, the van der Waals and electrostatic forces holding agglomerates together are at least partially disrupted, breaking agglomerates into their primary particle constituents or smaller agglomerates (Richman et al., 2011). It has already been reported in literature (Zimmer et al., 2002) that the arc welding activities represent a source of exposure to high amounts of fumes containing manganese, also in nanoparticle size. From a study population of welders, Racette et al. (2001) showed that some of them would develop Parkinsonism 17 years earlier if compared with the general population, thus placing the problem of understanding what was the penetration pathway of the metal into the inner brain structures and, in particular, inside the basal nuclei, the central nervous system

regions most involved in the genesis of the disease. In nano-form this metal can translocate through the olfactory tract reaching the brain, where it can cause a neurological disease called manganism, with Parkinson-like symptoms (Yu et al., 2000; McMillian, 2005).

Manganese enrichment in A-GTAW samples, if compared with M-GTAW ones, is in agreement with Moroni and Viti (2009) and Jenkins (2003) who report that it is a function of decreasing of magnetite-like particles size in welding fumes. For this reason, even if the time of direct exposure of workers to the fumes generated during the automatic process in the restrained area is brief, an effective local exhaust ventilation is necessary.

Another metal that can have an important role in lung toxicity is chromium, but in the case of automatic GTAW the size of chromium particles is higher reaching an average diameter of 1.276 μm. No chromium nanoparticles were found in aerosol sampled during the welding process.

In manual GTAW the pattern of particles changed: particles observed on TEM grids were mostly amorphous and irregular-shaped aggregates. In some cases these aggregates seem to be formed by thin and irregular plate-like particles overlapped and fused together. The most representative nanoparticles were constituted by iron/cobalt oxide, with an average diameter of 22 nm, and they were present inside aggregates of higher dimensions. As in the automatic welding, chromium was present only in bigger aggregates while no manganese oxide nanoparticles were found on TEM grids.

In our study particles, agglomerates and aggregates made of silicates were ubiquitous. On all collected TEM grids no fibres were found. The presence of silicates on A-GTAW and M-GTAW samples reflects in part the chemical composition of the welding wires (silicon was a component of the two kinds of wires), in part is due to the atmospheric particulate

matter of natural origin that was found also in BKD samples. For example aluminosilicates and phyllosilicates are widely used in constructions materials like plasters and paints. The fact that in BKD samples metal oxides particles like iron, manganese, cobalt and chromium oxides were not observed, confirms that the source of metal oxides was only the welding process.

Particles produced in both welding processes (automatic and manual) are respirable according to ISO-CEN (Organization for Standardization - European Committee for standardization) definition (CEN, 1993) but the most significant difference between the two sources of welding fumes that were investigated is the aggregation state of the particles found on TEM grids. The particles sampled during the automatic process had the smallest diameter in comparison with those sampled in the M-GTAW zone, were mostly nanosized and formed agglomerates chainlike. The particles found in the M-GTAW zone, instead, showed a larger diameter and were mostly aggregates. These results generate the hypothesis that even the same kind of welding process produces different classes of particles depending on the lifetime of the welding process. As a matter of fact, the automatic welding is a fast process in which the contact between the tungsten electrode, the filler wire and the material that has to be welded is brief. On the other hand, the automatic welding is performed inside a restrained area that workers cannot enter until the end of the welding process when they pick up the welded pieces to complete and refine them manually. In the manual process, the fume was generated by the welder who completed and refined the pieces treated in the automatic process (the operator welds a defined spot for a longer period of time respect to the automatic welding arm).

Our results on size and morphology of M-GTAW particles seem to be in contrast with Graczyk et al. (2016) who conducted the exposure assessment of apprentice welders

during aluminum manual GTAW in a ventilated exposure cabin to have a controlled setting. Regarding particle size distribution evaluated by means of particle sizers, they reported that at the breathing zone 92% of the particles had a geometric mean diameter below 100 nm and 50% of the particles was below 41 nm. Moreover, particles collected on TEM grids formed chainlike agglomerates of primary particles in the nanoscale.

On the contrary, in M-GTAW zone of our study we found mostly aggregate of particles that were not in the nanoscale. These differences can be due to the prevalence of the accumulation over the nucleation mechanism of particle formation and the influence of other industrial processes during our manual welding activity that was not performed in a controlled setting. In these terms, our results are substantially in agreement with Moroni and Viti (2009) who characterised GMAW fumes and pointed out the differences in aerosol composition in terms of particle size at variable distances from the welding chambers. The influence of the industrial setting resulted in greater particle size variability and larger particle size of welding fumes if compared with a controlled (laboratory) and/or confined setting. Moreover, Dasch and D'Arcy (2008) reported a size distribution mode for aluminum GMAW fumes in an automotive plant at 0.8 μm compared to 0.2-0.4 reported in literature for controlled settings.

For what concern the risk assessment during M-GTAW, it should be noticed that our sampling was performed at a distance of 0.5 m away from the welding task, not in the breathing zone where the particle number concentration could be actually higher as reported by Graczyk et al. (2016) who found that the mean particle number concentration at the breathing zone (inside the welding helmet) was 54% higher (1.69E+06 particles cm^{-3}) than at the near field location (0.6 m away from the welding task) confirming that the exposure increases with the decrease of the distance from the source and that a non-

ventilated welding helmet is not a sufficient protection measure. For this reason the particle number concentration and not only the particle size and morphology, has to be taken into account during manual welding as well.

1.5 Conclusions

Characterising dimensions, shape and composition of welding fumes particles is important to better understand how they can originate occupational diseases in welders with special attention to ultrafine particles.

Since in literature there are few studies that focus on GTAW fumes particles even though they are potentially the most hazardous ones in terms of occupational exposure, in this study two different real sources of GTAW fumes particles, collected in an automotive plant, were characterised by means of TEM-EDS and compared to a zone of the plant far from the two sources, used as a reference background.

All particles observed in this study are within the class of respirable particulate matter. The particles sampled during the automatic welding process had the smallest diameter in comparison with those sampled in the M-GTAW zone, were mostly nanosized, constituted by iron/manganese oxide and formed chainlike agglomerates. The particles found in the M-GTAW zone, instead, showed a larger diameter and were mostly aggregates that showed an X-ray spectrum characteristic of different kinds of silicates. Iron and cobalt oxides nanoparticles were present only inside bigger aggregates mainly composed of aluminum and titanium oxides.

These results generate the hypothesis that even the same kind of welding process produces different classes of particles depending on factors like the lifetime of the welding process. It was also demonstrated that chemical composition of the particles reflected the

composition of the mild steel used during the welding processes, meanwhile only particulate matter correlated to the building construction (as plaster) was found in BKD samples.

2. Ultrafine and submicron particles exposure assessment during the manufacturing of aluminium-based products: an integrated approach

2.1 Introduction

The study of UFPs emission during various operations in industrial settings is important to enhance knowledge on occupational diseases that may be related to it.

There are important gaps in the study of occupational exposure to NPs/UFPs in workplace scenarios and at present no standardised risk assessment protocol exists (Prodi and Larese, 2016).

In recent years it has been under discussion which metrics would be most relevant to monitor in relation to the exposure to ultrafine particles in workplaces (Brouwer et al., 2004). Mass concentration seems not to be a sufficient parameter to evaluate health hazard: particles in the nanometric range have a mass lower than particles of other dimensional classes but their number concentration can be very high as reported for GTAW process (Lehnert et al., 2012). Number concentration, size distribution, chemical composition and morphological characteristics of UFPs have to be considered in the risk assessment. The necessity of an approach for risk analysis on the workplaces that should be both comprehensive and simple is still an issue.

Despite the existence of several techniques which may be used together in a comprehensive risk assessment of NPs/UFPs in the workplace, such as surfaces or skin

wiping (Shepard and Brenner, 2014), carbon tabs used as interception method, tape sampling of skin and surfaces (Hedmer et al., 2015), and different air sampling techniques (Brouwer et al., 2004), very few of them have been utilized in real working conditions out of controlled environments.

Many processes performed in industrial settings such as smelting, welding, soldering, laser ablation, grinding, mixing, drilling, cutting and polishing (Wake et al., 2002; Zimmer and Maynard, 2002; Azarmi et al., 2014) are responsible for the emission of UFPs.

The aim of this study was to assess the exposure of workers to submicron and ultrafine particles in three industrial settings where aluminium was used as raw material for different applications.

The basic toxic data on nano-aluminium are scarce. The physical and chemical form of Al influence the uptake, accumulation and systemic bioavailability. The toxicity of different Al forms depends in large measure on their physical behaviour and relative solubility in water. Trivalent Al-induced formation of oxygen radicals accounts for the oxidative damage that leads to intrinsic cellular apoptosis. In contrast the toxicity of the insoluble Al oxides depends primarily on their behaviour as particulates (Willwhite et al., 2014). Toxicity studies have compared nano and micro particles of alumina, finding a much greater toxicity of the former (Zhang et al., 2013).

Aluminium containing welding fumes are mainly made of insoluble oxides (Al_2O_3). Riihimaki et al. (2008) estimated that only about 1 % of the inhaled aluminium welding fumes are rapidly absorbed by the lungs while it is assumed that smaller particles should be easier bioavailable. This kind of welding fumes are suspected to cause neurologic

disorders, with controversial results (Kiesswetter et al., 2007, 2009; Giorgianni et al., 2014).

In a series of tests to evaluate genotoxicity to brain tissues and bioaccumulation of aluminium oxide nanoparticles in various tissues of male albino rats (spleen, kidney, brain, intestine, liver), Morsy et al. (2016) concluded that acute doses generate a greater amount of uptake of aluminium by the spleen of rats while subacute doses accumulated mostly in the liver. The brain was the tissue with less amount of deposition. The results of comet assays showed significant increase in DNA percentage damage in the brain cells. Authors concluded that aluminium has high inclination to accumulate in tissues, in an extent that it is able to induce genotoxic effects: bioaccumulation is time, dose and organ dependant.

After having exposed rats to Al-NPs by nasal instillation, Kwon and coworkers (2013) suggested a dose-dependent increase in the presence of aluminium in the brain and in the olfactory bulb, demonstrating that nasal exposure to Al-NPs can allow the permeation of the substance in the brain via the olfactory bulb and modulate the gene and protein expression of mitogen activated protein kinases.

In this study an integrated approach for the exposure assessment was used in real workplace environments. Real-time measurements of number concentration and size of aerosol particles in the range 10-300 nm, sampling of respirable dust, sampling of particles on carbon tabs, surface wipe sampling, and skin tape stripping were performed to highlight the presence of submicron and UPFs and their characteristics. This integrated approach can help to better understand potential exposure in a real workplace context and possible health effects on workers.

2.2 Materials and methods

2.2.1 Sites and activities description

Three factories in which aluminium was used as raw material for different applications were chosen.

The first factory was committed to the assembling of aluminium parts for the cooling system in vehicles (Factory 1). In this factory the offices were in an area separated by two doors from the building in which the production takes place.

Along the production chain, components were assigned to 2-4 workers to perform manual oxy-fuel (O_2-GPL) welding operations. The filler material is an aluminium alloy rod (Al >70%, Si, Fe, Bi and other elements in traces) and the pickling agent is salts made of NaCl, KCl, LiCl and inorganic fluorides. In this factory the welding process was monitored.

In the second factory (Factory 2) die casting of aluminium was performed. The first step of the process consists in the melting, inside a melting oven, of bars mainly composed by Al (70-80%), Si (8-10%), Cu (2-4%), Zn and other metals in subpercentage. Then the molten metal is poured into a ladle and taken by operators to the degassing station. After these steps the molten metal is carried by operators to the die casting machine for the manufacturing of the final products. At the end of the process the products are moved to the quality control position where operators pick up the products for the selection and packaging. Three times a day the melting oven is cleaned from the slags by workers. In this factory the exposure of workers along all the production chain was monitored taking into account that the main sources of dustiness were: (i) the melting process, (ii) the degassing of the molten metal and (iii) the cleaning procedure performed on the melting oven.

In the third factory (Factory 3) aluminium was vacuum deposited on polypropylene food packaging films. The metalisation process is monitored by an operator inside a control cabin and performed by a machine formed by two parts in which (i) aluminium wires are heated till evaporation and then (ii) vacuum condensed on cold polypropylene films. After the metalisation process the two parts of the machine are cleaned using boron nitride as release agent. In this factory the exposure of workers was monitored mainly during the cleaning process of the machine.

2.2.2 Air monitoring and sampling

Air monitoring and sampling were conducted over 3 non-consecutive working days in Factory 1 and 2, over 2 non- consecutive working days in Factory 3.

2.2.2.1 Real-time measurements

A miniature diffusion size classifier (DiSCmini, Matter Aerosol) was used to measure the number concentration and mean diameter of particles in the range 10-300 nm. Flow rate and sampling time interval were 1 L min^{-1} and 1 second respectively.

The position of the instrument, the kind of process monitored and the duration of the measurements are reported in Table 1.2.1 for each factory.

Table 1.2.1 Details about the position of the DiSCmini, the kind of process monitored and the duration of the measurements for each factory.

Factory	Position	Monitored process	Average duration (hours)
Factory 1	In the offices area	Background	1 h 15 min
	2 m from the welding position	Welding process	6 h 37 min
Factory 2	Open area between the degassing station and the melting oven	Production chain during die casting process	7 h
Factory 3	Inside the control cabin	Background	1 h 20 min
	Open area between the two parts of the machine performing metalisation	Cleaning of the machine performing metalisation	3 h

2.2.2.2 Sampling of respirable dust

Respirable particles were collected on mixed cellulose ester filters (MCE) (0.45 µm pore size, 25 mm diameter, Whatman GmbH, Germany) by means of SKC GS-3 Cyclone samplers (model no. 225-103) for respirable dust (50% cut point for 4 µm aerodynamic diameter) connected to Tecora AYRON 5 pumps set to a flow rate of 2.75 L min^{-1}. Cyclones were clipped in the breathing zone of the workers and pumps were waist-secured by a belt. The position of the instrument, the kind of process monitored and the duration of the sampling are reported in Table 1.2.2 for each factory.

Table 1.2.2 Details about the position of the sampler for respirable dust, the kind of process monitored and the duration of the measurements for each factory.

Factory	Position	Monitored process	Average duration (hours)	Number of samples
Factory 1	Breathing zone of the welders	Welding process	6 h	4
Factory 2	Breathing zone of the workers	Production chain during die casting process	7 h	5
Factory 3	Breathing zone of the workers	Cleaning of the machine performing metalisation	3 h	4

2.2.2.3 Sampling of respirable dust on TEM grids

In Factory 1 and 2, the same samplers used in the breathing zone of workers to collect respirable particles on filters were also used, but not at the same time, to collect particles to be later characterised by means of a transmission electron microscope coupled with an energy-dispersive X-ray analytical system (TEM-EDS). The sampler contained a 5 µm MCE filter in the filter cassette. Under this filter that blocks particles larger than 5 µm, three TEM supports (200 mesh copper grids coated with a 20 nm carbon support film, Media System Lab, Italy) were placed to collect particle fraction with dimensions lower than 5 µm. Sampling period ranged from 30 to 50 min and 6 TEM grids were collected in each factory.

2.2.2.4 Sampling of particles using a cascade impactor

In Factory 3 a Sioutas Cascade Impactor (SKC) was used to collect particles both on MCE filters for the quantitative analysis of metal content and on TEM grids for morpho-chemical evaluations. In the second case a TEM grid was placed on "D" impactor stage to collect the aerosol fraction 0.25-0.50 µm. To secure the grid, a properly sized square section was cut from the adhesive area of 3M Post-it ® Notes and glued on the MCE impaction substrate. The adhesive portion faced upward and secured the grid in place. In this way, the grid was easily removed without damage after sampling for TEM analysis (Birch et al., 2011) (Fig. 1.2.1).

The instrument was secured about 1.80 m off the ground in the open area between the two parts of the machine performing metalisation. Sampling lasted 2 hours/day in order to collect about 1,000 L of air with a flow rate of 9 L min^{-1}.

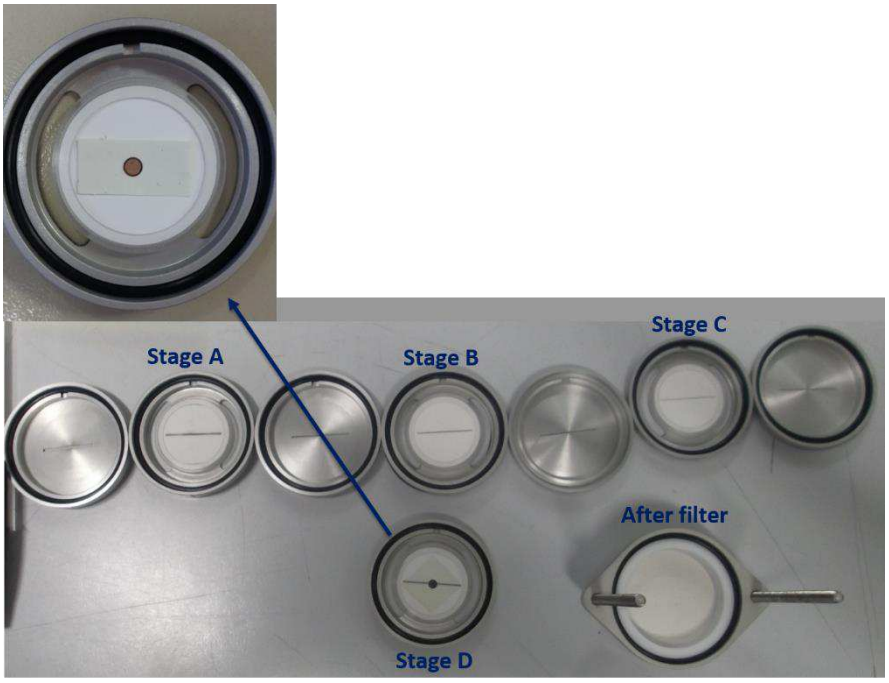

Figure 1.2.1 Image of the impaction stages (A-After filter) with a focus on the positioning of a TEM grid (on the top).

2.2.3 Monitoring of surface and skin contamination

Monitoring of surface and skin contamination was conducted over 3 non-consecutive working days in Factory 1 and 2, over 2 non-consecutive working days in Factory 3.

2.2.3.1 Carbon tabs

Carbon tabs (Agar Scientific Ltd Stansted UK) are double-sided adhesive tabs used as an interception sampler for bulk and dispersed powders to be later characterised by means of a scanning electron microscope coupled with an energy-dispersive X-ray analytical system (SEM-EDS) obtaining qualitative and morphological information on particles (Fig. 1.2.2). In each factory, after the cleaning of selected working surfaces, carbon tabs have been applied on surfaces at various distances from emission sources (10 carbon tabs per 3 days on average) and in the case of Factory 1 also over the gloves worn by workers (3 per 3 days).

The selected working surfaces were: control consoles and protective barriers of the welding positions in Factory 1, various areas on the surface of the degassing station and of the melting oven in Factory 2, different points of the outside surface of the machine performing metalisation and working surfaces near it in Factory 3.

Exposure time was the full work shift (6 hours on average for Factory 1 and 2, 4 hours for Factory 3). At the end of the work shift carbon tabs were removed carefully using tweezers in order to avoid further contamination or loss of deposited substance and properly stocked in polypropylene boxes till further analysis.

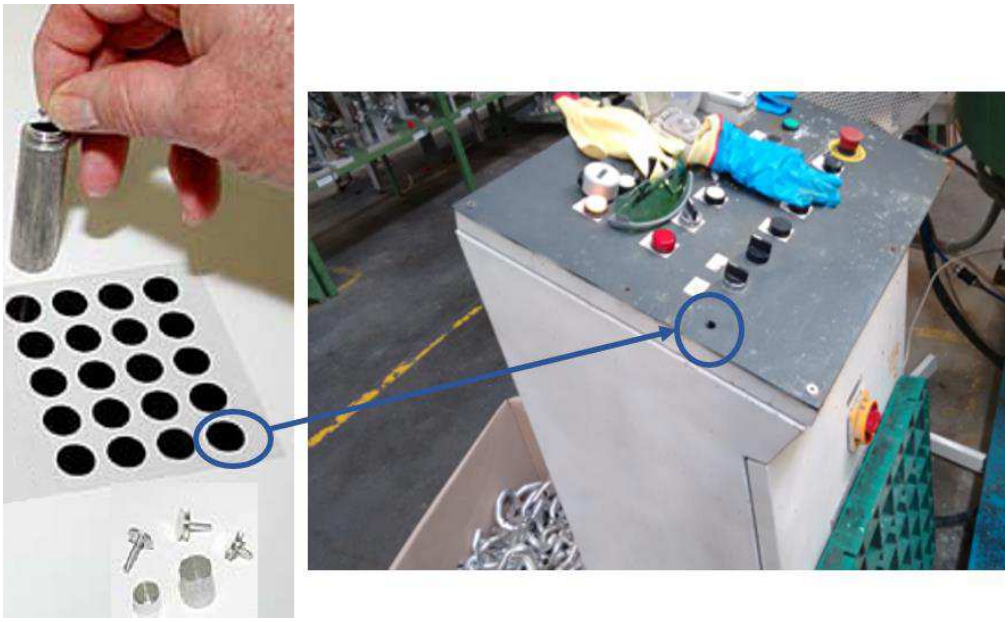

Figure 1.2.2 Image of the positioning of carbon tabs.

2.2.3.2 Wipe samples

The surface wiping technique consists in the removal of contamination from a 100 cm^2 area (10 cm x 10 cm). Wipe sampling was performed on the same surfaces on which carbon tabs were applied. Areas were cleaned before the work-shift by swiping it through a cellulose-made swab soaked with 1% HNO_3 solution with an adequate external force. At the end of the work shift, surfaces were wiped according to American Society for Testing Materials (ASTM) International, D-6966-08 procedure. On average 10 wipe samples were collected in each factory. All wipe samples underwent chemical analysis to detect Al concentration.

2.2.3.3 Skin tape stripping

Tape stripping allows the removal of the cell layers of the stratum corneum (SC) and contaminating particles. The protocol of tape stripping may be derived from the international literature (Lademann et al, 2009). However, the use of a full tape stripping

protocol may be difficult in an occupational context: the protocol requires a long amount of time, a well-trained operator, technical appliances to determine the right number of strips for each tested worker and may cause temporary discomfort to the tested volunteers (redness of skin, itching, skin colour alteration) which might last for some days/weeks after the procedure until the SC is fully restored.

An approach which can lead to a good approximation of the contamination, limiting most of the issues of a full-scaled protocol, may involve 1-3 consecutive stripping just to assess the external SC contamination.

Round adhesive tape discs (polyacrylate ester adhesive, 3.80 cm^2, D-Squame; CuDerm, Dallas, TX, USA) were used (Fig. 1.2.3). One tape sample (three consecutive stripping) was taken for each worker (6 workers for each factory on average) from the volar surface of the exposed forearm in Factory 1 and from an exposed area of the neck of workers in Factory 2 and 3. None of the workers cleaned the selected skin surface till the end of the work shift (on average 6 hours).

With the same method skin tape stripping was performed also on non-exposed volunteers in order to have a comparison.

Tape discs underwent chemical analysis to detect Al concentration.

Figure 1.2.3 Image of the skin tape stripping procedure.

2.2.4 Analysis of collected samples

2.2.4.1 Analysis of filter samples

All filters were digested with 3 mL of nitric acid (≥ 69%, trace select) in Teflon pressure vessels by means of a microwave-assisted digestion system (Multiwave PRO, Anton Paar) following the heating program reported in Table 1.2.3.

Inductively coupled plasma atomic emission spectroscopy (ICP-AES) was used for the quantitative determination of the filter samples aluminium content (PerkinElmer Optima 8000 with autosampler S10).

Table 1.2.3 Heating program for the microwave-assisted digestion procedure.

Step	Program	Temperature (°C)	Time (mm:ss)
1	Temperature ramp	200	12:00
2	Temperature hold		40:00
3	Cooling	50	25:00

After complete dissolution, samples were diluted to 15 mL with MilliQ water. The obtained solutions were analysed for total aluminium concentration. Analyses were conducted using a calibration curve, obtained by dilution of aluminium standard solutions for ICP-AES analyses. The limit of detection (LOD) for aluminium was 0.020 mg L^{-1} at the analytical wavelength of 396.153 nm. The precision of the measurements as repeatability (RSD %) for the analysis was always less than 5%.

2.2.4.2 Wipe and tape samples analysis

Wipe and tape samples were placed in crucibles and heated up to 500 °C for 5 hours in a muffle furnace. Resulting ash was solubilised following the microwave-assisted acid

digestion procedure previously described and diluted to a final volume of 15 mL with MilliQ water. Obtained solutions were analysed for total aluminium concentration by means of ICP-AES (same experimental parameters).

2.2.4.3 SEM-EDX investigations

Surface conditions were examined using SEM. Carbon tabs were mounted on aluminium stubs. SEM analysis was performed by means of a FEI Quanta250 SEM operating in secondary electron detection mode. Working distance was adjusted in order to obtain the suitable magnification, the accelerating voltage was 30kV.

Elemental composition of the scaffolds was determined using an EDS probe (Quanta250 FEI with EDAX probe, Hillsboro, OR, USA). Accelerating voltage varied between 10 and 30kV; both spot-size and fullframe acquisition were made at a varying time from 5 to 15 min.

2.2.4.4 TEM-EDS investigations

A JEOL (JEM 3010) electron microscope operating at 300 kV, with a point-to-point resolution of 0.17 nm, equipped with a 749 CDD Gatan Camera, coupled with an energy dispersive X-ray analyser (Oxford Instr., EDS-6636), was used to provide a detailed morpho-chemical characterisation (size distributions, shapes, microchemical data and structural information) of particles collected on TEM grids. TEM images were processed using ImageJ program.

2.3 Results

2.3.1 Air monitoring and sampling

2.3.1.1 Real-time measurements

Factory 1

Table 1.2.4 summarises the particle number concentration (PNC) and particle size in the offices area (background-BKD) and in the factory at the emission source during day 1, 2 and 3. Differences between the results obtained in day 1 and 2 and those obtained in day 3 are probably due to the intrinsic variabilities occurring in a real occupational context.

Table 1.2.4 Results obtained in Factory 1 for particle number concentration (maximum, mean and standard deviation SD, median) and particle size (mean and SD).

Factory 1	Particle number concentration (particles/cm^3)			Particle size (nm)
	Maximum	Mean (SD)	Median	Mean (SD)
BKD	17,601	9,811 (1,268)	9,951	62 (4)
Factory day 1	1,141,016	72,848 (73,068)	44,716	36 (7)
Factory day 2	779,417	61,673 (38,146)	51,881	39 (5)
Factory day 3	772,044	115,013 (41,514)	109,093	27 (3)

Figure 1.2.4 shows the data acquired in the background (BKD) (1 h and 15 minutes) and in the factory, showing the temporal evolution of particle number concentration and

particle size in day 2: generally, an increase of the former corresponds to a decrease of the latter, resulting in two specular profiles.

The difference between these two parameters in the offices area and in the factory near the emission source is clear. The average values changed from approximately 10,000 particles cm^{-3} and 60 nm to approximately 50,000 particles cm^{-3} and 40 nm respectively.

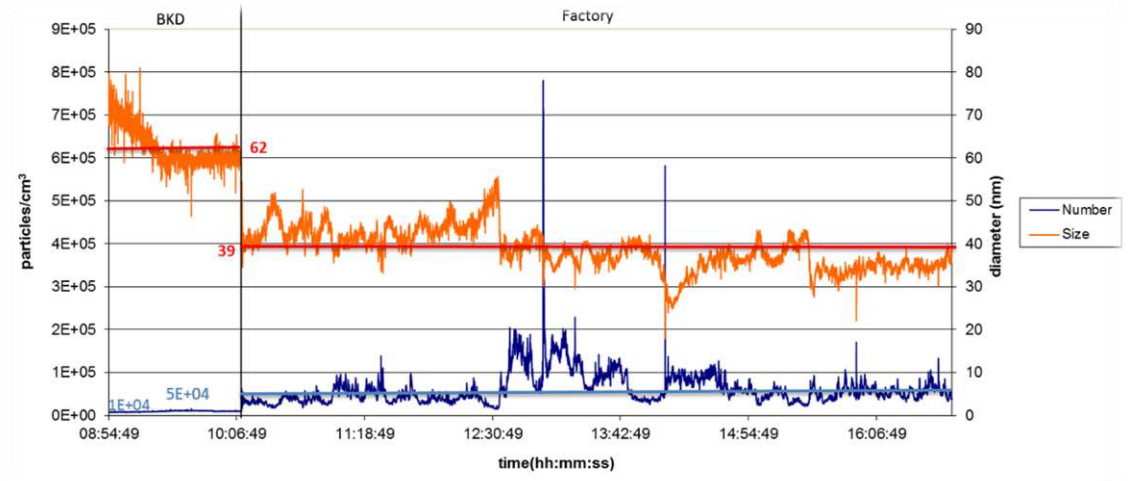

Figure 1.2.4 Temporal evolution of PNC and particle size in the BKD site and in Factory 1 at the emission source during day 2. Red lines: mean values of particle size (BKD and factory). Light blue lines: median values of PNC (BKD and factory).

Factory 2

Table 1.2.5 summarises the PNC and particle size in the factory at the emission source during day 1, 2 and 3.

Figure 1.2.5 shows a representative temporal evolution of particle number concentration and particle size in the factory (day 2). Peaks off the scale have been graphically hidden in order to better appreciate the main profile. These peaks in number and size are due to the saturation of the instrument.

Table 1.2.5 Results obtained in Factory 2 for particle number concentration (maximum, mean and standard deviation SD, median) and particle size (mean and SD).

Factory 2	**Particle number concentration (particles/cm^3)**			**Particle size (nm)**
	Maximum	Mean (SD)	Median	Mean (SD)
Factory day 1	5,336,106	248,990 (124,715)	237,597	34 (7)
Factory day 2	7,089,475	392,637 (268,103)	352,576	32 (12)
Factory day 3	7,894,972	572,325 (440,488)	415,872	32 (9)

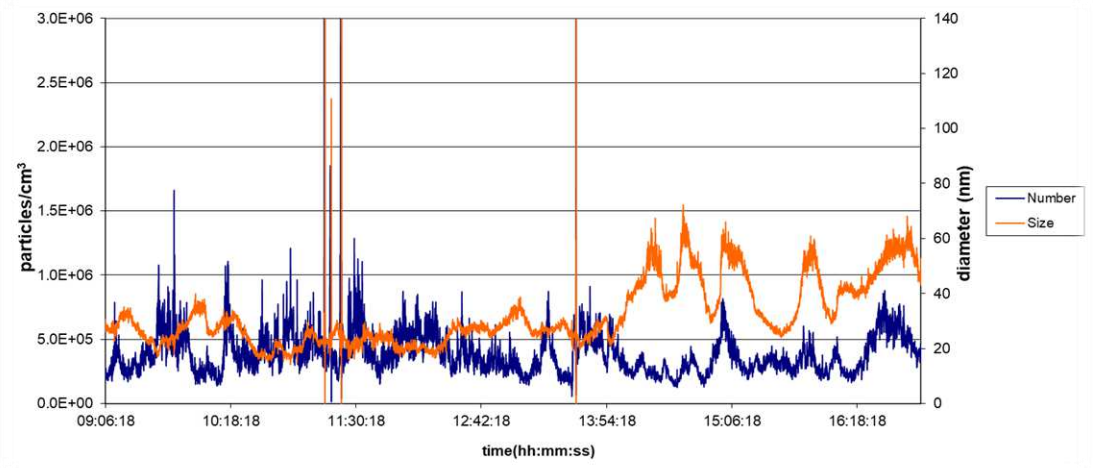

Figure 1.2.5 Temporal evolution of PNC and particle size in Factory 2 during day 2. Peaks off the scale have been graphically hidden in order to better appreciate the main profile.

Table 1.2.6 summarises the PNC and particle size in the factory at the emission source during day 1, 2 and inside the control cabin for a comparison.

Table 1.2.6 Results obtained in Factory 3 for particle number concentration (maximum, mean and standard deviation SD, median) and particle size (mean and SD).

Factory 3	Particle number concentration (particles/cm^3)			Particle size (nm)
	Maximum	Mean (SD)	Median	Mean (SD)
Control cabin	74,013	12,426 (4,170)	11,758	91 (12)
Factory day 1	5,284,233	41,954 (103,473)	30,884	68 (17)
Factory day 2	2,984,167	56,624 (141,729)	26,489	47 (23)

Figure 1.2.6 shows a representative temporal evolution of particle number concentration and particle size in the factory (day 1). Peaks off the scale have been graphically hidden in order to better appreciate the main profile.

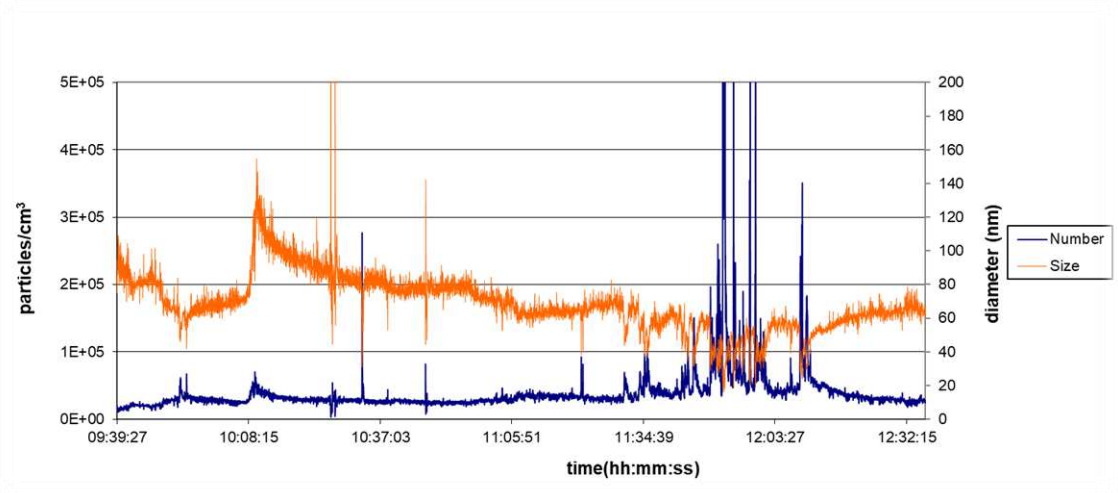

Figure 1.2.6 Temporal evolution of PNC and particle size in Factory 3 during day 1. Peaks off the scale have been graphically hidden in order to better appreciate the main profile.

As shown in Table 1.2.6, inside the control cabin PNC was more two times lower than in the open area between the two parts of the machine performing the metalisation of the polymeric films. On the contrary, particle size was higher inside the cabin than outside.

2.3.1.2 Filter samples

The results of the quantitative analysis on filters collected in each factory by means of cyclones for respirable dust are reported in Table 1.2.7 as mean values over non-consecutive sampling days.

Table 1.2.7 Mean aluminium concentration in filter samples (respirable dust) collected in the factories. n= number of filters analysed by means of ICP-AES for each factory.

	Al µg/m^3 (respirable dust)
Factory 1 (n=4)	1.833
Factory 2 (n=5)	4.367
Factory 3 (n=4)	73.23

In Factory 3, in addition to cyclones for respirable dust, a cascade impactor was used to have data on aluminium distribution on the impactor stages corresponding to different size ranges of the particles collected (< 0.25 µm: after filter, 0.25–0.50 µm: Stage D, 0.5–1.0 µm: Stage C, 1.0–2.5 µm: Stage B, and 2.5–10 µm: Stage A). Aluminium concentration, depending on the sampling day, ranged from 13.631 to 103.8 µg m^{-3} on Stage A, from 4.037 to 20.39 µg m^{-3} on Stage B, from 1.386 to 8.770 µg m^{-3} on Stage C, from 1.226 to 6.231 µg m^{-3} on Stage D and from 1.970 to 5.757 µg m^{-3} on the after filter.

The aluminium distribution in the different size ranges expressed in terms of percentage is shown in Fig. 1.2.7.

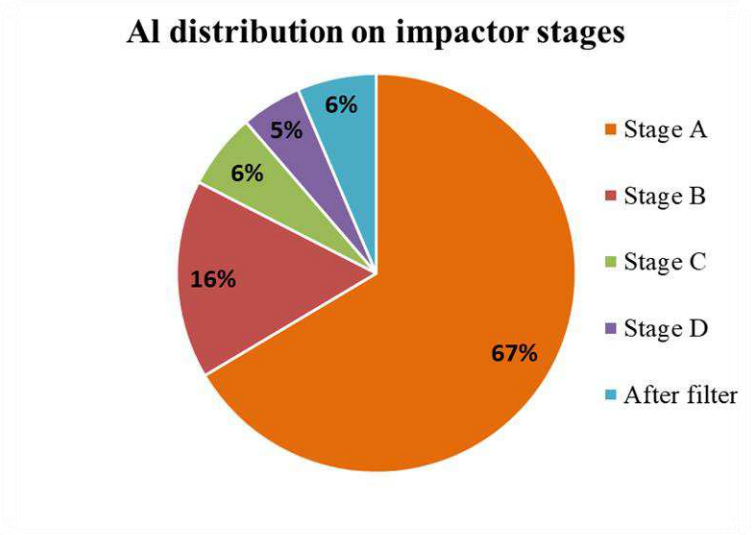

Figure 1.2.7 Aluminium distribution (percentage) on the stages of the cascade impactor used in Factory 3.

2.3.1.3 TEM-EDS investigations

During TEM-EDS investigations, the chemical composition of the grid must be taken into account. In all the following EDS spectra the peaks related to C, Cu and Ni are due to the material of the grid.

Factory 1

On the grids collected during the welding activity, nano (<20nm) and submicron particles, agglomerates and aggregates containing mainly Al, Br and Si were observed (Fig. 1.2.8 and 1.2.9). Br could be an impurity in the pickling agent as well as Bi that is present in some EDS spectra. Bi could also be present in the aluminium alloy as well as Si.

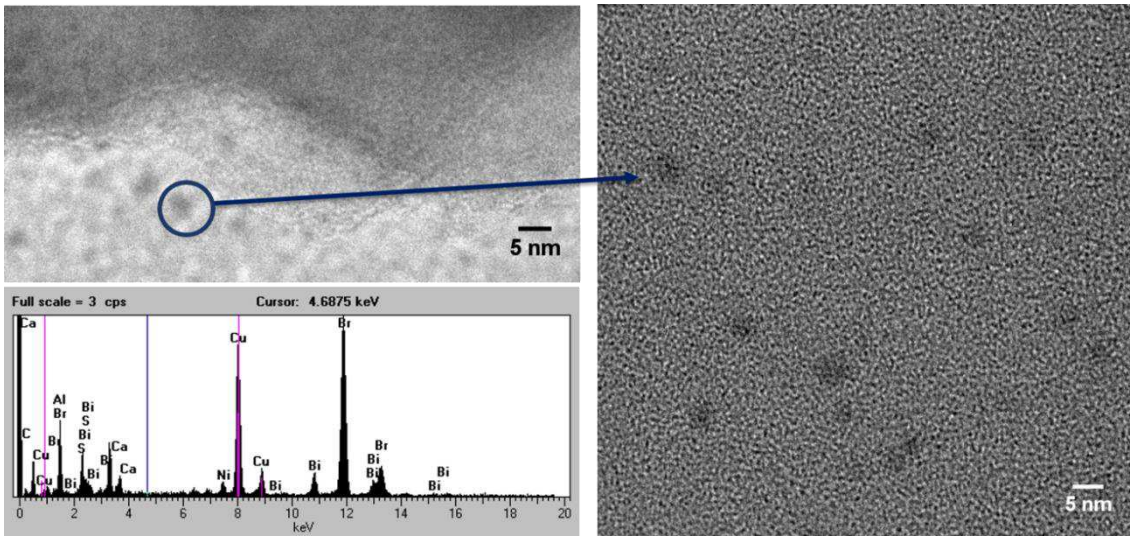

Figure 1.2.8 Representative TEM images and EDS spectrum of particles found on a TEM grid collected in Factory 1. Scale bar: 5 nm. Spectrum refers to an aluminium-containing compound.

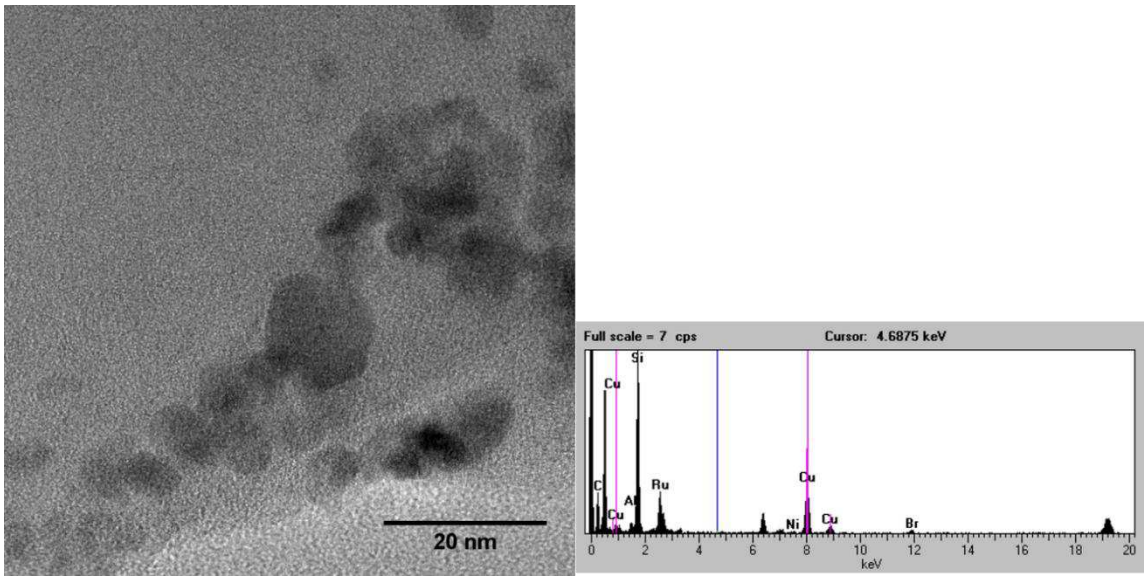

Figure 1.2.9 Representative TEM image and EDS spectrum of an agglomerate of particles found on a TEM grid collected in Factory 1. Scale bar: 20 nm. Spectrum refers to an aluminium-containing compound.

Factory 2

On the grids collected during the production chain involving die casting, particles in the range 20-500 nm containing Al were observed (Fig. 1.2.10 and 1.2.11). Using higher magnifications these particles appear as agglomerates of nanoparticles. Moreover, submicron particles and aggregates containing mainly Al, Si and Br were observed. Chemical composition of particles is consistent with the aluminium alloy used.

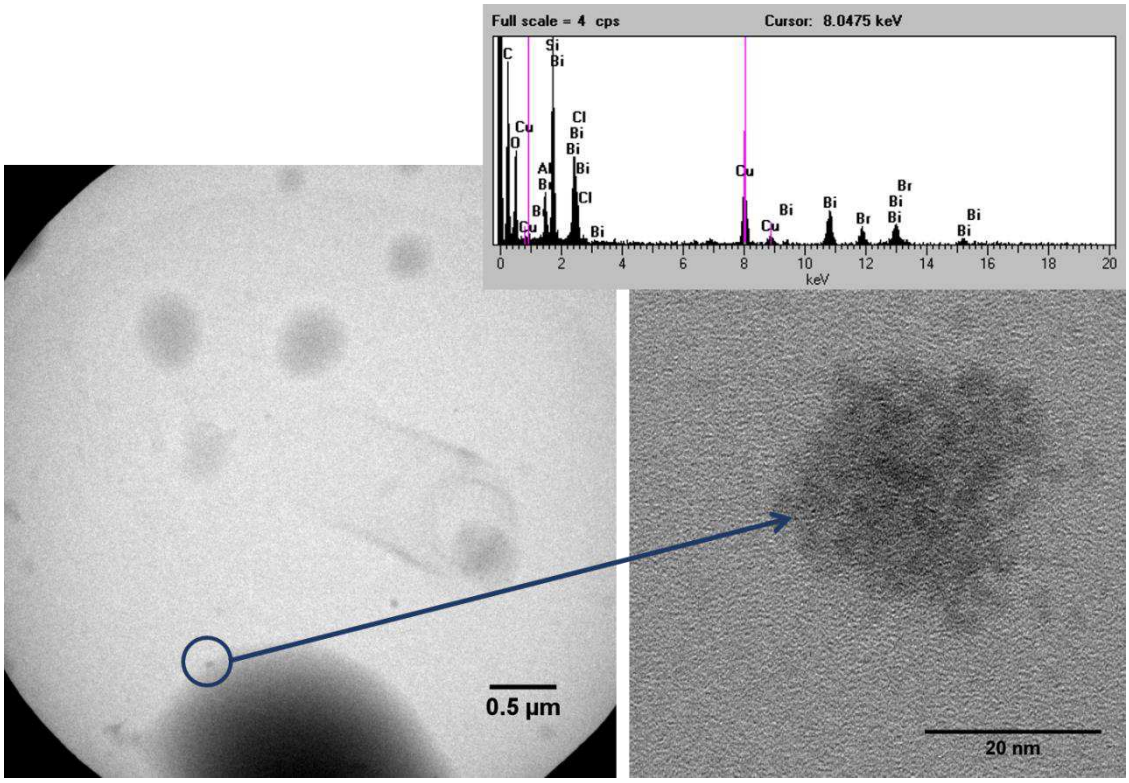

Figure 1.2.10 Representative TEM images and EDS spectrum of agglomerates of particles found on a TEM grid collected in Factory 2. Scale bar: 500 nm (image on the left), 20 nm (image on the right). Spectrum refers to an aluminium-containing compound.

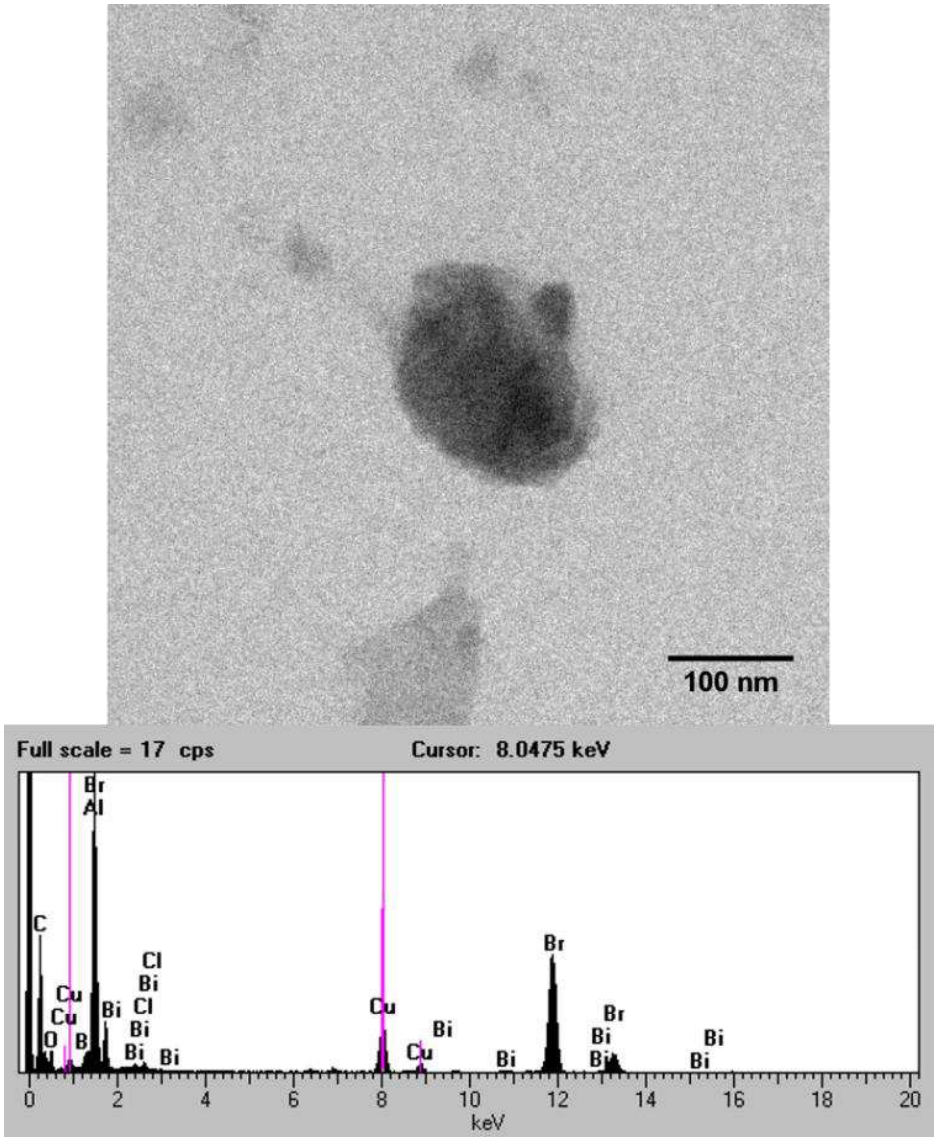

Figure 1.2.11 Representative TEM image and EDS spectrum of a particle found on a TEM grid collected in Factory 2. Scale bar: 100 nm. Spectrum refers to an aluminium-containing compound.

Factory 3

On the grids collected during the cleaning of the machine performing metalisation of polymeric films, particles of irregular shape in the micron range (1 μm and over) seems to overlap each other. Beside this kind of micro particles some particles in the nanoscale were observed (Fig. 1.2.12).

Some aggregates in the size range 1-5 μm seem to be formed by thin and irregular plate-like particles overlapped and fuse together (Fig. 1.2.13).

All particles are mainly constituted by Al as can be seen from EDS spectra.

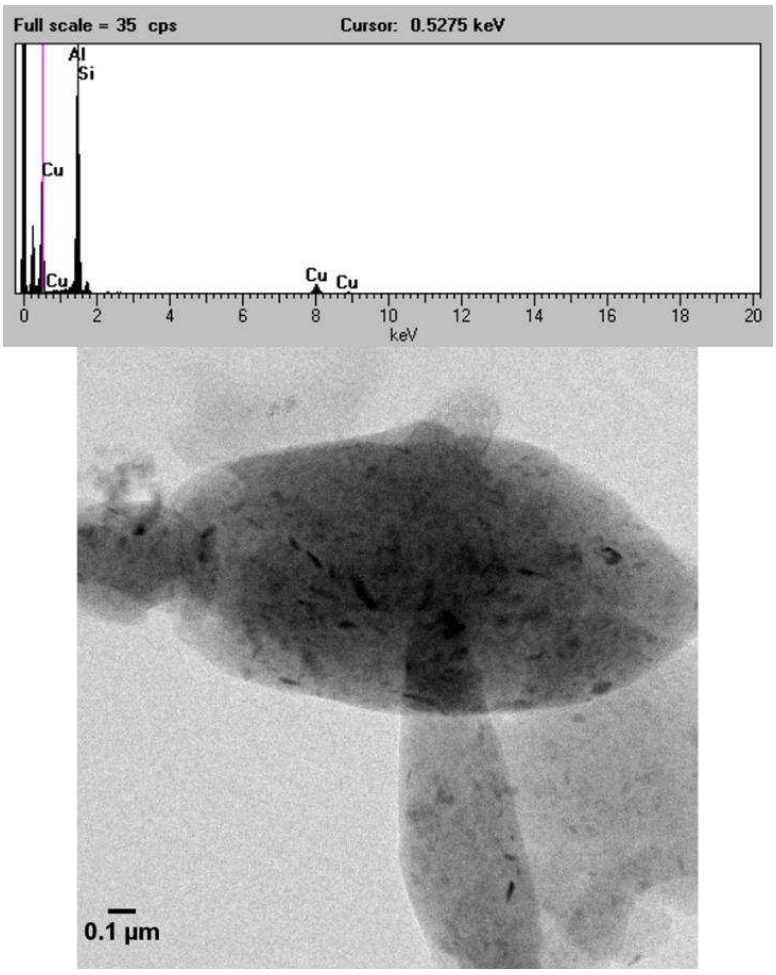

Figure 1.2.12 Representative TEM image and EDS spectrum of particles found on a TEM grid collected in Factory 3. Scale bar: 100 nm. Spectrum refers to an aluminium-containing compound.

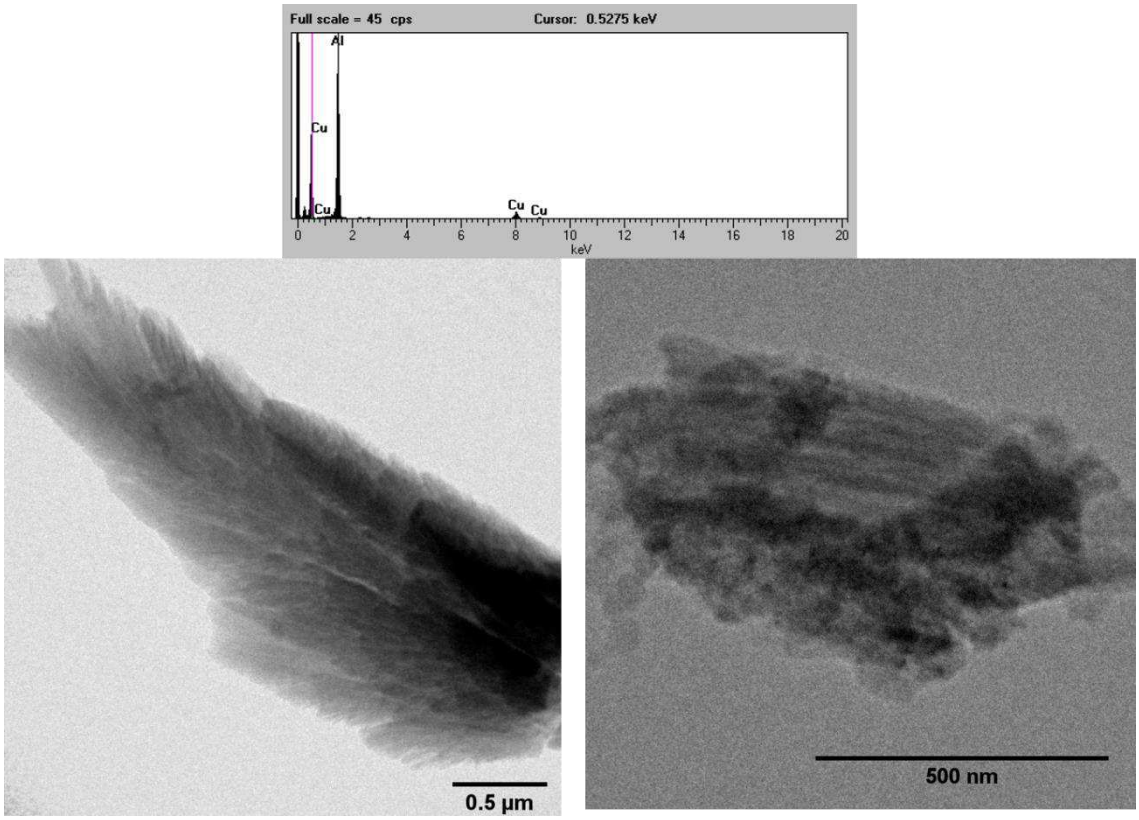

Figure 1.2.13 Representative TEM images and EDS spectrum of aggregates of plate-like particles found on a TEM grid collected in Factory 3. Scale bar: 500 nm. Spectrum refers to an aluminium-containing compound.

2.3.2 Surface and skin contamination

2.3.2.1 Carbon tabs

Factory 1

SEM-EDS analysis of the carbon tabs placed on the gloves of workers performing welding activity have shown the presence of aggregates/agglomerates in the micron range. Some of these micro aggregates were constituted by submicron particles. The chemical composition of the particles (Al, Fe, Na, Cl and K) is consistent with the composition of the Al alloy rod and of the pickling agent (Fig 1.2.14).

It is plausible that smaller particles dispersed in air tend to aggregate/agglomerate forming structures of higher dimensions and depositing on surfaces.

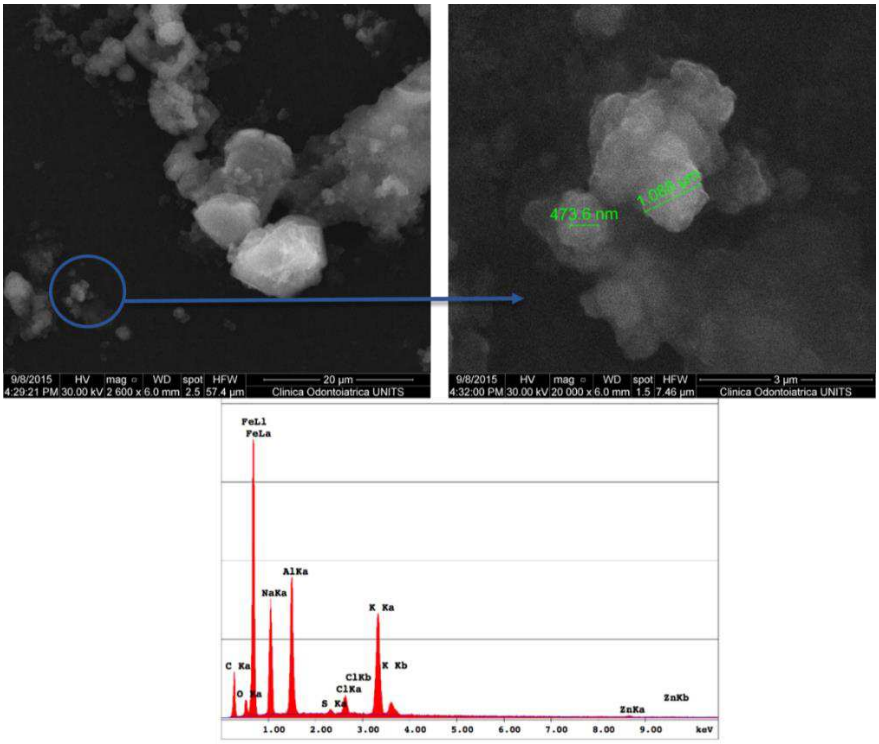

Figure 1.2.14 SEM images and EDS spectrum of aggregates/agglomerates of particles found on carbon tabs placed on the gloves of welders in Factory 1. Scale bar: 20 µm (image on the left), 3 µm (image on the right). Spectrum refers to an aluminium-containing compound.

SEM-EDS analysis of the carbon tabs placed close to the workers on protective barriers of the welding position have shown the presence of various kinds of aggregates. Some of them, cube-shaped, were probably salts (NaCl, KCl) from the pickling agent used during the welding activity. At higher magnification aggregates of quasi-spherical nanoparticles (90-100 nm) were observed. In this case the chemical composition of the particles is coherent with the composition of the Al alloy rod and of the pickling agent (Fig. 1.2.15) as well.

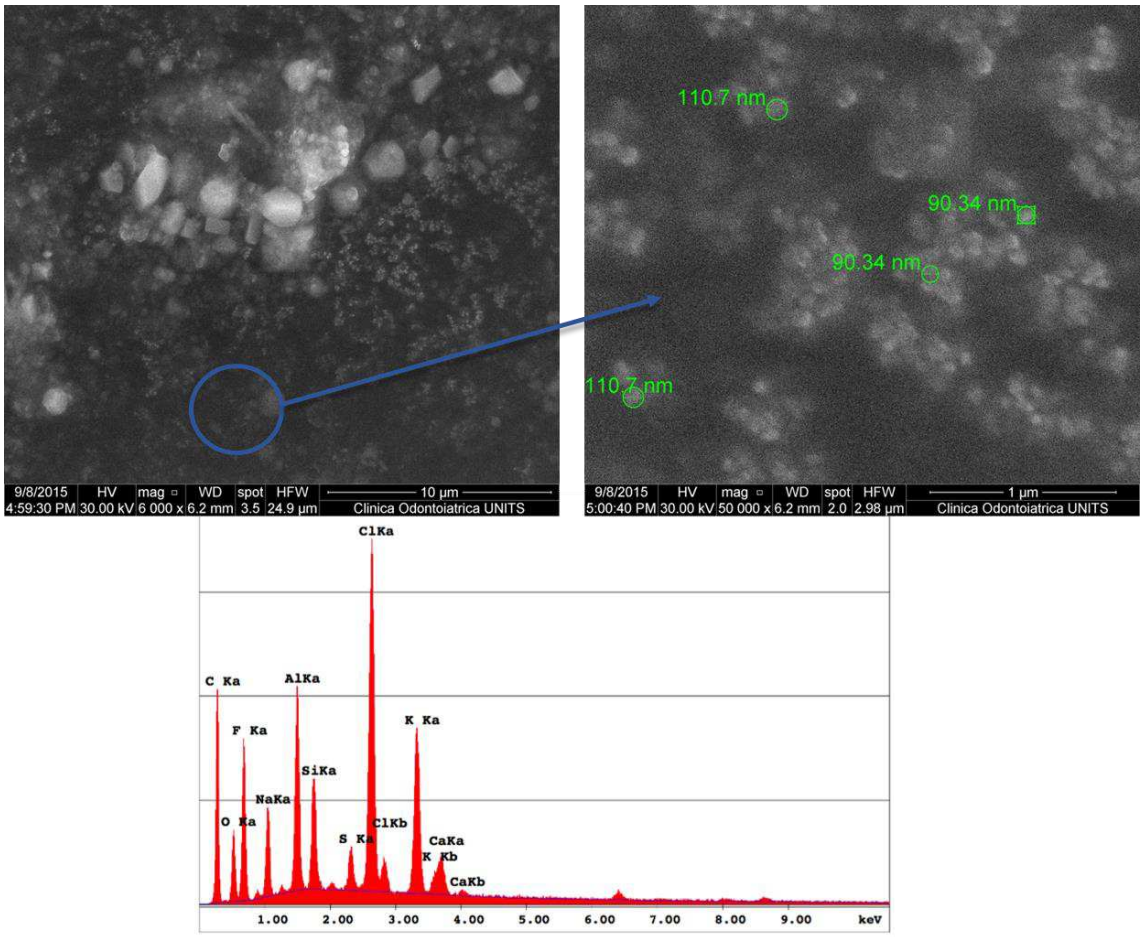

Figure 1.2.15 SEM images and EDS spectrum of aggregates of nanoparticles found on carbon tabs placed on protective barriers of the welding position in Factory 1. Scale bar: 10 µm (image on the left), 1 µm (image on the right). Spectrum refers to an aluminium-containing compound.

Factory 2

SEM-EDS analysis of the carbon tabs placed on the degassing position revealed the presence of aggregates in the size range 50-200 µm constituted of particles with dimensions between approximatively 1 and 20 µm (on the top of Fig 1.2.16).

Around them aggregates of quasi spherical nanoparticles (80-120 nm) were found (on the bottom of Fig 1.2.16).

The most prevalent element on the tabs was Al, followed by Na and Cl, even though in relative small quantities.

.

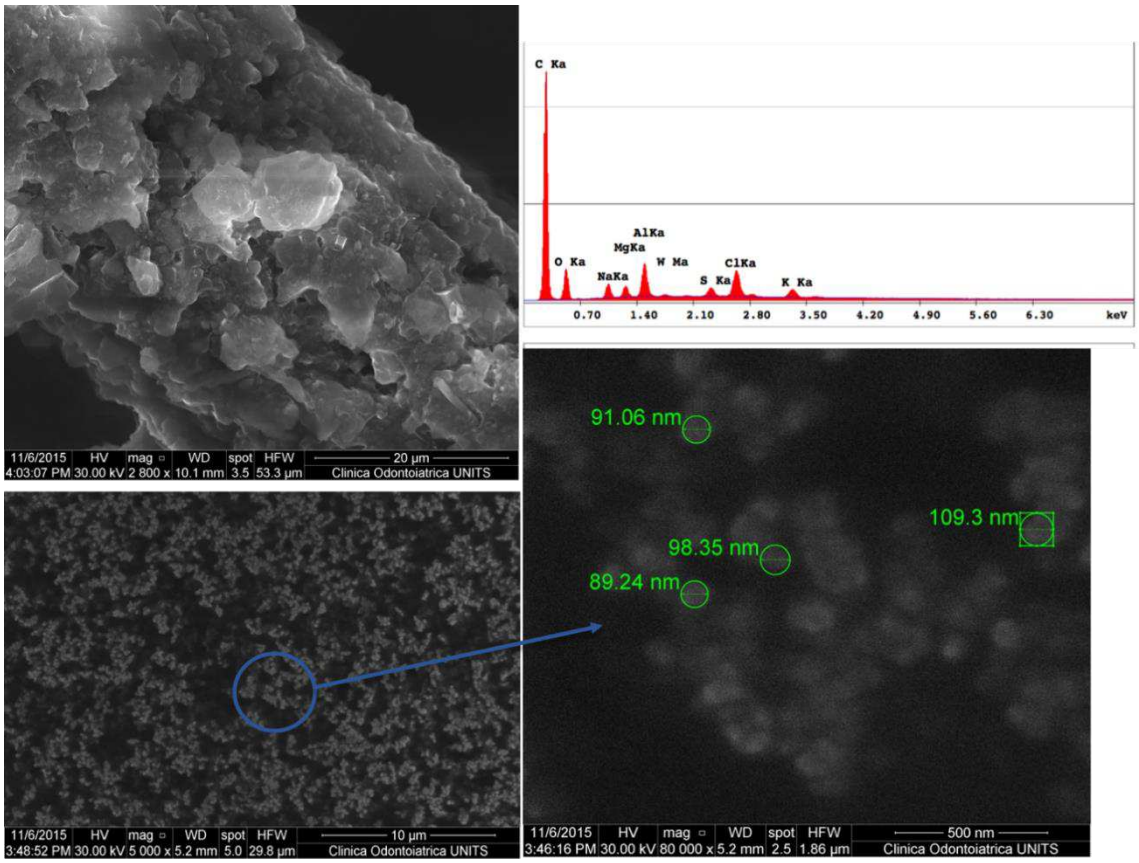

Figure 1.2.16 SEM images and EDS spectrum of aggregates of particles found on carbon tabs placed on the degassing position in Factory 2. Scale bar: 20 µm (image on the top), 10 µm (image left-bottom), 500 nm (image right-bottom). Spectrum refers to an aluminium-containing compound.

In Fig 1.2.17 an aggregate of particles with the major dimension of about 70 µm that is mainly composed of Al can be seen. At higher magnifications micro and submicron particles similar to fibres can be observed. This kind of aggregates were found on carbon tabs placed close to the melting oven where two important phases of the die casting production cycle occur: the pouring of the molten aluminium inside a ladle and the cleaning of the oven. The latter operation is particularly dusty.

All around these aggregates, quasi-spherical nanoparticles like these shown on the bottom of Fig 1.2.16 were observed. The most prevalent element on the tabs was Al.

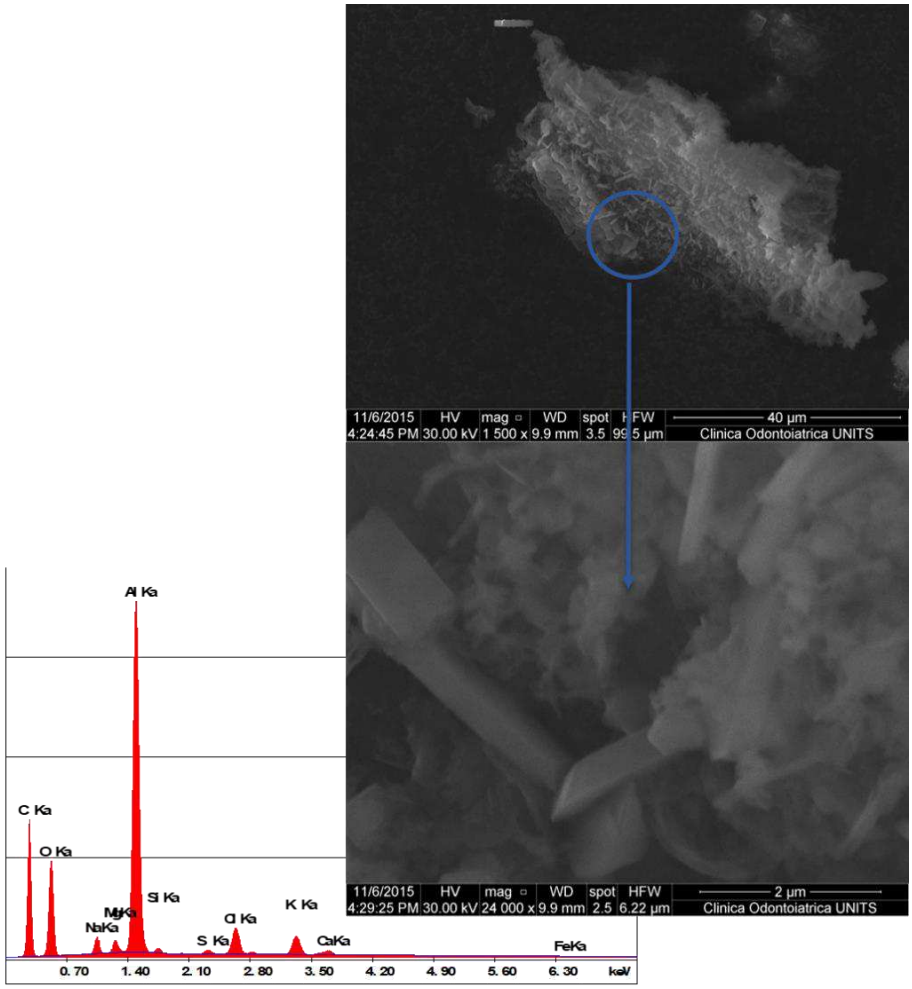

Figure 1.2.17 SEM images and EDS spectrum of aggregates of particles found on carbon tabs placed close to the melting oven in Factory 2. Scale bar: 40 µm (image on the top), 2 µm (image on the bottom). Spectrum refers to an aluminium-containing compound.

Factory 3

Particles with irregular shapes and, in some cases, needle-like particles were found on carbon tabs placed on different points of the outside surface of the machine performing metalisation. The dimensions of these particle mainly composed of Al were between 10 and 200 µm (Fig. 1.2.18).

Other aggregates of micro and submicron particles mainly composed of Al were sporadically observed (Fig. 1.2.19).

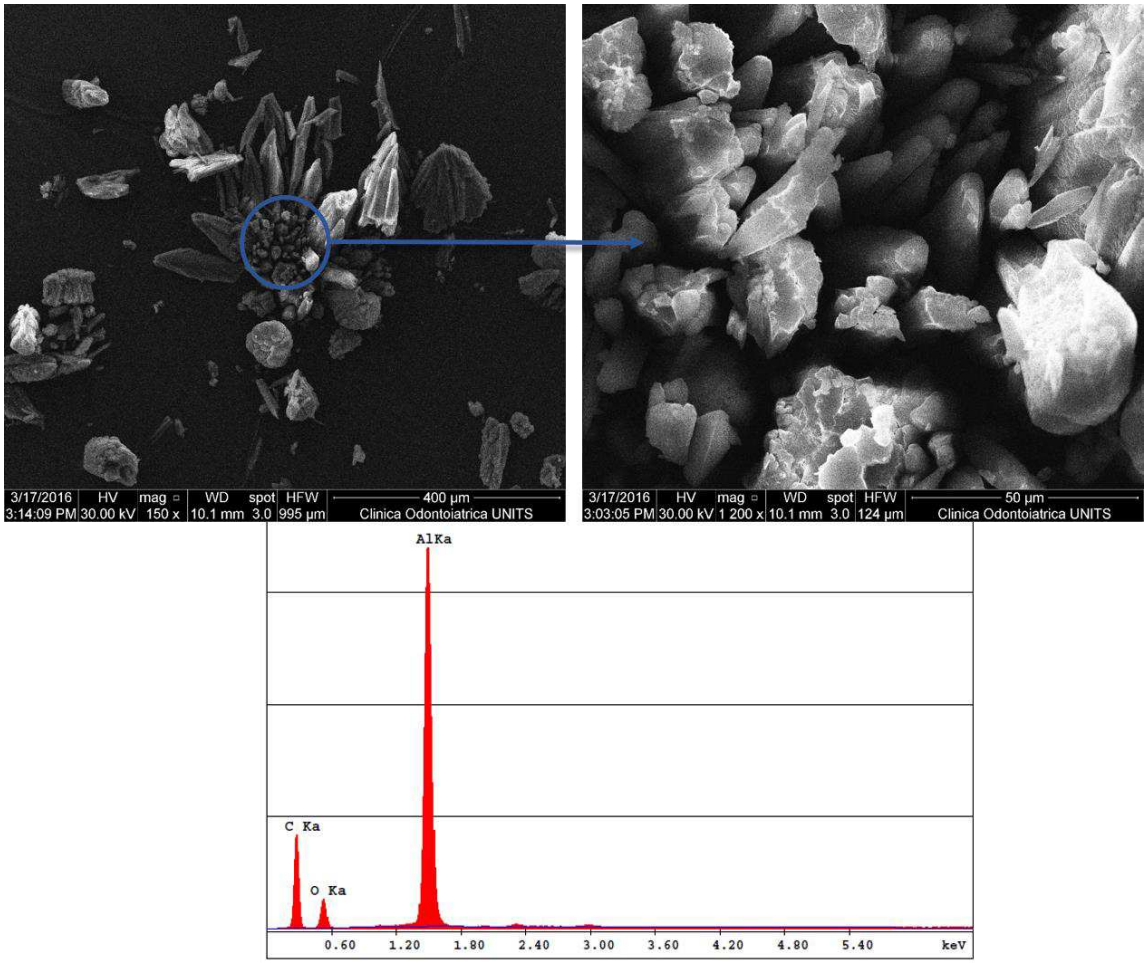

Figure 1.2.18 SEM images and EDS spectrum of particles found on carbon tabs placed on the machine performing metalisation in Factory 3. Scale bar: 400 µm (image on the left), 50 µm (image on the right). Spectrum refers to an aluminium-containing compound.

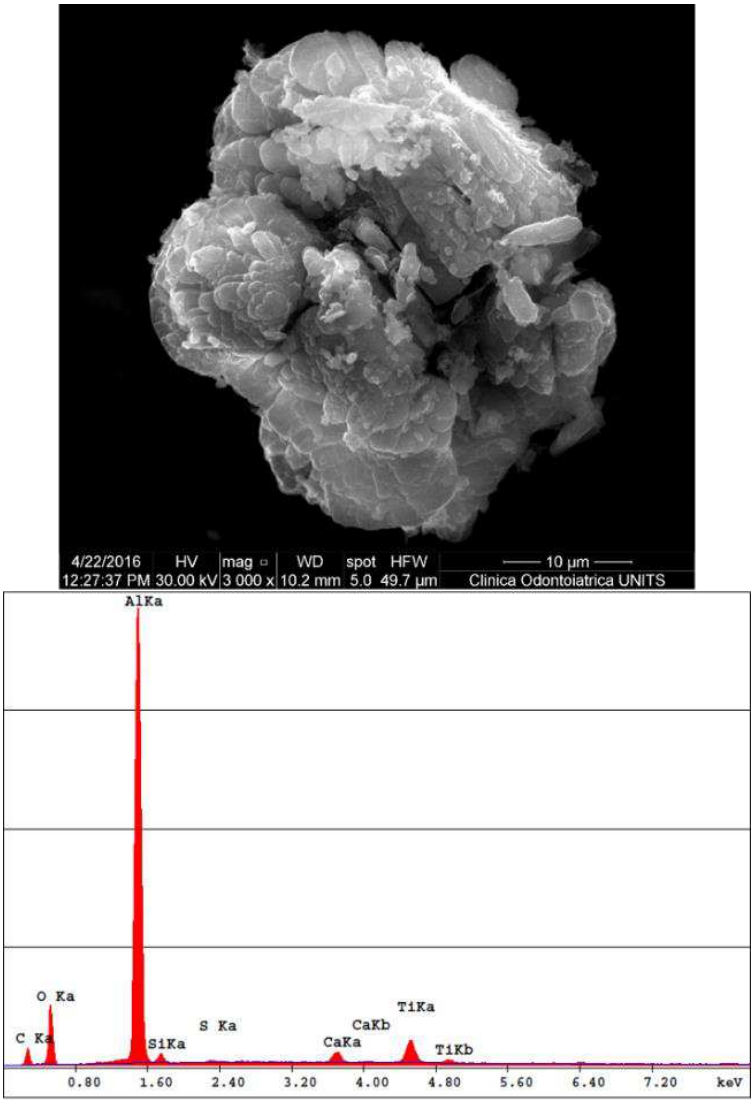

Figure 1.2.19 SEM image and EDS spectrum of an aggregate of particles found on carbon tabs placed on the machine performing metalisation in Factory 3. Scale bar: 10 µm. Spectrum refers to an aluminium-containing compound.

2.3.2.2 Wipe and tape samples

Table 1.2.8 summarises the results of the quantitative analysis of wipe and tape samples collected in each factory as mean values over non-consecutive sampling days. The results represent the contamination and refer to the quantity of Al deposited on the selected area: 100 cm^2 of working surfaces (wipe samples) and 3.80 cm^2 of skin (tape samples).

Table 1.2.8 Surface and skin contamination for each factory: total amount of Al (µg) on wipe (selected area: standardized 100 cm^2), and tape samples (selected area: disc area 3.80 cm^2). n= number of samples analysed by means of ICP-AES.

Contamination	Average exposure time (minutes)	µg Al on wipe/tape mean (SD)
Factory 1		
Surface contamination		
Wipe samples from welding positions, prior to cleaning procedures (n=4)	Days/weeks	418.0 (27.2)
Wipe samples from welding positions after cleaning (blank) (n=4)	0	69.6 (11.7)
Wipe samples from welding positions, after a full work shift (n=4)	480	78.4 (15.4)
Skin contamination		
Skin tape stripping from non-exposed volunteers (n=4)	0	1.257 (0.536)
Skin tape stripping from welders (n=9)	360	6.427 (1.314)
Factory 2		
Surface contamination		
Wipe samples from machines and control consoles after a full work shift (n=13)	450	104.8 (21.6)
Skin contamination		
Skin tape stripping from workers (n=7)	480	6.517 (2.145)
Factory 3		
Surface contamination		
Wipe samples from the machine performing metallization and various surfaces near it (n=9)	Hours/days	37,128 (1,223)
Skin contamination		
Skin tape stripping from workers (n=4)	165	7.391 (2.375)

2.4 Discussion

Background data obtained in Factory 1 and 3 are not shown here but, as aforementioned, an increase in number and a decrease in size of particles in the range 10-300 nm was registered moving from background areas to the emission source. This demonstrates that the specific manufacturing process involves the production of UFPs that are released in the working environment.

Fig. 1.2.20 shows the comparison of the median PNC and the average particle size between the three factories mediated along all sampling days at the emission source.

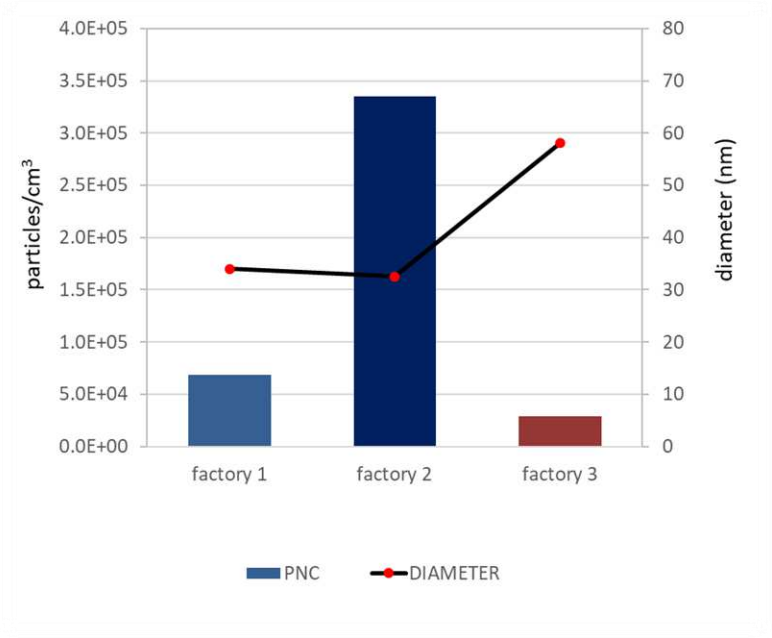

Figure 1.2.20 Comparison of the median PNC (bars) and the average particle size (dots) between the three factories mediated along all sampling days at the emission source.

The die casting production cycle performed in Factory 2 seems to be responsible for the highest emission of particles in the size range 10-300 nm with a mean diameter of 32 nm (UFPs).

The welding process performed in Factory 1 seems to release a lower amount of UFPs with a comparable mean size.

Graczyk and coworkers (2016) investigated UFPs emission during aluminium welding performed with a technique (GTAW) different from that used in Factory 1. They found that the mean diameter of particles in the size range 10-300 nm was 51 nm in a near field location (about 0.6 m away from the welding task) and 45 nm in the breathing zone of welders. These results are similar to those obtained in Factory 1 taking into account the differences in the experimental conditions.

They also found mean PNC between 1.10E+06 particles cm^{-3} in the near field location and 1.69E+06 particles cm^{-3} in the breathing zone of welders. Results obtained in Factory 1 are approximately one order of magnitude lower except for peak events. It should be said that PNC increases with the decrease of distance from the emission source so results obtained in Factory 1 are affected by the distance (2 m from the welding task). Reducing the distance results obtained in our study would be probably more similar to data reported in literature (Graczyk et al., 2016).

This difference can also be due to the different welding technique used and the raw materials. In these terms during welding of steel (Brouwer et al., 2004) peak number concentration was about 3E+5 particles cm^{-3} at a distance of 0.60 m from the welding task.

Lehnert and coworkers (2012) evaluated different kind of welding processes with different raw materials. Area sampling revealed a median count of 1E+5 particles cm^{-3} in

the particle size ranging from 14 to 673 nm comprising UFPs and their agglomerates. These results seem to be comparable to those obtained in Factory 1.

For what concern the die casting process performed in Factory 2 comparisons can be done with a study of Cheng and coworkers (2008). They measured the ultrafine particle concentrations and size distribution in an iron foundry where the operations performed were similar to those performed in Factory 2 (melting and pouring of raw metals). UFPs number concentrations ranged from 2.07E+4 to 2.82E+5 particles cm^{-3} (size range 10-100 nm) and the geometric mean diameter was found to be about 35 nm. These data seem to be substantially in agreement with those obtained in Factory 2.

The metalisation of polymeric film but, in particular, the cleaning process of the machine performing it (the dusty process we investigated) in Factory 3 seems to be responsible for the lowest emission of particles in the size range 10-300 nm with a mean diameter of 58 nm (UFPs).

IFA (Institute for Occupational Safety and Health) in Germany and DMSAE (Dutch Minister of Social Affairs and Employment) in The Netherlands (van Broekhuizen et al., 2011) proposed the nano reference value (NRV, 8h TLW= 4E+4 particles cm^{-3}). Considering this limit only Factory 3 can be considered safe in terms of UFPs exposure. Factory 1 showed mean values a little bit higher than the proposed reference value while Factory 2 cannot be considered safe in these terms.

The average aluminium concentration in respirable dust was far below the ACGIH limit (1 mg m^{-3}) in Factory 1 and 2 (1.833 and 4.367 μg m^{-3} respectively). Manufacturing processes performed in Factory 3, if compared to the other factories, seem to release a higher amount of respirable Al even if one order of magnitude lower than the ACGIH limit.

British Standard Institute (BSI) proposes for insoluble nanomaterials a workplace limit value of 0.066 times the workplace limit value for microscale material. In our case this limit corresponds to 66 μg m^{-3}. Given this consideration, the levels found in Factory 1 and 2 can be considered safe since UFPs are only a fraction of the respirable dust that was sampled.

On the contrary Factory 3 seems to exceed this limit with a mean value of 73.23 μg m^{-3} but the processes performed are responsible for the lowest emission of UFPs. Moreover, Al concentration ranging from 1.970 to 5.757 μg m^{-3} was measured on the after filter (particle fraction <250 nm) of the cascade impactor used in parallel to the respirable dust samplers. Given this consideration, also Factory 3 can be considered safe.

The prevalence of micro respect to ultrafine particles in Factory 3 are supported by TEM and SEM data. As a matter of fact, on TEM grids collected in Factory 3, aggregates in the size range 1-5 μm were found. Beside this kind of micro particles, nanoscale particles were sporadically observed.

On carbon tabs submicron particles were also sporadically observed while bigger aggregates (10 and 200 μm) were predominant.

On the contrary on TEM grids collected in Factory 1 and 2 aggregates of nanoparticles were found. Aggregates of quasi-spherical nanoparticles (90-100 nm) were observed on carbon tabs even if aggregates of higher dimensions were also observed. It is plausible that smaller particles dispersed in air tend to aggregate/agglomerate forming structures of higher dimensions and depositing on surfaces.

Tape stripping results showed that all workers had a higher amount of Al deposited on their skin if compared to non exposed volunteers. We cannot exclude that Al could be

contained in agglomerates of nanoparticles especially in the case of Factory 1 and 2 where agglomerates of nanoparticles were found on the working surfaces.

From wipe samples analysis we observed an increase of surface contamination during the work shift in all the factories. A standard cleaning of the surfaces is not always enough to free the surface from metals.

Together the findings on surfaces and skin contamination suggest that it is important to provide an adequate cleaning of the surfaces to minimise secondary exposure sources.

Our study demonstrated that welders and workers in the die casting sector are exposed to UFPs containing Al and that inhalation route could be the main portal of entry in the human body. Surface and skin contamination seems to be a secondary source of exposure to UFPs.

From these considerations it is important to take into account the toxicological effects of this kind of exposure in occupational contexts.

Andujar et al. (2014) have provided evidence of a link between human exposure to UFPs in welders and long-term pulmonary effects. In 2011 a review (Win-Shwe and Fujimaki, 2011) has pointed out that in experimental animals NPs may enter the brain by (i) nasal mucosa and olfactory nerve, (ii) systemic circulation. When inside the brain, NPs may induce inflammation, apoptosis and oxidative stress.

The exposure to welding fumes NPs is associated with an increase of inflammatory cytokines in bronchoalveolar lavage and systemic oxidative stress, with an evident ability of generating free radicals (Li et al., 2004). Significant pulmonary inflammatory responses and lipid peroxidation has been evidenced in rats exposed to welding fumes (McNeilly et al., 2005). The soluble metals appear to be the primary mechanism of oxidative stress, inflammation and carcinogenesis (Donaldson et al., 2005).

Toxicity studies evidenced greater toxicity of nano alumina compared to micro particles (Zhang et al., 2013), induction of depression like behaviour especially on female mice (Zhang et al., 2015), deposition of Al in the brain, olfactory bulb (Kwon et al., 2013) and other organs in mice (Morsy et al., 2016) acute cytotoxic effects on mesenchymal cells (Periasamy et al., 2015), oxidative stress in the brain, kidneys and liver of rats and interaction with several enzymatic activities (Prabhakar et al., 2012), genetic damages to the bone marrow of rats (Balasubramanyam et al., 2016).

2.5 Conclusions

In the tested occupational settings, a significant increase in number and a decrease in size of particles in the range 10-300 nm was registered moving from background areas to the emission source demonstrating that the specific manufacturing process is responsible for the production of UFPs that are released in the working environment.

The die casting production cycle seems to be responsible for the highest emission of particles in the size range 10-300 nm followed by the welding activities. Both this manufacturing processes cannot be considered safe taking into account the nano reference value (4E+4 particles cm^{-3}) suggesting a possible increased risk of inhalation exposure in workers. On the contrary they can be considered safe in terms of Al concentration in the UFPs fraction using the data obtained from sampling of respirable dust as a comparison.

The presence of UFPs containing Al in occupational settings where welding and die casting activities were performed are supported by TEM-EDS data for airborne particles and SEM-EDS data for particles deposited mainly on working surfaces. In the second case a tendency to the aggregation were observed leading us to conclude that the

inhalation route could be the main portal of entry in the human body. Surface and skin contamination seems to be a secondary source of exposure to UFPs.

The metalisation of polymeric films but, in particular, the cleaning process of the machine performing it (the dusty process we investigated) seems to be responsible for the lowest emission of particles in the size range 10-300 nm but the highest release of respirable Al. This result is confirmed by TEM and SEM analysis of airborne and deposited particles that revealed the presence of particles mainly in the non-nano range. Giving these considerations, this manufacturing process can be considered safe taking into account both the nano reference value and Al concentration in the UFPs fraction using the data obtained from the cascade impactor.

The exposure of workers to contaminants in working environments is conventionally assessed using the American Conference of Governmental Industrial Hygienists (ACGIH) limit values as reference without taking into account the exposure to UFPs despite their toxicological relevance. In the tested factories ACGIH limits were respected but an integrated approach which takes into account air sampling, and the evaluation of skin and surfaces contamination should be recommended to assess the exposure to UFPs when no standardised methods exist.

References

American Society for Testing Materials (ASTM) International. (2008). *D 6966-08 Standard practice for collection of settled dust samples using wipe sampling methods for subsequent determination of metals*.

Andujar, P., Simon-Deckers, A., Galateau-Sallé, F., Fayard, B., et al. (2014). Role of metal oxide nanoparticles in histopathological changes observed in the lung of welders. *Part. Fibre Toxicol.* 11: 23-35.

Antonini, J. M. (2003). Health effects of welding. *Crit. Rev. Toxicol.* 33: 61-103.

Azarmi, F., Kumar, P. and Mulheron, M. (2014). The exposure to coarse, fine and ultrafine particle emissions from concrete mixing, drilling and cutting activities. *J. Hazard. Mat*. 279: 268–279.

Balasubramanyam, A., Sailaja, N., Mahboob, M., Rahman, M. F., et al. (2016). Evaluation of genotoxic effects of oral exposure to aluminium oxide nanomaterials in rat bone marrow. *Mut. Res*. 676: 51-59.

Bang, J. J., Trillo, E. A. and Murr, L. E. (2003). Utilization of selected area electron diffraction patterns for characterization of air submicron particulate matter collected by a thermophoretic precipitator. *J. Air Waste Manage. Assoc.* 53: 227-236.

Berlinger, B., Benker, N., Weinbruch, S., et al. (2011). Physicochemical characterization of different welding aerosols. *Anal Bioanal Chem*. 399: 1773–1780.

Berlinger, B., Ellingsen, D. G., Náray, M., et al. (2008). A study of the bio-accessibility of welding fumes. *J. Environ. Monit.* 10: 1448–1453.

Birch, M. E., Ku, K., Evans, D. E. and Ruda-Eberenz, T. A. (2011). Exposure and Emission Monitoring during Carbon Nanofiber Production – Part I: Elemental Carbon and Iron-Soot Aerosols. *Ann. Occup. Hyg*. 55(9): 1016-1036.

Brand, P., Lenz, K., Reisgen, U., et al. (2013). Number size distribution of fine and ultrafine fume particles from various welding processes. *Ann. Occup. Hyg*. 57: 305–313.

Brody, A. R., Roe, M. W., Evans, J. N. and Davis, G. S. (1982). Deposition and translocation of inhaled silica in rats: quantification of particle distribution, macrophage participation, and function. *Lab. Invest*. 47: 533-542.

Brouwer, D. H., Gijsbers, J. H. J. and Lurvink, M. W. M. (2004). Personal Exposure to Ultrafine Particles in the Workplace: Exploring Sampling Techniques and Strategies. *Ann. Occup. Hyg*. 48(5): 439–453.

BSI. (2007). *Nanotechnologies-Part 1: Good Practice Guide for Specifying Manufactured Nanomaterials.* London, UK British Standards Institute. PD 6699-1.

Buonanno, G., Morawska, L. and Stabile, L. (2011). Exposure to welding particles in automotive plants. *J. Aerosol Sci*. 42: 295-304.

CEN. European Committee for Standardization. (1993). *Workplace atmospheres: size fraction definitions for measurement of airborne particles* (Report No. BS EN 481:1993). London, England: CEN, British Standards Institute.

Cheng, Y. H., Chao, Y. C., Wu, C. H., Tsai, C. J., et al. (2008). Measurements of ultrafine particle concentrations and size distribution in an iron foundry. *J. Hazard. Mater*. 158(1): 124-30.

Dasch, J. and D'Arcy, J. (2008). Physical and chemical characterization of airborne particles from welding operations in automotive plants. *J. Occup. Environ. Hyg*. 5: 444–454.

Donaldson, K., Tran, L., Jimenez, L. A., Duffin, R., et al. (2005). Combustion-derived nanoparticles: a review of their toxicology following inhalation exposure. *Part. Fibre. Toxicol.* 21: 2-10.

Fornero, E., Belluso, E., Capella, S. and Bellis, D. (2009). Environmental exposure to asbestos and other inorganic fibres using animal lung model. *Sci. Tot. Env*. 407(3): 1010–1018.

Giorgianni, C. M., D'Arrigo, G., Brecciaroli, M., Abbate, A., et al. (2014). Neurocognitive effects in welders exposed to aluminium. *Toxicol. Ind. Health.* 30: 347-356.

Graczyk, H., Lewinski, N., Zhao, J., Concha-Lozano, N., et al. (2016). Characterization of Tungsten Inert Gas (TIG) Welding Fume Generated by Apprentice Welders. *Ann. Occup. Hyg*. 60(2): 205-219.

Hedmer, M., Ludvigsson, L., Isaxon, C., Nilsson, P. T., et al. (2015). Detection of Multi-walled Carbon Nanotubes and Carbon Nanodiscs on Workplace Surfaces at a Small-Scale Producer. *Ann. Occup. Hyg*. 59(7): 836-852.

IFA (2016). *Criteria for assessment of the effectiveness of protective measures*.

Jenkins, N. T. and Eagar, T. W. (2005b). Chemical analysis of welding fume particles. *Weld. J*. 84: 87s-93s.

Jenkins, N.T. (2003). Chemistry of airborne particles from metallurgical processing. Ph.D. thesis, Massachusetts Institute of Technology, pp.189.

Jenkins, N. T., Pierce, W. M. and Eagar, T. W. (2005a). Particle size distribution of gas metal and flux cored arc welding fumes. *Weld. J.* 84: 156–163.

Kiesswetter, E., Schaper, M., Buchta, M., Schaller, K. H., et al. (2007). Longitudinal study on potential neurotoxic effects of aluminium: I. Assessment of exposure and neurobehavioural performance of Al welders in the train and truck construction industry over 4 years. *Int. Arch. Occup. Environ. Health*. 81: 41-67.

Kiesswetter, E., Schaper, M., Buchta, M., Schaller, K. H., et al. (2009). Longitudinal study on potential neurotoxic effects of aluminium: II. Assessment of exposure and

neurobehavioral performance of Al welders in the automobile industry over 4 years. *Int. Arch. Occup. Environ. Health.* 82: 1191–1210.

Konarski, P., Iwanejko, I. and Ćwil, M. (2003a). Core-shell morphology of welding fume micro- and nanoparticles. *Vac*. 70: 385–389.

Konarski, P., Iwanejko, I. and Mierzejewska, A. (2003b). SIMS depth profiling of working environment nanoparticles. *Appl. Surf. Sci.* 203-204: 757–761.

Kou, S. (2003). *Welding metallurgy. 2nd edn,* Wiley & Sons Inc, London.

Kwon, J. T., Seo, G. B., Jo, E., Lee, M., Kim, H. M., et al. (2013). Aluminum Nanoparticles Induce ERK and p38MAPK Activation in Rat Brain. *Toxicol. Res.* 29(3): 181-185.

Lademann, J., Jacobi, U., Surber, C., Weigmann, H. J., et al. (2009). The tape stripping procedure – evaluation of some critical parameters. *Eur. J. Pharm. Biopharm*. 72(2): 317-23.

Lee, S. J., Demokritou, P., Koutrakis, P. and Delgado-Saborit, J. M. (2006). Development and evaluation of personal respirable particulate sampler (PRPS). *Atmos. Environ*. 40(2): 212-224.

Lehnert, M., Pesch, B., Lotz, A., Pelzer, J., et al. (2012). Exposure to inhalable, respirable, and ultrafine particles in welding fumes. *Ann. Occup. Hyg.* 56: 557-567.

Li, G. J., Zhang, L. L., Lu, L., Wu, P., et al. (2004). Occupational exposure to welding fume among welders: alteration of manganese, iron, zinc, copper, and lead in body fluids and the oxidative stress status. *J. Occup. Environ. Med.* 46: 241-248.

McMillan, G. (2005). Is electric arc welding linked to manganism or Parkinson's disease? *Toxicol. Rev.* 24(4): 237-257.

McNeilly, J. D., Heal, M. R., Beverland, I. J., Howe, A., et al. (2004). Soluble transition metals cause the pro-inflammatory effects of welding fumes in vitro. *Toxicol. Appl. Pharmacol.* 196: 95–107.

McNeilly, J. D., Jiménez, L. A., Clay, M. F., MacNee, W., et al. (2005). Soluble transition metals in welding fumes cause inflammation via activation of NF-B and AP-I. *Toxicol. Lett*. 158(2): 152-157.

Merkus, H. G. (2009). *Particle size measurements: fundamentals, practice, quality*, Springer.

Miettinen, M., Torvela, T., Leskinen, J. T. (2016). Physicochemical Characterization of Aerosol Generated in the Gas Tungsten Arc Welding of Stainless Steel. *Ann. Occup. Hyg*. 60(8): 960-968.

Miller, A., Frey, G., King, G. and Sunderman, C. (2010). A handheld electrostatic precipitator for sampling airborne particles and nanoparticles. *Aerosol Sci. Technol*. 44: 417–427.

Moroni, B. and Viti, C. (2009). Grain size, chemistry, and structure of fine and ultrafine particles in stainless steel welding fumes. *Aerosol Sci.* 40: 938 – 949.

Morsy, G., El-Ala, K. And Ali, A. (2016). Studies on fate and toxicity of nanoalumina in male albino rats: Lethality, bioaccumulation and genotoxicity. *Toxicol. Ind. Health*. 32(2): 344-359.

Oberdörster, G., Oberdörster, E. and Oberdörster, J. (2005). Nanotoxicology: an emerging discipline evolving from studies of ultrafine particles. *Environ. Health Perspect*. 113(7): 823-839.

Periasamy, V., Athinarayanan, J. and Alshatwi, A. (2015). Aluminum oxide nanoparticles alter cell cycle progression through CCND1 and EGR1 gene expression in human mesenchymal stem cells. *Biotech. Appl. Biochem.* 63(3): 320-327.

Prabhakar, P. V., Reddy, U. A., Singh, S. P., Balasubramanyam, A., et al. (2012). Oxidative stress induced by aluminium oxide nanomaterials after acute oral treatment in Wistar rats. *J. Appl. Toxicol.* 32: 436-445.

Prodi, A. and Larese Filon, F. (2016). Nano-Scaled Particles and Fibres Occupational Exposure Assessment: An Integrated Approach from Air Sampling to Skin and Surface Contamination. *Nano Biomed. Eng*. 8(2): 91-104.

Racette, B. A., McGee-Minnich, L., Moerlein, S. M., Mink, J. W., et al. (2001). Welding-related parkinsonism. Clinical features, treatment, and pathophysiology. *Neurol*. 56: 8–13.

Richman, J. D., Livi, K. J. T. and Geyh, A. S. (2011). A scanning transmission electron microscopy method for determination of manganese composition in welding fume as a function of primary particle size. *J. Aerosol Sci*. 42: 408-418.

Riihimäki, V., Valkonen, S., Engström, B., Tossavainen, A., et al. (2008). Behavior of aluminum in aluminum welders and manufacturers of aluminum sulfate--impact on biological monitoring. *Scand. J. Work. Environ. Health*. 34(6): 451-62.

Shepard M., and Brenner, S. (2014). Cutaneous exposure scenarios for engineered nanoparticles used in semiconductor fabrication: a preliminary investigation of workplace surface contamination. *Int. J. Occup. Environ. Health*. 20(3): 247-257.

Sowards, J. W., Lippold, J. C., Dickinson, D. W. and Ramirez, A. J. (2008b). Characterization of welding fume from SMAW electrodes – Part I. *Weld. J*. 87: 106–112.

Sowards, J. W., Ramirez, A. J., Dickinson, D. W. and Lippold, J. C. (2010). Characterization of welding fume from SMAW electrodes – Part II. *Weld. J*. 89: 82–90.

Sowards, J. W., Ramirez, A. J., Lippold, J. C. and Dickinson, D. W. (2008a). Characterization procedure for the analysis of arc welding fume. *Weld. J*. 87: 76–83.

van Broekhuizen, P., van Broekhuizen, F., Cornelissen, R. and Reijnders, L. (2011). Use of nanomaterials in the European construction industry and some occupational health aspects thereof. *J. Nanopart. Res.* 13: 447-462.

Wake, D., Mark, D. and Northage, C. (2002) Ultrafine aerosols in the workplace. *Ann. Occup. Hyg*. 46(1): 235-238.

Willwhite, C., Karyakina, N., Yokel, R., Yenugadhati, N., et al. (2014). Systematic review of potential health risks posed by pharmaceutical, occupational and consumer exposures to metallic and nanoscale aluminum, aluminum oxides, aluminum hydroxide and its soluble salts. *Crit. Rev. Toxicol.* 44(4); 1-80.

Win-Shwe, T. and Fujimaki, H. (2011). Nanoparticles and neurotoxicity. *Int. J. Mol. Sci.* 12(9): 6267-6280.

Yu, I. J., Kim, K. J., Chang, H. K., Song, K. S., et al. (2000). Pattern of deposition of stainless steel welding fume particles inhaled into the respiratory systems of Sprague-Dawley rats exposed to a novel welding fume generating system. *Toxicol. Lett*. 116(1-2): 103-111.

Zhang, Q., Xu, L., Wang, J., Sabbioni, E. et al. (2013). Lysosomes involved in the cellular toxicity of nano-alumina: combined effects of particle size and chemical composition. *J. Biol. Regul. Homeost. Agents.* 27(2):365-375.

Zhang, X., Xu, Y., Zhou, L., Zhang, C., et al. (2015). Sex-Dependent Depression-Like Behavior Induced by Respiratory Administration of Aluminum Oxide Nanoparticles. *Int. J. Environ. Res. Public Health*. 12(12): 15692-15705.

Zimmer, A. T. and Biswas, P. (2001). Characterization of the aerosols resulting from arc welding processes. *J. Aerosol Sci*. 32: 993–1008.

Zimmer, A. T. and Maynard, A. D. (2002). Investigation of the aerosols produced by a high-speed hand-held grinder using various substrates. *Ann. Occup. Hyg*. 46: 663–672.

Zimmer, A. T., Baron, P. A. and Biswas, P. (2002). The influence of operating parameters on number-weighted aerosol size distribution generated from a gas metal arc welding process. *J. Aerosol Sci*. 33: 519–531.

SECTION 2

Real-time measurements, sampling and characterisation of ultrafine and submicron airborne particles in proximity of an integrated steel plant

In Section 1 the attention was addressed to ultrafine and submicron particles released by industrial processes in working environments. Nevertheless, industrial activities are also an important source of metal-containing UFPs that are released in ambient air.

Iron and steel industries can generate large amounts of coarse to ultrafine range particles associated with high concentration of metals such as Cr, Fe, Mn, Ni and Zn (Mohiuddin et al., 2014).

Iron is an essential element for the human body but not in the form of inhalable particles. As a matter of fact, iron-reach particles can stimulate the production of ROS that are a major contributing factor in inflammation and toxicity (Gwinn and Vallyathan, 2006).

Particles released by this kind of industrial activities can impact the surrounding areas. If the area is inhabited the residents can be exposed to elevated levels of atmospheric particles of a wide dimensional range and metal composition.

In Trieste, in Servola district, an integral cycle steel plant commonly called “Ferriera” is present. The dwellings of the district are positioned in very close proximity of the plant that is considered a “hot spot”.

Given these considerations, this section focuses on the evaluation of the presence of airborne ultrafine and submicron particles in a sampling site in Servola district.

Real-time measurements of number concentration and mean diameter of particles in the range 10-300 nm were performed. Moreover size-resolved sampling of particles was used to allow qualitative (ED-μXRF), quantitative (ICP-AES) and morpho-chemical (TEM-EDS) analysis. Data from a "background" site where UFPs emission from anthropogenic sources was expected to be minimum were used for a comparison.

Instruments used for real-time measurements and size-resolved sampling of particles were the same portable devices used in working environments for the studies presented in Section 1.

The aim of this study was a first approach to a topic of major concern and some improvements in the sampling strategy should be introduced in future studies.

The "Commissariato del Governo nella Regione Friuli Venezia Giulia" ("Fondo Trieste") funded this doctoral research that should provide a significant impact on the area of Trieste.

1. Introduction

Atmospheric particles are currently regulated in terms of mass concentrations in the size ranges PM_{10} and $PM_{2.5}$. Since there are no air quality regulations for UFPs, they have not received due attention from regulatory authorities (Kumar et al., 2011).

UFPs are ubiquitous and in the last decade have become a major human health concern. Clinical and toxicological studies have shown that this class of particles in part act through mechanisms that are not shared with larger particles that dominate mass-based metrics such as $PM_{2.5}$ and PM_{10} (WHO, 2013). UFPs differ from larger sized particles in their potential for lung deposition and translocation to other parts of the body. Moreover, they have a higher surface area per unit volume than larger particles that increases the capability to adsorb organic compounds, some of which are potentially carcinogenic (Donaldson et al., 2005), and the potential to act as catalyst for specific reactions with cells (Oberdörster, 2001).

On the other hand it has been demonstrated that UFPs have a higher probability of suspension in the atmosphere and hence a longer residence time (AQEG, 2005), influencing urban visibility (Horvath, 1994), global climate (Strawa et al., 2010), and the chemistry of the atmosphere opening novel chemical transformation pathways (Kulmala et al., 2004).

As UFPs have a negligible mass if compared with larger sized particles, what would be the best metric to be measured is still under debate. UFPs are preferentially evaluated through measurements of particle number concentration (PNC) (Kumar et al., 2010).

While UFPs account for < 1% of outdoor mass concentration of total particulate matter (PM), they account for about 90% of the PM number concentration (Oberdörster, 2001).

1.1 Formation and growth of UFPs

In aerosol science, atmospheric particles are discussed in terms of modes (i.e. nucleation, Aitken, accumulation and coarse) (Fig. 2.1). Distinctive sources, size range, formation mechanisms, chemical composition and deposition pathways (Hinds, 1999) correspond to each mode.

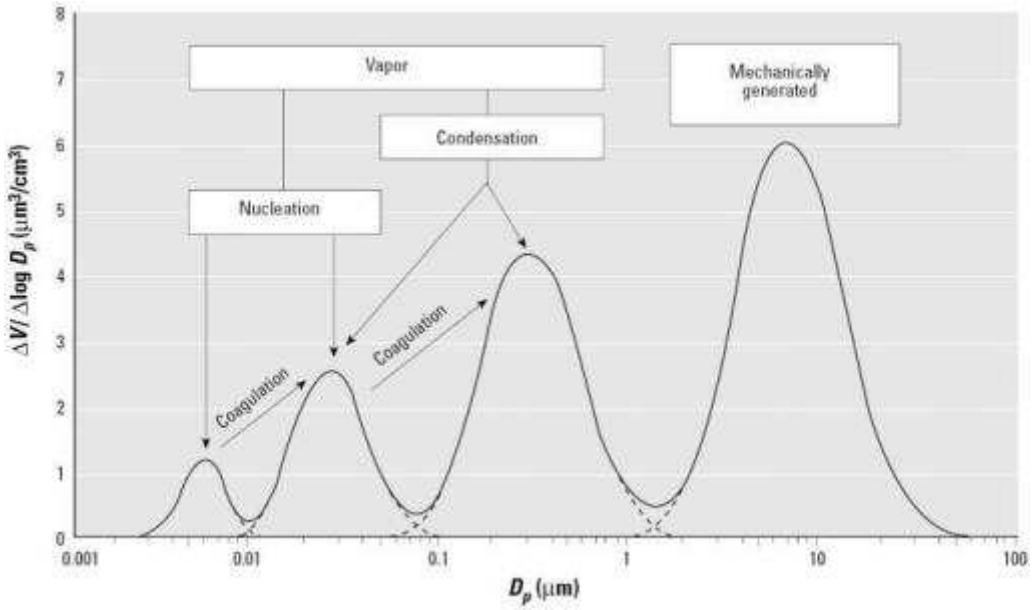

Figure 2.1 Idealised size distribution of particulate matter (Oberdörster, 2005).

Nucleation, Aitken, and in some cases also accumulation, mode particles are defined as UFPs (Kumar et al., 2010).

Nucleation (or nuclei) mode particles are typically defined as the 1-30 nm range. They are thought to be formed through nucleation (gas-to-particle conversion) in the

atmosphere after rapid cooling and dilution of emissions. These particles are typically liquid droplets primarily composed by readily volatile components derived from unburned fuel and lubricant oil. Nucleation mode particles are found in high number concentrations near sources. They are characterised by relatively short atmospheric life time due to collisions with each other and with particles in the accumulation mode. Other removal mechanisms are dry deposition, rainout or growth through condensation (Hinds, 1999).

The Aitken mode particles, typically defined as the 20-100 nm range, is an overlapping fraction of the nucleation and accumulation mode. Particles in this mode arise from the growth or coagulation of nucleation mode particles as well as by production by primary combustion sources such as vehicles (Kulmala et al., 2004). These particles are mainly composed of a soot/ash core with a readily absorbed outer layer of volatilisable material (Lingard et al., 2006).

Accumulation mode particles, typically defined as the 30-300 nm size range, are carbonaceous (soot and/or ash) agglomerates. They derive mainly from the combustion of engine fuel and lubricant oil by diesel-fuelled or direct injection petrol-fuelled vehicles (Graskow et al., 1998; Wehner et al., 2009), as well as from the coagulation of nucleation mode particles (Hinds, 1999). They tend to have relatively long atmospheric life times, from days to weeks, and hence can travel over very long distances in the atmosphere.

1.2 Sources of UFPs

1.2.1 Natural sources

The main natural sources of UFPs are forests, oceans and atmospheric formation. It has been demonstrated that PNC in marine and forest environments is typically 2-3 orders of magnitude smaller than in urban areas. New particles are formed in the atmosphere through condensation of semi-volatile organic aerosols, photochemically induced nucleation and/or nucleation through gas-to particle conversion (Kumar et al., 2010). Episodic contributions to the PNC derives from forest fires, dust storms and volcanic eruptions. The great variability in particle formation and growth rates in different environments leads to significant differences in number concentrations.

1.2.2 Anthropogenic UFPs

Manufactured NPs such as fullerenes, carbon nanotubes, metal oxides (e.g. oxides of iron and zinc, titania, ceria) and metal NPs (e.g. nano-silver) are not intentionally released into the environment, though a release may occur in the production, use and disposal phases.

Numerous studies demonstrate that road conventional-fuelled vehicles are a major source of UFPs in urban areas (Johansson et al., 2007; Keogh et al., 2009; Shi et al., 2001) contributing up to 86% of total PNC (Pey et al., 2009). As a matter of fact, the majority of particles emitted from road diesel- and petrol-fuelled vehicles are of sizes below 130 nm and 60 nm, respectively (Harris and Maricq, 2001; Kittelson, 1998). A number of studies described in detail in Kumar et al. (2010), suggest that use of bio-fuels in road vehicles considerably reduces emissions of total particle mass while this does not seem

to be the case with number concentrations. Another source of UFPs in cities are represented by tyre and road surface interactions (Gustafsson et al., 2008; Dahl et al., 2006).

1.2.2.1 Atmospheric metallic UFPs

Emissions from road vehicles are the primary source of metallic UFPs into the atmosphere (Sanderson et al., 2014). These can include derivatives of internal combustion engines, lubricating oils, fuel additives and trace amounts in gasoline and diesel fuel, particles from brake wear, and from resuspended tyre dust.

Evidence for metals in UFPs emissions from biomass burning and wood fuels has been reported in literature but it is difficult to define tracer elements because they strongly depend on the fuel type and combustion conditions.

Industrial processes such as metal refining and fossil fuel combustion are known to release fine particles which are often enriched in trace metals that can be considered conservative tracers of urban and industrial sources (Mbengue et al., 2014). This subject is discussed in length in reviews about UFPs (Sanderson et al., 2014; Riffault et al., 2015) (see Fig. 2.2).

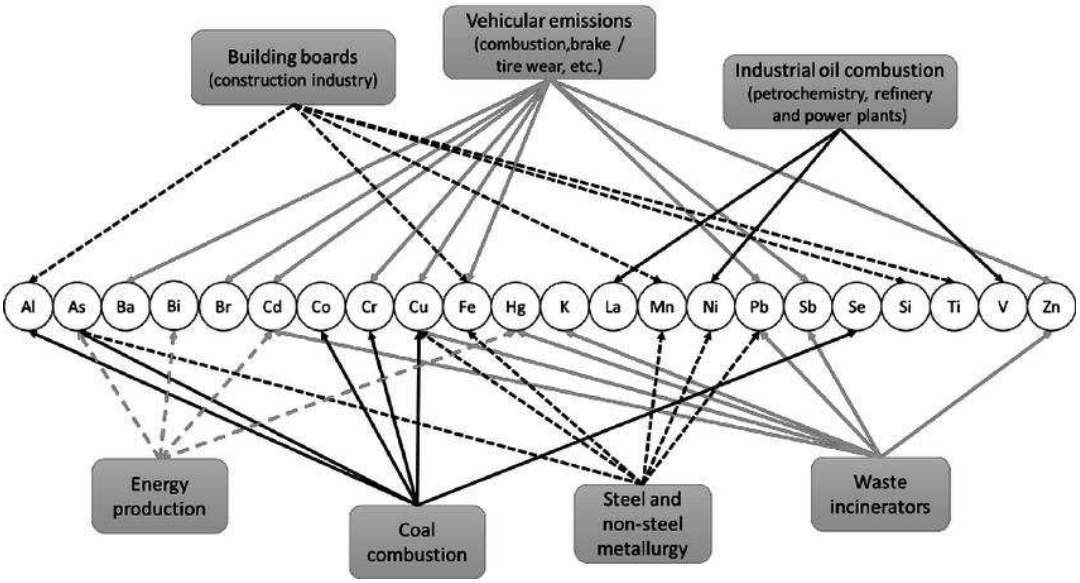

Figure 2.2 Main anthropogenic sources of metals in atmospheric particles (Riffault et al., 2015).

For instance, waste incinerators are known to be a source of trace metals in atmospheric particulates such as Cd, Pb, Sb and Zn (Tolocka e al., 2005). Cernuschi and coworkers (2012) reported that the main metals in UFPs emissions of waste to energy plants were Cr, Fe, Ni, Pb and Zn. Traces of Ti, V, Mn and Co were also found. Elements with higher boiling points presented higher concentrations at lower diameters (50-200nm) when emitted from the stack of a waste combustion plant (Buonanno et al., 2011). Other examples of metals that enrich UFPs of industrial origin are As, Cu, Fe, Mn, Pb for steelworks and non-ferrous metallurgy; Cr for coal combustion; Ni and V for fuel and oil combustion; and Sb, Cu and Ba for road traffic. Dall'Osto and coworkers (2008) has investigated particulate emissions from an integrated iron and steelmaking site. Metals dominating the spectra included Fe, Pb, Zn, Ni, and K were attributed to the iron-making, steel/coke-making, and the rolling mill processes of the facility.

1.3 Measurement methods

1.3.1 Counting and sampling techniques

As previously said particle number concentration of UFPs is the most considered parameter. In addition mass concentration, size distribution and chemical composition have to be taken into account for an extensive study.

Scanning mobility particle sizer (SMPS™, TSI Inc.) uses an electrical mobility detection technique to measure number and size distributions (Kumar et al., 2010). It consists of three components: (i) a bipolar radioactive charger for charging the particles, (ii) a differential mobility analyser (DMA) for classifying particles by electrical mobility, and (iii) a condensation particle counter (CPC) for detecting particles. The SMPS measures the electrical mobility equivalent diameter (Dp) in a size range that is specific of the model using a specific number of size channels for number concentrations in the range 10^2 -10^8 particles cm^{-3}. For SMPS measurements, mass concentration can be determined using assumptions of particle density and shape.

Multistage impactors are capable to segregate particles by passing the aerosol through a number of stages (one stage consisting of a nozzle and impaction plate) in series, with each subsequent stage collecting particles smaller than the one before it. This is known as a cascade impactor.

The electrical low pressure impactor (ELPI™, Dekati Ltd.) measures number, mass and size distributions of particles typically in the range 0.03-10 μm. It operates on three main principles: (i) charging by a corona charger, (ii) inertial classification using a low pressure cascade impactor, and (iii) electrical detection of the aerosol particles by a multi-channel electrometer (ELPI, 2017).

The micro orifice uniform deposit impactor (MOUDI, MSP corp.) consists of two basic assemblies: the cascade impactor and the rotator. The uniform deposit is achieved by using multiple nozzles at each stage and rotating the impaction plate beneath the nozzles (Marple et al., 1991).

Both the impactors allow particle collection for offline analyses (gravimetric, chemical and morphological) that are classically performed using filter substrates on impaction stages, the nature of which depends on the analytical technique that must be used and the species targeted (Riffault et al., 2015). There are different types of substrates that have specific physical and chemical characteristics, including Al foils, quartz fibre filters, PTFE, cellulose esters or polycarbonate membrane filters (Sanderson et al., 2014).

1.3.2 Offline methods

Depending on the information that has to be obtained various offline methods can be used.

Scanning electron microscopy (SEM) and transmission electron microscopy (TEM) are generally employed to investigate size and shape of atmospheric particles. While SEM analysis can be performed on different types of substrates just coating them with a conductive material, for TEM analysis the dissolution of filters is required in order to deposit a liquid drop on TEM grid (Moroni and Viti, 2009). Alternatively, the collection of particles directly on TEM grids positioned on the impaction plates of the impactor is possible (Kero et al., 2015). If SEM and TEM are coupled with an energy-dispersive X-ray analytical system (EDS), the elemental composition of particles can be determined and correlated to morphological data.

Trace elements are typically measured using destructive techniques such as graphite furnace atomic absorption spectroscopy (GF-AAS) (Manoli et al., 2002), inductively coupled plasma atomic emission spectroscopy (ICP-AES) (Fernandez-Espinosa et al., 2001) and inductively coupled plasma mass spectrometry (ICP-MS) if it is necessary to deal with low detection limits (Cernuschi et al., 2012; Fernandez-Camacho et al., 2012). All these analytical techniques require a sample pre-treatment that consists in the acid digestion of the filters.

In contrast, among non-destructive techniques that allow measurement of the elemental species directly on the filters, energy dispersive x-ray fluorescence spectroscopy (ED-XRF) (Vecchi et al., 2008; Bernardoni et al., 2011) can be cited.

1.3.3 Limitations

For what concern instruments that measure number and size distributions of particles such as mobility analysers, reproducibility of data still remains a major issue (Asbach et al., 2009). Other technical issues concern the definition of particle diameter (aerodynamic equivalent, Da, or electrical mobility equivalent, Dp), the appropriate sampling frequencies and the adequacy of corrections for particle losses in sampling tubes (Kumar et al., 2010). Instruments measuring particles based on Dp may be preferable to those measuring Da as the aerodynamic measure can be adversely affected by particle characteristics (such as size, shape and density), as most of the particles in the accumulation mode are non-spherical agglomerates (Hinds, 1999).

Cascade impactors instruments can require long sampling times to collect sufficiently high masses of UFPs for accurate quantification of mass and chemical composition that

depend on the limits of detection of the analytical technique (Sanderson et al., 2014). In literature sampling times of several days are typical. Moreover, particle bouncing can be a significant artifact in the measurements (Riffault et al., 2015), as well as interstage particle losses and deposition onto impaction walls. Some studies use coatings on the impaction stages to reduce these effects, but it represents a problem if chemical and gravimetric analysis have to be performed (Sanderson et al., 2014).

All these matters together with the lack of standards methods, instrumentations, long-term monitoring studies, limited the development of ambient UFPs regulations in terms of number concentrations, size distribution and elemental concentrations (Kumar et al., 2010).

2. Materials and methods

2.1 Sites description

Trieste is a city located in NE Italy by the Adriatic Sea counting about 200,000 inhabitants.

In this work four sampling sites where UFPs emission from anthropogenic sources was expected to be minimum were selected in a light traffic zone near the University of Trieste and in the Karst Plateau (see Fig. 2.3, Table 2.1).

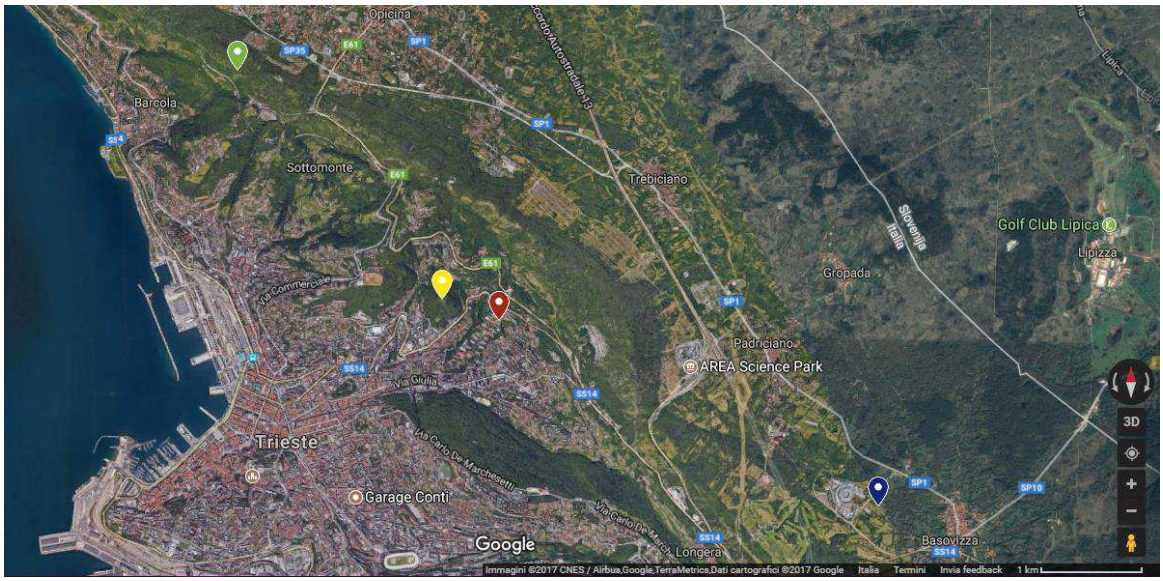

Figure 2.3 "Background" sites in Triste. Blue: site 1, red: site 2, yellow: site 3 and green: site 4.

In Servola district (about 12,000 inhabitants- density 8,300 inh km^{-2}) an integral cycle steel plant commonly called "Ferriera" is present. The dwellings of the district are positioned in a very close proximity to the plant. The steel plant overlooks the sea to the west and the inland to the east. One site (named "Servola") positioned in a light traffic street between two buildings of a neighbourhood (see Fig. 2.4, Table 2.2) was selected.

The site was separated from the coke oven batteries of the plant by about 200 m where just covered tennis courts and a railway delimiting the steel plant were present.

Figure 2.4 Map of the integral steel plant "Ferriera" (blue area) and Servola district (red area). The red point indicates the position of "Servola" sampling site.

2.2 Chemicals

All chemicals were analytical grade. Nitric acid (≥ 69% w/w) and hydrochloric acid (≥ 37% w/w) were purchased from Sigma Aldrich (Milan, Italy). Water reagent grade was produced with a Millipore purification pack system (MilliQ water).

2.3 Counting, sampling and characterisation of particles

2.3.1 Real-time measurements

A miniature diffusion size classifier (DiSCmini, Matter Aerosol) was used to measure the number concentration and mean diameter of particles in the range 10-300 nm. The flow rate and the sampling time interval were 1 L min^{-1} and 1 second respectively. First the instrument was used in order to have "background" data about concentration and diameter of UFPs mainly of natural and non-anthropogenic origin. For this purpose it was placed about 0.50 m off the ground in 4 sampling sites where UFPs emission from anthropogenic sources was expected to be minimum. Measurements were performed twice a day for each sampling site (two hours in the morning and two hours in the afternoon). Sites details, PM_{10} data and weather conditions are reported in Table 2.1.

Table 2.1 "Background" sites details, PM_{10} data and weather conditions (http://www.arpa.fvg.it). AM: morning, PM: afternoon, ND: data not available.

Sampling site	Day	Sampling period (hh:mm)	Wind (km h^{-1})	T_{mean} (°C)	P_{mean} (hPa)	U_{rel} (%)	PM_{10} (µg m^{-3})
Karst Plateau (Basovizza) (**site 1 AM**) 45°38'40.7''N 13°51'12.6''E	09/02/15	8:30 10:30	12	4	1021.4	51	ND
Karst Plateau (Basovizza) (**site 1 PM**) 45°38'40.7''N 13°51'12.6''E	09/02/15	16:05 17:58	12	4	1021.4	51	ND
Comprensorio S. Giovanni (**site 2 AM**) 45°39'39.6''N 13°48'17.1''E	10/02/15	8:22 10:11	5	6.2	1023.2	66	ND
Comprensorio S. Giovanni (**site 2 PM**) 45°39'39.6''N 13°48'17.1''E	10/02/15	15:40 17:40	5	6.2	1023.2	66	ND
Monte Valerio (**site 3 AM**) 45°39'45.5''N 13°47'52.5''E	11/02/15	8:12 10:12	7	7.7	1025.2	73	41
Monte Valerio (**site 3 PM**) 45°39'45.5''N 13°47'52.5''E	11/02/15	15:26 17:23	7	7.7	1025.2	73	41
Strada Vicentina (**site 4 AM**) 45°40'59.4''N 13°46'15.5''E	18/02/15	8:27 10.27	27	7.4	1035.7	47	20
Strada Vicentina (**site 4 PM**) 45°40'59.4''N 13°46'15.5''E	18/02/15	15:24 17:25	27	7.4	1035.7	47	20

Then the DiSCmini was placed in a site located in Trieste in Servola district that is interested by the presence (200 m far) of an integrated steel plant. This site was used in order to have data about number concentration and diameter of UFPs anthropogenic, mainly industrial, origin. The particle counter was also used again in the "background" site (BKD) in the Karst Plateau. Sites details, PM_{10} data and weather conditions are

reported in table (Table 2.2). PM_{10} was measured in the site by ARCO SolutionS s.r.l by means of an air quality monitoring station.

Table 2.2 Details about sampling days in the site "Servola". PM_{10} data (ARCO SolutionS s.r.l.) and weather conditions (http://www.arpa.fvg.it). ND: data not available.

Sampling day	Sampling site	Day	Sampling period (hh:mm)	Wind (km h^{-1})	T_{mean} (°C)	P_{mean} (hPa)	U_{rel} (%)	PM_{10} (µg m^{-3})
Day 1	Servola (via S. Lorenzo in Selva) 45°37'26.99"N 13°46'44.99"E	25/11/2015	10:00 16:00	13.2	7.2	1007.6	47	9
Day 2	Servola (via S. Lorenzo in Selva) 45°37'26.99"N 13°46'44.99"E	01/12/2015	10:00 16:00	4.4	11.0	1023.2	79	82
Day 3	Servola (via S. Lorenzo in Selva) 45°37'26.99"N 13°46'44.99"E	11/12/2015	10:00 16:00	2.8	8.1	1030.0	52	23
Day 4	Servola (via S. Lorenzo in Selva) 45°37'26.99"N 13°46'44.99"E	17/12/2015	10:00 16:00	2.3	11.5	1028.8	58	35
Day 5	Servola (via S. Lorenzo in Selva) 45°37'26.99"N 13°46'44.99"E	18/02/2016	10:00 16:00	2.1	11.4	1011.8	79	36
BKD	Karst Plateau (Basovizza) 45°38'40.7''N 13°51'12.6''E	02/03/2016	10:00 16:00	3.9	15.6	968.3	44	ND

2.3.2 Sampling and characterisation of aerosol particles

Sioutas Cascade Impactor (SKC) was used to collect particles both on MCE filters for the quantitative analysis of metal content and on TEM grids for morpho-chemical evaluations. In the second case two TEM grids (200 mesh copper grids coated with a 20 nm carbon support film, Media System Lab, Italy) were placed on "A" and "D" impactor stages to collect the aerosol fractions (2.5-10 µm and 0.25-0.50 µm respectively). To

secure the grids, properly sized square sections were cut from the adhesive area of 3M Post-it ® Notes and glued on the MCE impaction substrate. The adhesive portion faced upward and secured the grids in place. In this way the grids were easily removed without damage after sampling for TEM analysis (Birch et al., 2011).

The impactor was used together with DiSCmini in BKD site in the Karst Plateau near Trieste and in the sampling site located in Servola district. The instrument was secured about 1.80 m off the ground in both sampling site (see Fig. 2.5). Sampling lasted 6 hours/day in order to collect 3,000 L of air with a flow rate of 9 L min^{-1}. Site details and weather conditions are reported in table (Table 2.2).

Figure 2.5 Image of the istruments set-up.

2.3.2.1 ED-µXRF measurements

ED-µXRF measurements were conducted on a single focal spot of 1.2 x 0.1 mm^2 on some filters using an ARTAX 200 micro-X-ray fluorescence spectrometer (Bruker Nano GmbH). The instrument was set up with the following test parameters: X-ray tube, Mo target U= 50 kV, I= 700 µA, acquisition time: 120 s (live time), collimator: 650 µm (air environment).

In this study the examined elements were: Fe (line: Kα1 6.4052 keV), Mn (line: Kα1 5.9003 keV), Ni (line: Kα1 7.4803 keV), Pb (line: Lα1 10.5510 keV), Cr (line: Kα1 5.4149 keV), V (line: Kα1 4.9529 keV), Zn (line: Kα1 8.6372 keV) and Cu (line: Kα1 8.0463 keV).

2.3.2.2 TEM-EDS investigations

A JEOL (JEM 3010) electron microscope operating at 300 kV, with a point-to-point resolution of 0.17 nm, equipped with a 749 CDD Gatan Camera, coupled with an energy dispersive X-ray analyser (Oxford Instr., EDS-6636), was used to provide a detailed morpho-chemical characterisation (size distributions, shapes, microchemical data and structural information) of particles collected on TEM grids. TEM images were processed using ImageJ program.

2.3.2.3 ICP-AES analyses

The inductively coupled plasma atomic emission spectroscopy (ICP-AES) technique was used for the quantitative determination of the filter samples metal content. The instrument used for analysis was a PerkinElmer Optima 8000 equipped with autosampler S10.

All filters were digested with 3 mL of aqua regia (HCl: HNO_3 3:1) in Teflon pressure vessels by means of a microwave-assisted digestion system (Multiwave PRO, Anton Paar) following the heating program reported in Tab. 2.3. After complete dissolution, samples were diluted to 15 mL with MilliQ water. The obtained solutions were analysed for total Fe, Mn, Cr, Ni, Pb, V, Zn and Cu concentration. Analyses were conducted using a calibration curve, obtained by dilution of standard solutions for ICP-AES analyses. The limit of detection (LOD) at the operative wavelength for each element was: 0.005 mgL^{-1} for Fe at 238.204 nm, 0.001 mg L^{-1} for Mn at 257.610 nm, 0.002 mg L^{-1} for Cr at 267.716 nm, 0.010 mg L^{-1} for Ni at 231.604 nm, 0.010 mg L^{-1} for Pb at 220.353 nm, 0.010 mgL^{-1} for V at 292.464 nm, 0.004 mg L^{-1} for Zn at 206.200 nm and 0.010 mg L^{-1} for Cu at 327.393 nm. The precision of the measurements, as repeatability (RSD %), for the analysis was always less than 5%.

Table 2.3 Heating program for the microwave-assisted digestion procedure.

Step	Program	Temperature (°C)	Time (mm:ss)
1	Temperature ramp	195	12:00
2	Temperature hold		45:00
3	Cooling	50	25:00

3. Results

3.1 Real-time measurements

Fig. 2.6 shows the temporal evolution of particle number concentration (a) and particle size (b) in the four background sites. The average values of these two parameters are reported in Tab 2.4.

Table 2.3 Results obtained in the "background" sites for particle number concentration (mean and standard deviation SD, median) and particle size (mean and SD, median).

	Particle number concentration PNC (pt/cm^3)		Diameter (nm)	
Sampling site	Mean (SD)	Median	Mean (SD)	Median
Karst Plateau (Basovizza) (**site 1 AM**)	3,681 (655)	3,599	41 (3)	41
Karst Plateau (Basovizza) (**site 1 PM**)	14,870 (14,353)	10,870	38 (7)	40
Comprensorio S. Giovanni (**site 2 AM**)	20,586 (5,180)	22,676	48 (3)	49
Comprensorio S. Giovanni (**site 2 PM**)	21,457 (5,832)	21,233	53 (2)	52
Monte Valerio (**site 3 AM**)	18,278 (9,756)	16,533	47 (7)	44
Monte Valerio (**site 3 PM**)	9,199 (1,173)	9,155	68 (5)	68
Strada Vicentina (**site 4 AM**)	5,084 (623)	4,999	74 (6)	74
Strada Vicentina (**site 4 PM**)	6,208 (1,330)	6,073	63 (5)	63

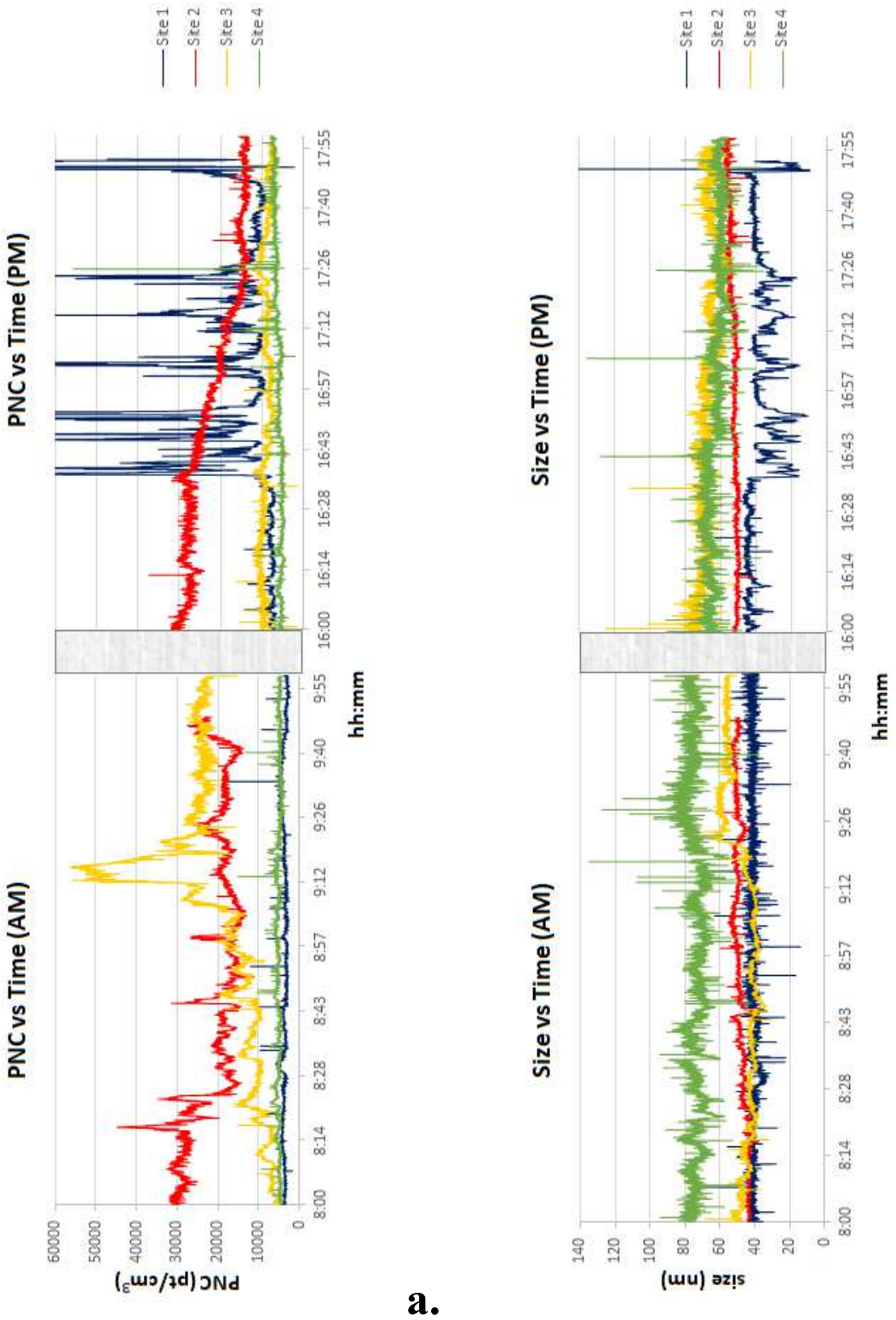

Figure 2.6 Temporal evolution of particle number concentration (a) and particle size (b) in the 4 background sites. Blue: site 1, red: site 2, yellow: site 3 and green: site 4. Peaks off the scale have been graphically hidden in order to better appreciate the main profile.

Fig. 2.7 and Fig. 2.8 show, respectively, the temporal evolution of particle number concentration and particle size during all sampling days in the site “Servola” and in the BKD site in the Karst Plateau. The average values of these two parameters are reported in Table 2.4.

Table 2.4 Results obtained in the site “Servola” for particle number concentration (mean and standard deviation SD, median) and particle size (mean and SD, median).

	Particle number concentration PNC (pt/cm^3)		Diameter (nm)	
Servola (via S. Lorenzo in Selva) Sampling day	Mean (SD)	Median	Mean (SD)	Median
Day 1	9,510 (3,384)	8,788	47 (5)	47
Day 2	14,427 (8,895)	12,202	87 (14)	86
Day 3	23,766 (15,397)	17,929	47 (5)	49
Day 4	27,550 (12,338)	22,502	53 (8)	53
Day 5	28,416 (21,476)	20,225	43 (5)	43
BKD	6,857 (3,522)	6,289	56 (8)	55

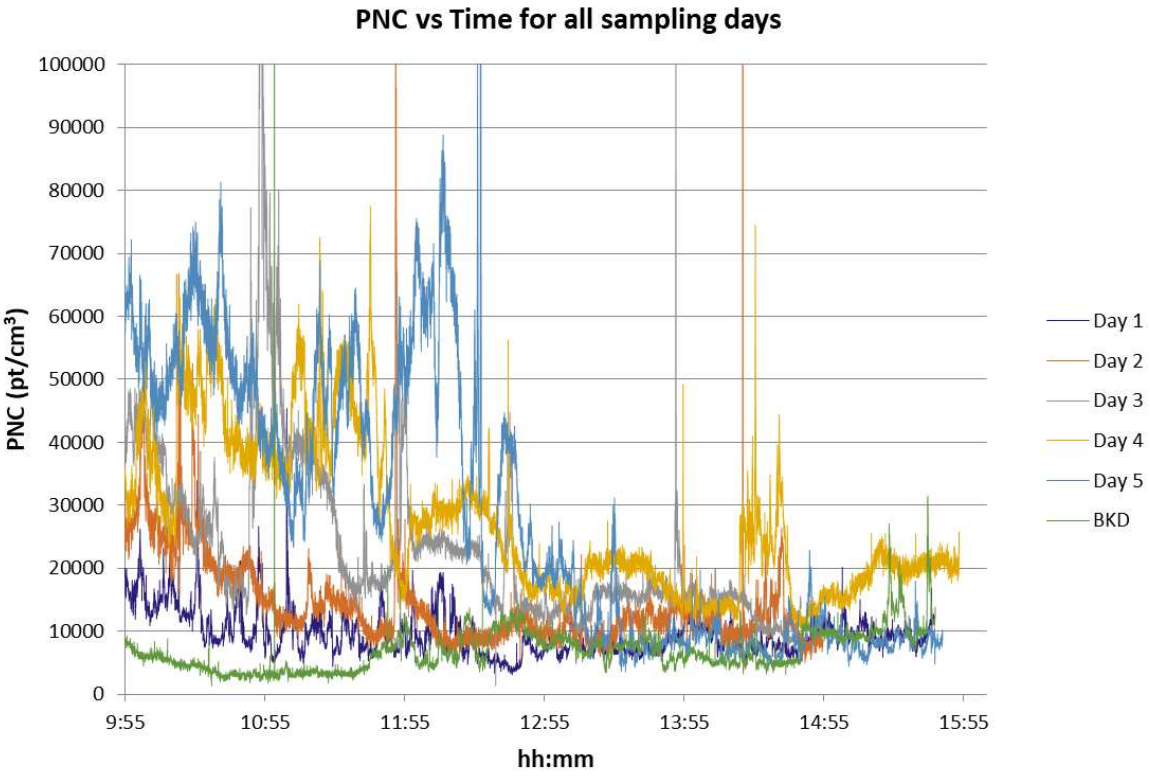

Figure 2.7 Temporal evolution of particle number concentration during the sampling days in the site "Servola" (Blue: Day 1, orange: Day 2, grey: Day 3, yellow: Day 4 and light blue: Day 5) and in the BKD site (green). Peaks off the scale have been graphically hidden in order to better appreciate the main profile.

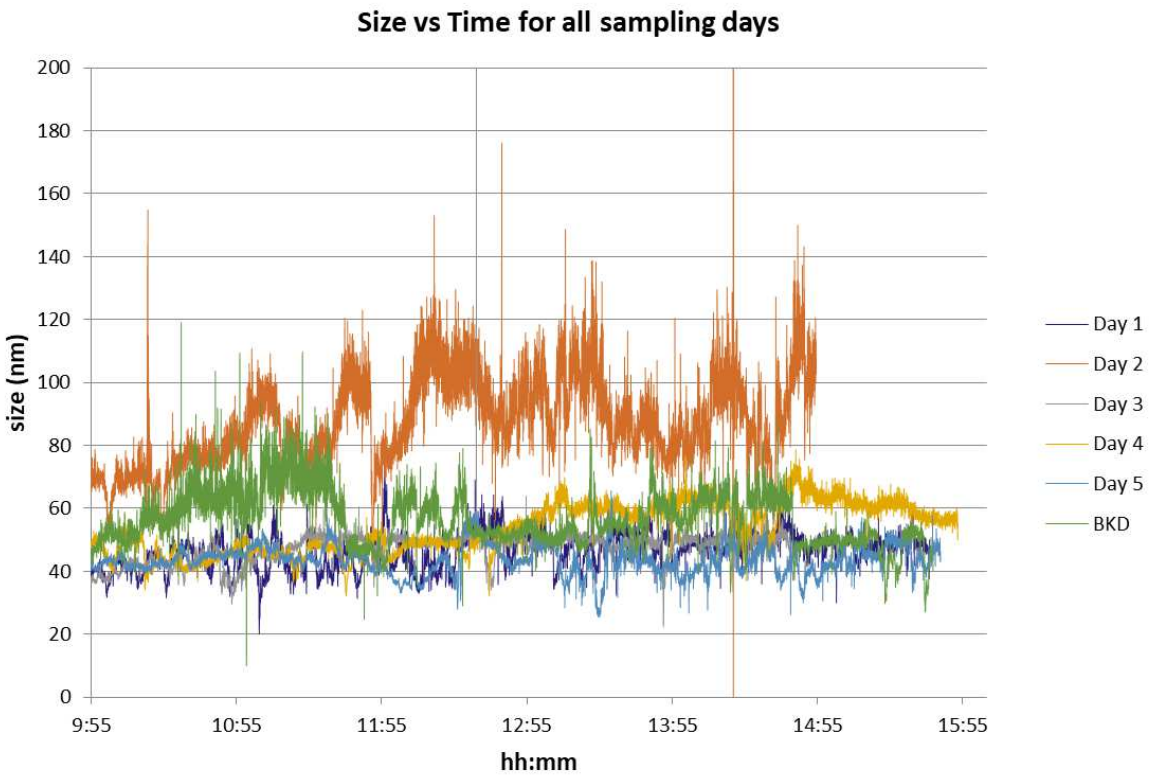

Figure 2.8 Temporal evolution of particle size during the sampling days in the site "Servola" (Blue: Day 1, orange: Day 2, grey: Day 3, yellow: Day 4 and light blue: Day 5) and in the BKD site (green). Peaks off the scale have been graphically hidden in order to better appreciate the main profile.

3.2 Characterisation of aerosol particles

3.2.1 ED-µXRF measurements

Representative ED-µXRF spectra acquired on filters placed on stage "B", "C" and "D" of the impactor and on a "blank" filter are shown in Fig. 2.9 to make a comparison. Spectra were acquired on one point of the dark line characteristic of the stages "A"-"D" corresponding to the particle deposit (see Fig. 2.10), while for the blank filter data were acquired in a central point.

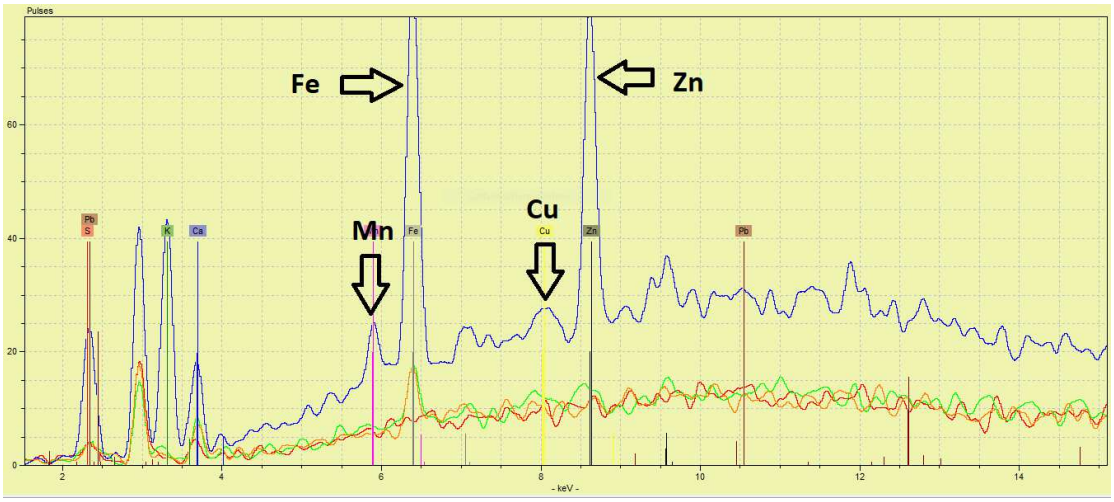

Figure 2.9 Representative ED-µXRF spectra acquired on filters placed on stage "B" (orange), "C" (green) and "D" (blue) of the impactor and on a "blank" filter (red).

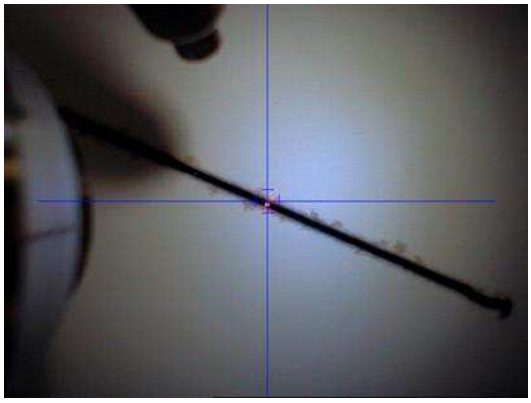

Figure 2.10 ED-µXRF acquisition point on the line corresponding to the particle deposit.

Signals characteristic of Fe, Zn, Mn and Cu can be observed in the spectrum of stage “D” filter (blue), while only the signal of Fe is distinguishable on stage “B” (orange) and “C” (green) filters if compared to the “blank” filter (red). No significant differences between spectra acquired on “after filters” (collection of particles < 0.25 μm) and “blank” filters were observed. It has to be noticed that the deposition of particles on “after filter” is spread on all the filter area resulting in a dilution of the particulate matter if compared to the other stages.

3.2.2 TEM-EDS investigations

Figs. 2.11-2.14 show representative TEM images and EDS spectra of particles collected on TEM grids in “Servola” site. It should be noticed that the characteristic peaks due to the material of the grid (C, Cu) are present in all acquired spectra.

In Fig. 2.11 a particle with its highest dimension of about 0.500 μm can be observed. It is mainly composed of low atomic weight elements as Al, Si and O probably in the form of silicates. On the surface of this particle a chainlike agglomerate of crystalline nanoparticles (10-20 nm) can be seen. EDS analysis performed with higher magnification reveals that these nanoparticles are mainly composed of Fe and Mn.

Fig. 2.12 shows an agglomerate of irregular plate-like particles overlapped. The highest dimension of this agglomerate is about 2 μm and it is mainly composed of Al, Si an O. Nanoparticles composed of Fe can be observed using a higher magnification on the agglomerate.

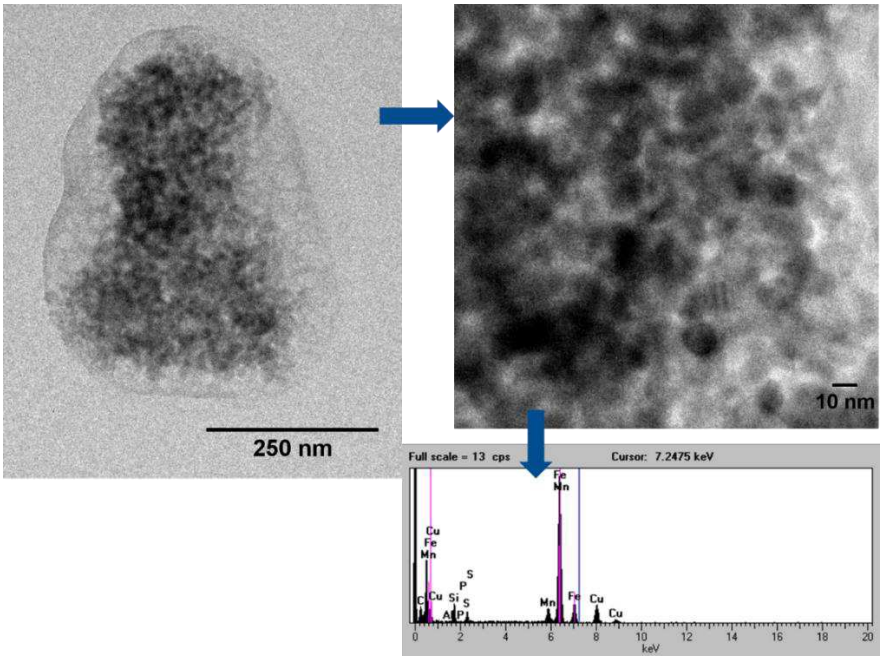

Figure 2.11 Representative TEM images and EDS spectrum of particles found on a TEM grid collected in "Servola" site. Scale bar: 250 nm (image on the left), 10 nm (image on the right). Spectrum refers to a compound containing Fe and Mn.

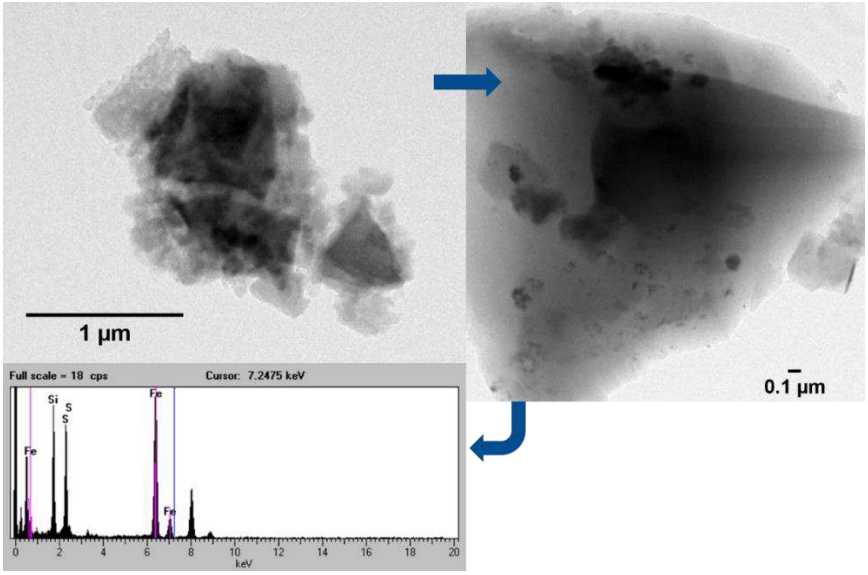

Figure 2.12 Representative TEM images and EDS spectrum of an agglomerate of particles found on a TEM grid collected in "Servola" site. Scale bar: 1 µm (image on the left), 100 nm (image on the right). Spectrum refers to a compound containing Fe.

In Fig. 2.13 a nanoparticle (about 20 nm) mainly composed by Fe can be observed inside a structure of higher dimension. Fig. 2.14 shows a submicron particle (about 0.500 µm) mainly composed by Zn.

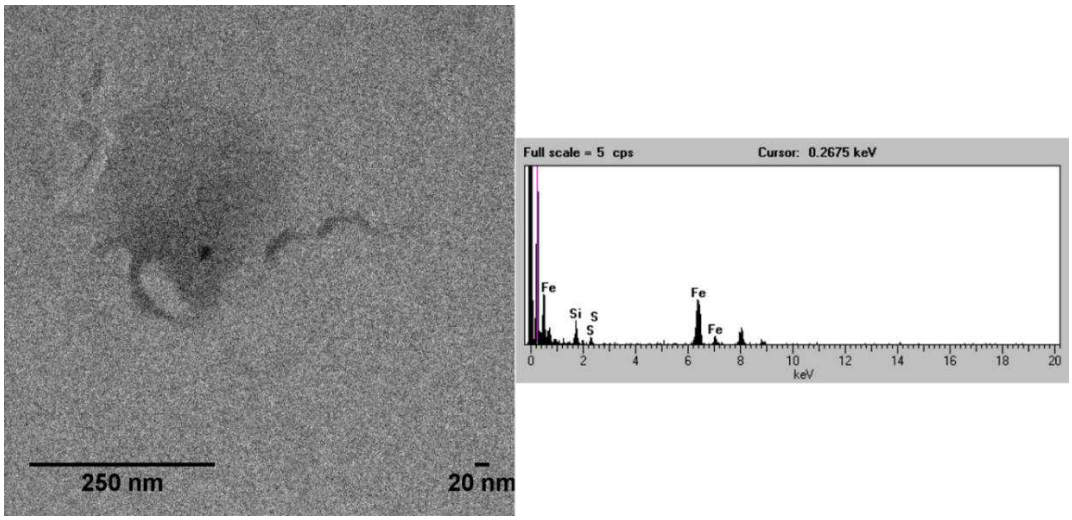

Figure 2.13 Representative TEM image and EDS spectrum of a nanoparticle found on a TEM grid collected in "Servola" site. Scale bar 20 nm. Spectrum refers to a compound containing Fe.

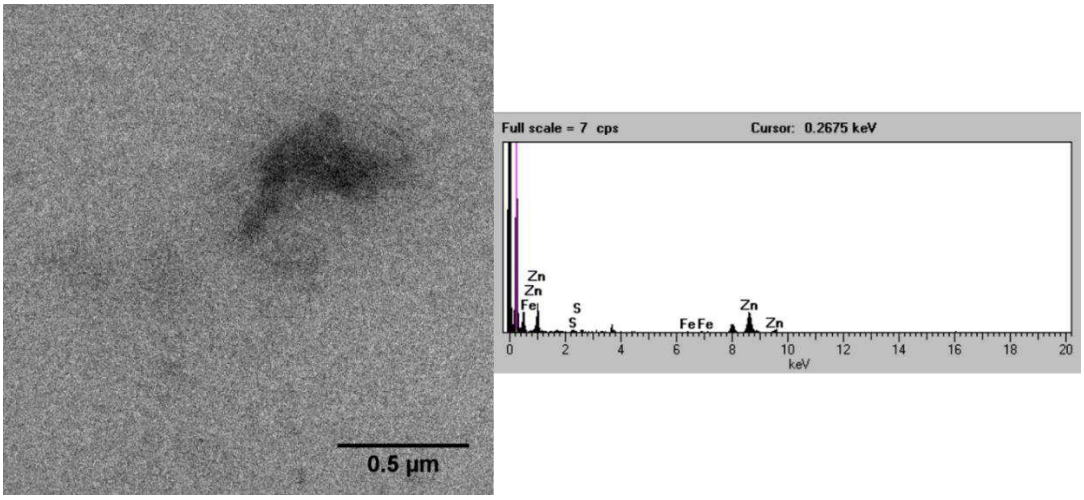

Figure 2.14 Representative TEM image and EDS spectrum of a particle found on a TEM grid collected in "Servola" site. Scale bar 500 nm. Spectrum refers to a compound containing Zn.

3.2.3 ICP-AES analyses

Results obtained from ICP-AES analyses of the filters in each stage of the impactor are reported in Table 2.5. Metal content is expressed as a function of the air volume sampled in the "Servola" site and in the BKD site in the Karst Plateau.

Table 2.5 Metals concentration (μg m^{-3}) in each stage of the impactor for all the sampling days in the site "Servola" and in the "background" (BKD) site. *TEM grids were placed in stage A and D so there are no quantitative data for these stages.

	Fe	Mn	Cr	Ni	Pb	V	Zn	Cu
Day 1 Servola*								
After filter	0.265	0.018	0.027	<0.047	<0.047	<0.047	0.163	<0.047
Stage C	0.067	<0.005	<0.009	<0.047	<0.047	<0.047	0.066	<0.047
Stage B	0.081	<0.005	<0.009	<0.047	<0.047	<0.047	0.129	<0.047
Day 2 Servola								
After filter	0.184	0.006	<0.009	<0.047	<0.047	<0.047	0.090	<0.047
Stage D	0.119	0.009	<0.009	<0.047	<0.047	<0.047	0.126	<0.047
Stage C	0.104	<0.005	<0.009	<0.047	<0.047	<0.047	0.088	<0.047
Stage B	0.186	<0.005	<0.009	<0.047	<0.047	<0.047	0.084	<0.047
Stage A	0.452	0.021	0.022	<0.047	<0.047	<0.047	0.119	<0.047
Day 3 Servola								
After filter	0.254	<0.005	<0.009	<0.047	<0.047	<0.047	0.115	<0.047
Stage D	0.124	<0.005	<0.009	<0.047	<0.047	<0.047	0.067	<0.047
Stage C	0.129	<0.005	<0.009	<0.047	<0.047	<0.047	0.077	<0.047
Stage B	0.206	0.008	<0.009	<0.047	<0.047	<0.047	0.077	<0.047
Stage A	0.359	<0.005	<0.009	<0.047	<0.047	<0.047	0.144	<0.047
Day 4 Servola								
After filter	0.184	0.006	<0.009	<0.047	<0.047	0.049	0.107	<0.047
Stage D	0.168	0.006	<0.009	<0.047	<0.047	<0.047	0.076	<0.047
Stage C	0.149	<0.005	<0.009	<0.047	<0.047	<0.047	0.063	<0.047
Stage B	0.247	<0.005	0.009	<0.047	<0.047	<0.047	0.069	<0.047
Stage A	0.479	0.006	<0.009	<0.047	<0.047	<0.047	0.070	<0.047
Day 5 Servola								
After filter	0.891	0.010	<0.009	<0.047	<0.047	<0.047	0.080	<0.047
Stage D	0.586	0.007	<0.009	<0.047	<0.047	<0.047	0.048	<0.047
Stage C	0.907	0.009	0.060	<0.047	<0.047	<0.047	0.040	<0.047
Stage B	1.700	0.006	<0.009	<0.047	<0.047	<0.047	0.062	<0.047
Stage A	3.259	0.009	<0.009	<0.047	<0.047	<0.047	0.057	<0.047
BKD								
After filter	0.144	<0.005	<0.009	<0.047	<0.047	<0.047	0.106	<0.047
Stage D	0.046	<0.005	<0.009	<0.047	<0.047	<0.047	0.051	<0.047
Stage C	0.056	<0.005	<0.009	<0.047	<0.047	<0.047	0.065	<0.047
Stage B	0.171	<0.005	<0.009	<0.047	<0.047	<0.047	0.051	<0.047
Stage A	0.093	<0.005	<0.009	<0.047	<0.047	<0.047	0.079	<0.047

4. Discussion

4.1 Real-time measurements in “background” sites

Fig. 2.15 shows the comparison of the mean PNC and the average particle size between the four “background” sites along morning and afternoon measurements.

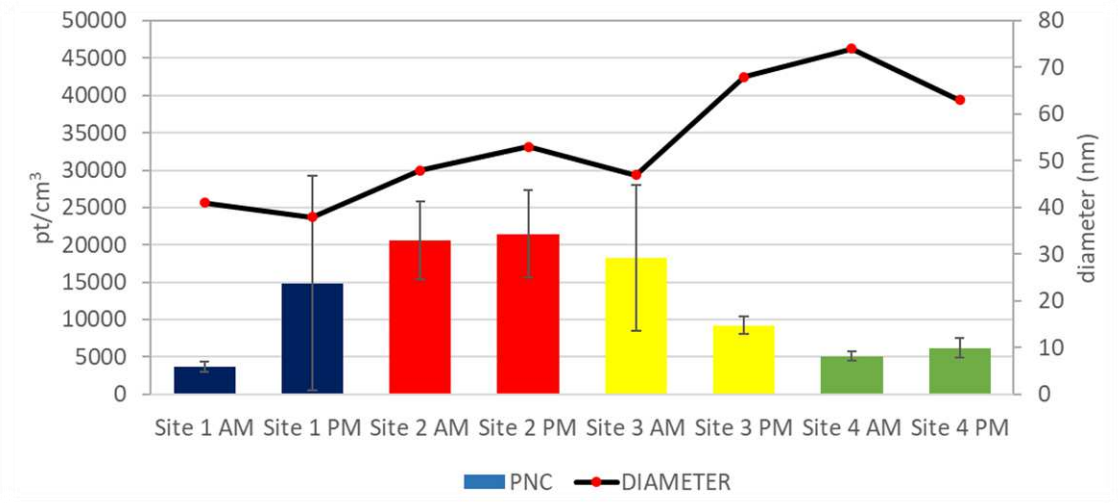

Figure 2.15 Comparison of the mean PNC (bars) and the average particle size (dots) between the “background” sites in morning (AM) and afternoon (PM) measurements.

UFPs emission from anthropogenic sources was expected to be minimum in the chosen sampling sites, but a certain variability in the results can also be noted between measurements performed in the same sampling site in different hours of the same day. Taking into account the intrinsic variability between the sites, the average value of PNC and diameter of particles in the size range 10-300 nm was 12,420 particles cm^{-3} and 54 nm respectively.

It should be noted that an inverse relation was found between the average PNC for each site and the wind speed during the sampling days (Fig. 2.16). In these terms both the characteristics of the sites and the wind condition could justify the differences in the results. The influence of the variable "weather conditions" would probably reduce if the measure of PNC cover the same site for a longer period of time.

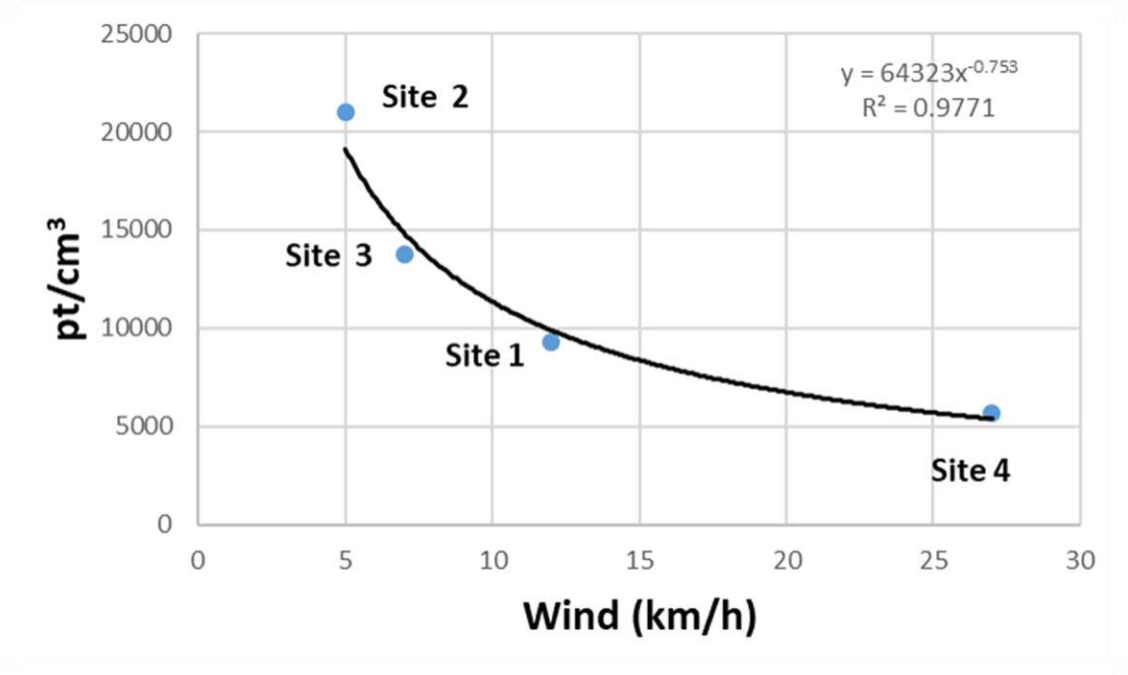

Figure 2.16 Relation between the daily average PNC and the wind speed for all the "background" sites.

In a review of the literature about airborne UFPs, Morawska et al. (2008) suggested 2,000-4,000 particles cm^{-3} as a typical range for UFPs number concentration in "clean" background and rural environments. Our results seem to be comparable only for Site 4 that in fact was located on a mountain path.

In another review Kumar et al. (2010) reported that the typical range of UFPs number concentration measured in forest regions, remote continental, desert and rural (or city background) is 10^3-10^4, in line with our average results.

Two-years measurement of UFPs number concentration in a botanic garden in Rome revealed a mean value of 25,000 particles cm^{-3} (Marconi et al., 2007).

Reche et al. (2011) measured an average PNC of 14,945 particle cm^{-3} in the submicron range in a background site in Lugano (50 m to the east there was a busy urban road but buildings protected the site from direct road traffic emissions towards all other wind directions).

Given these considerations our results seem to be substantially in line with previous studies reported in literature for "background" sites.

4.2 Real-time measurements in "Servola" site

Fig. 2.17 shows the comparison of the mean PNC and the average particle size between the five sampling days in "Servola" site.

Also in this case, the inverse relation existing between the mean PNC for each sampling day and the wind speed could justify some differences in the results (Fig. 2.18).

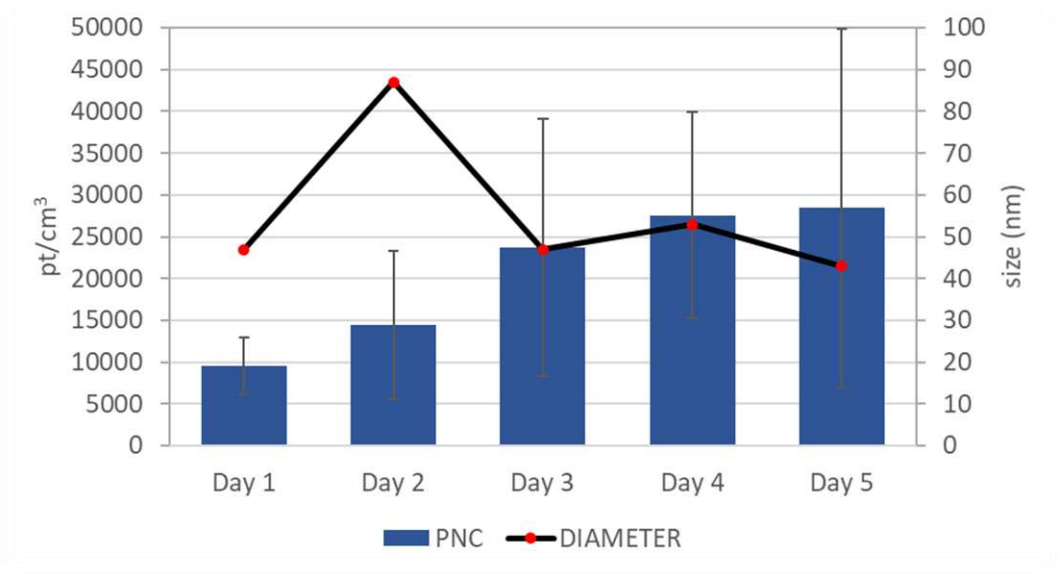

Figure 2.17 Comparison of the mean PNC (bars) and the average particle size (dots) between the five sampling days in "Servola" site.

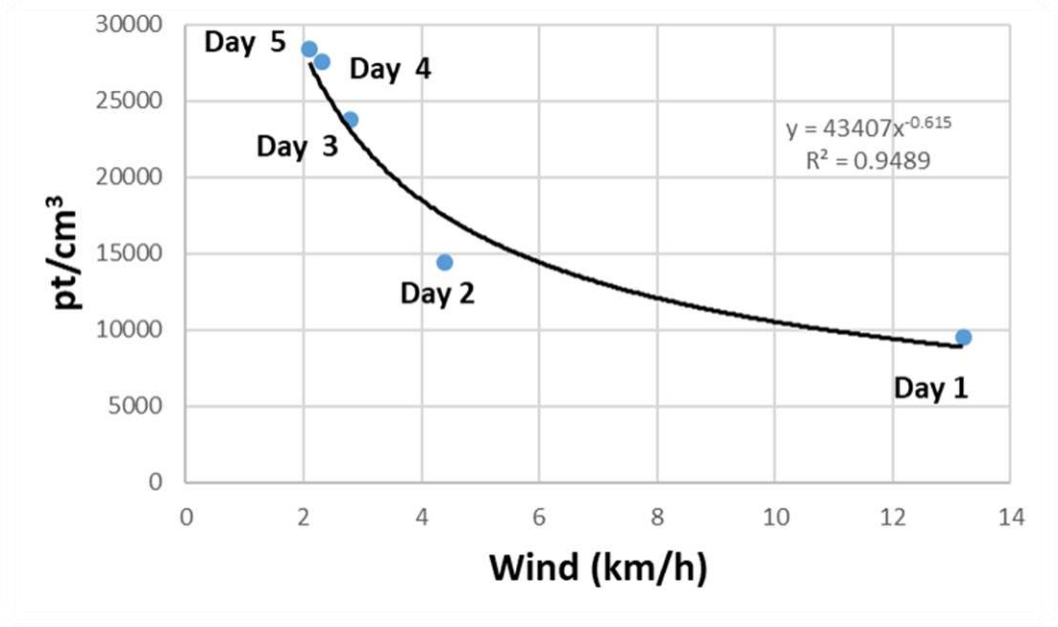

Figure 2.18 Relation between the daily average PNC and the wind speed for all the sampling days in the "Servola" site.

Mediating the results of all sampling days, the average value of PNC and diameter of particles in the size range 10-300 nm in "Servola" site where the emission source is supposed to be anthropic, mainly industrial, was 20,734 particles cm^{-3} and 55 nm respectively. Despite similar values of mean diameter, the PNC in "Servola" site was more than twice higher if compared to the BKD site in the Karst Plateau (Fig. 2.19). In the BKD site (the same of the "background" site 1 where the average PNC and diameter was 9,275 particles cm^{-3} and 40 nm respectively) the mean PNC and average diameter was 6,857 particles cm^{-3} and 56 nm respectively.

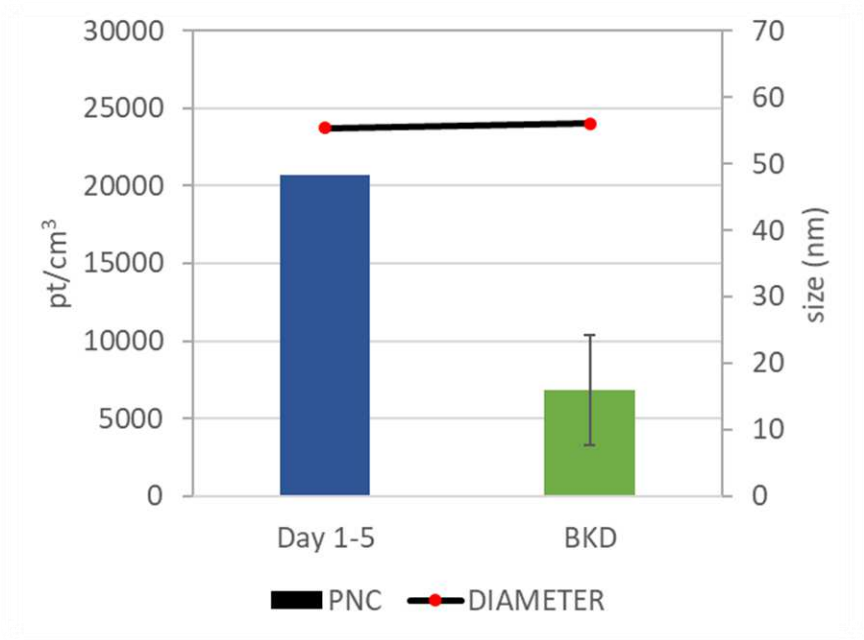

Figure 2.19 Comparison of the average PNC (bars) and the average particle size (dots) between the five sampling days in "Servola" site and the BKD site.

Reche et al. (2011) measured at four selected urban air quality monitoring sites covering road traffic, urban-industrial, and urban-shipping environments, from southern, central and northern Europe, a number concentration of particles in the submicron range from

about 20,000 up to 30,000 particles cm^{-3}. They concluded that the results showed that the variations of number concentration levels in submicron range do not always reflect the variation of the impact of road traffic emissions on urban aerosols.

Morawska et al. (2008) suggested 10,000-50,000 particles cm^{-3} as a typical range for UFPs number concentration in urban environments.

Two-years measurement of UFPs number concentration in a traffic-oriented site in Rome revealed a mean value of 47,000 particles cm^{-3} (Marconi et al., 2007).

In the summer of 2015 we performed real-time measurements of PNC and size closer to the integrated steel plant (75 m from the plant). The results are reported in Fig. 2.20 as a comparison. Nucleation mode particles (1-30 nm) are found in high number concentrations near sources (Kumar et al., 2010) and this could explain the decrease of PNC in "Servola" site that was located 200 m from the plant suggesting that the distance is a critical point for UFPs number concentration measurements.

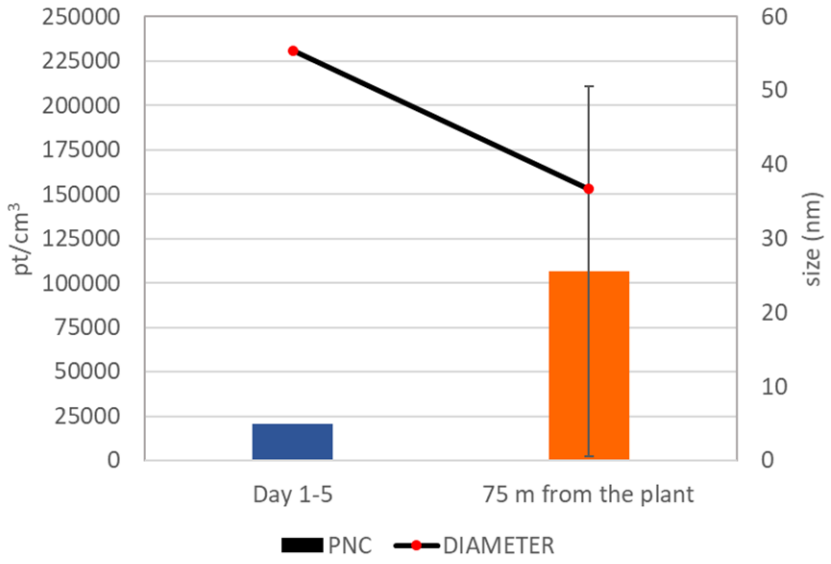

Figure 2.20 Comparison of the average PNC (bars) and the average particle size (dots) between the five sampling days in "Servola" site and a site located 75 m far from the plant.

Fig. 2.21 shows the data acquired during sampling Day 4, as a representative day, in "Servola" site, showing the temporal evolution of PNC and particle size: generally, an increase of the former corresponds to a decrease of the latter and vice versa, resulting in two specular profiles.

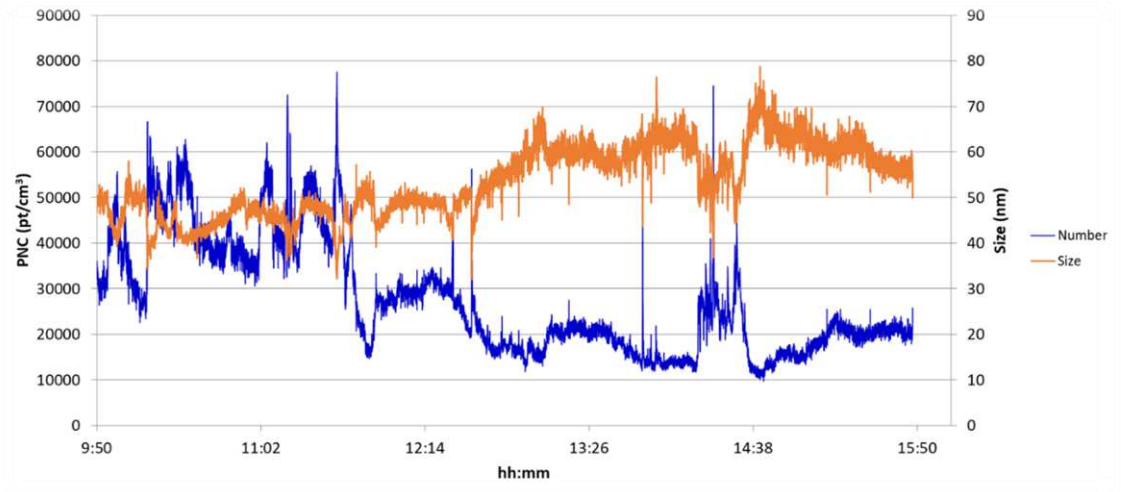

Figure 2.21 Temporal evolution of PNC and particle size in "Servola" site during Day 4.

Plotting PNC versus particle size, an inverse relation was confirmed for each sampling days in "Servola" site (see Fig 2.22 for sampling Day 4). High PNC values for smaller particles (1-30 nm) could be compatible with nucleation events. On the other hand, lower PNC values for bigger particles (20-100 nm) could be compatible with the growth or coagulation of nucleation mode particles (Kumar et al., 2010).

Using this kind of graphical representation a peculiarity was revealed for sampling Day 5. The inverse relation between PNC and particle size seems to divide the collected data in two subsets corresponding to morning and afternoon acquisitions respectively (Fig. 2.23). PNC decreased from a mean value of 44,830 particles cm^{-3} in the morning to 9,026 particles cm^{-3} in the afternoon. A hypothesis for this difference could be a change related to the emission source.

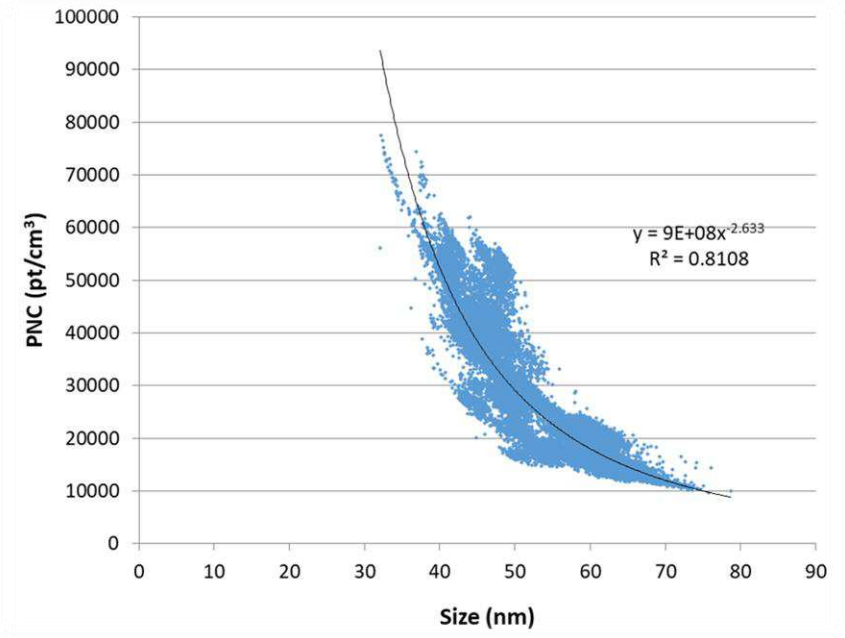

Figure 2.22 Relation between PNC and particle size during Day 4 in the "Servola" site.

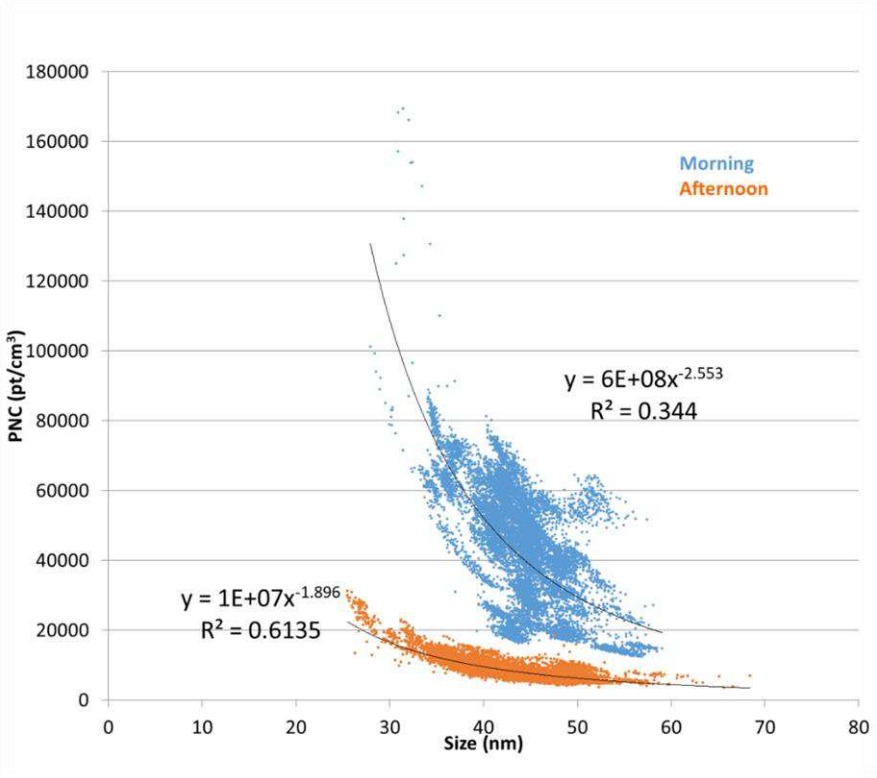

Figure 2.23 Relation between PNC and particle size during Day 5 in the "Servola" site. Blue cluster: morning data, orange cluster: afternoon data.

4.3 Characterisation of aerosol particles

ED-μXRF analysis performed on filters sampled in "Servola" site showed the presence of Fe, Zn and Mn in the particulate matter. The same elements constituted agglomerates of nanoparticles observed by means of TEM-EDS and were those with a concentration (μg m^{-3}) higher than the limit of detection (LOD) in the quantitative analysis performed using ICP-AES.

Other elements that were chosen as possible markers of the industrial activity were not detected by all the techniques used for the characterisation of the particulate matter.

For what concern ICP-AES analyses, the length of collection period is a very critical point because of the lower sensitivity than other analytical techniques (e.g., ICP-MS).

Extending the collection period using a cascade impactor, the probability of particles loss from the impaction stages increases. Giving these considerations, a suitable compromise has to be found.

Moreover, the Sioutas Cascade Impactor is normally used for the evaluation of workers exposure during the work shift (8 hours) in occupational settings, mainly indoor, where a minor dilution of particulate matter occurs. In ambient conditions cascade impactors typically require sampling times of several days (Sanderson et al., 2014; Malandrino et al., 2016).

The concentration of Fe and Zn (μg m^{-3}) for each impaction stage is reported in Table 2.6 as mean value resulting from sampling Day 2 to 5 in "Servola" site. Day 1 is not

considered because data for the impaction stages were not complete due to the presence of TEM grids for particles collection.

Fe and Zn concentration in PM_{10} and PM_1 fractions are reported in Table 2.6 as sum of concentrations for all the stages and stages C, D and after filter respectively. Data obtained in BKD site are reported in bracket for a comparison.

Table 2.6 Mean concentration of Fe and Zn (µg m^{-3}) for each impaction stage and in PM_{10} and PM_1 fractions measured in the sampling days (Day 2-5) in the site "Servola".

Impaction stage (size range)	**Fe (µg m^{-3})**	**Zn (µg m^{-3})**
After filter (< 0.25 µm)	0.378	0.098
Stage D (0.25–0.50 µm)	0.249	0.079
Stage C (0.5–1.0 µm)	0.322	0.067
Stage B (1.0–2.5 µm)	0.585	0.073
Stage A (2.5–10 µm)	1.137	0.098
PM_{10}	2.672	0.415
PM_1	0.950 (0.246 in BKD site)	0.244 (0.222 in BKD site)

Fig. 2.24 shows the difference in terms of Fe and Zn concentration in PM_1 fraction between "Servola" and BKD sites. Taking into account that soil is considered an important source of Fe in the aerosol, the major difference between the two sites, as expected, is represented by an increase of the Fe concentration in proximity of the integrated steel plant. For Zn this increase does not occur.

To make a comparison Fe and Zn average concentration in PM_1 in three urban sites in Italy were in the range 24-86 ng m^{-3} and 9-59 ng m^{-3} respectively (Vecchi et al., 2008). These results are lower than our BKD data.

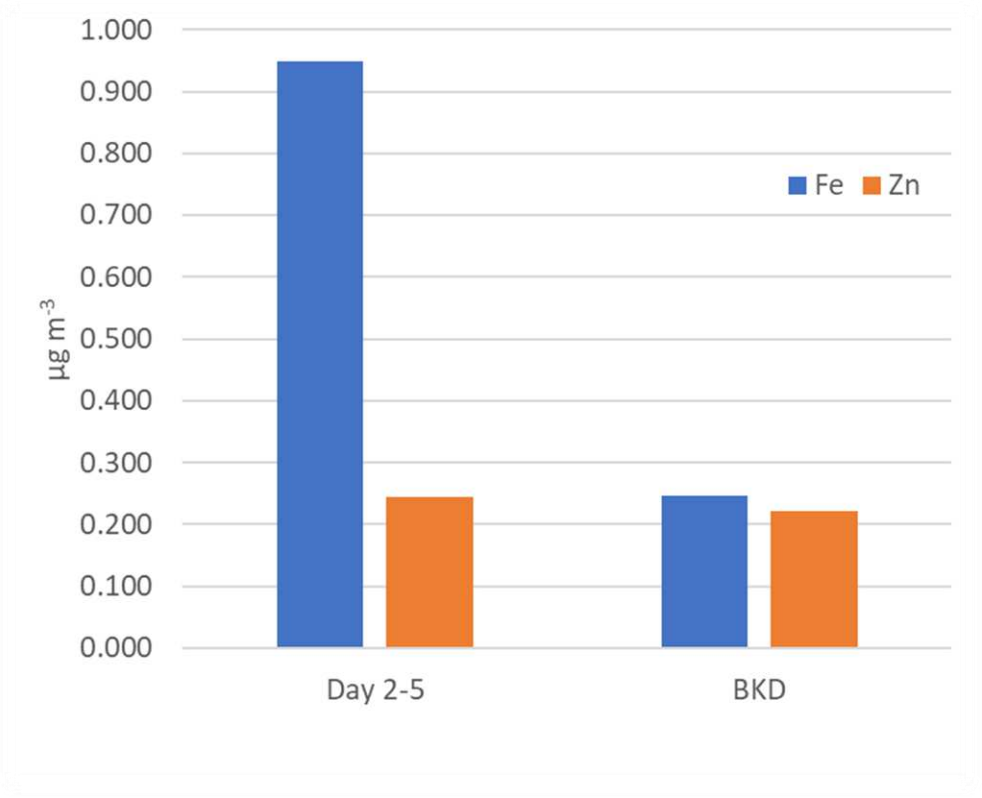

Figure 2.24 Comparisons of the average Fe (blue) and Zn (orange) concentration (µg m^{-3}) in PM_1 between sampling days in the site "Servola" (Day 2-5) and in the BKD site.

Fe and Zn distribution in the different size ranges of particles collected in “Servola” is reported in Fig. 2.25 and Fig. 2.26 respectively.

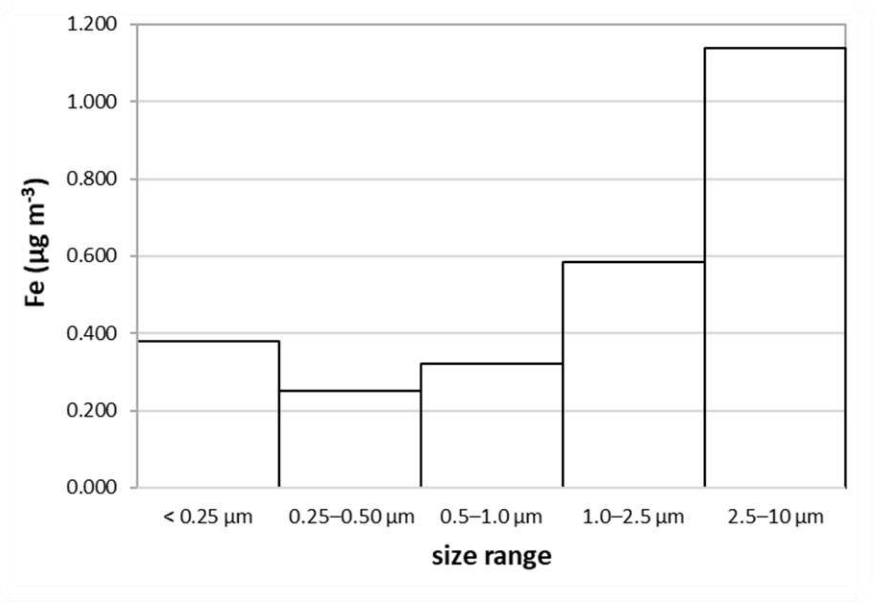

Figure 2.25 Fe distribution (µg m^{-3}) in the different size ranges of particles collected in “Servola” site.

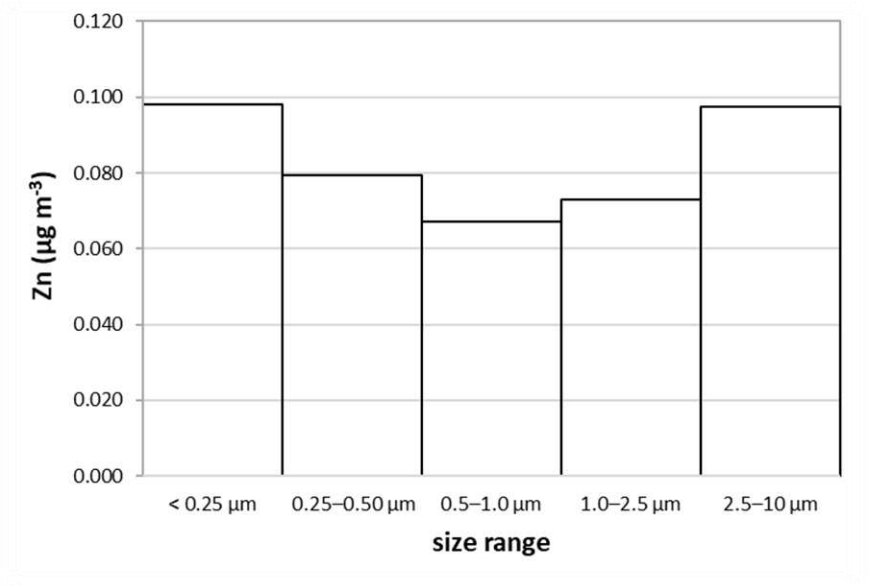

Figure 2.26 Zn distribution (µg m^{-3}) in the different size ranges of particles collected in “Servola” site.

Mohiuddin et al. (2014) selected three sites in the vicinity of Australian iron and steel industries for sampling of size resolved particulate matter using a MOUDI sampler that provided ten different PM size ranges (>18, 10-18, 5.6-10, 3.2-5.6, 1.8-3.2, 1-1.8, 0.56-1, 0.32-0.56, 0.18-0.32, <0.18 μm).

They reported a total mass concentration for PM_1 ranging from 2.3 to 10.6 μg m^{-3} depending on the site.

The chemical composition of the collected particles was analysed using the proton induced X-ray emission technique (PIXE). Extrapolating data from the graphs reported in that study, Fe concentration in the PM_{10} fraction was about 3 μg m^{-3} (about 10% of PM_{10} mass concentration) in one of the sampling site. Fe concentration in the PM_1 fraction was about 1.3 μg m^{-3}. These results seem to be substantially in agreement with our results.

They also reported that Fe showed a bimodal distribution in that site: a mode at 0.18-0.56 μm and a mode at 1.8-5.6 μm similar to our results.

Bernardoni and coworkers (2011) performed ED-XRF analysis of size-segregated aerosol samples collected at urban background sites in the cities of Florence and Milan and at a traffic site in Genoa. They observed a big mode at diameters higher than 2.5 μm for Fe, while the contribution at sizes lower than a few tenths of micrometres was almost negligible. This difference with our results could be due to completely different kind of source.

Despite a significant difference in terms of mass concentration, likely due to the different characteristics of the sampling sites, Malandrino et al. (2016) reported a higher Fe concentration in the size range <0.54 μm with respect to the fraction 0.54-1.6 μm similar

to our results. Their data refer to a sampling campaign conducted in October 2011 in the city of Turin using the 8-stages Andersen cascade impactor.

One year-long sampling campaign of quasi-ultrafine particles (<0.25 μm) was conducted at ten distinct locations across the Los Angeles south coast air basin by Saffari et al. (2013). Samplings were performed by means of the same kind of impactor used in our study. Fe and Zn average concentration in the particle fraction <0.25 μm (after filter) were in the range 11-38 ng m^{-3} and 0.9-3.1 ng m^{-3} respectively. Our results for the same particle fraction are considerably higher. This could be due in part to the different kind of emission source (mainly industrial in our case, traffic related in the study performed in Los Angeles), in part to an overestimation of the finest fraction in our study caused by particle bouncing-off phenomena inside the sampler (Giorio et al., 2013). In impactor samplers particles can bounce on an impaction stage re-entering the airstream and depositing on the next stage. The use of impactor grease and/or Teflon filters (Misra et al., 2002) is suggested in order to minimize bouncing-off phenomena but in many cases this preventative measure is not enough (Giorio et al., 2013; Hedmer et al., 2015).

Using OPC daily counts and PM_{10} mass concentration measured in "Servola" site in a period before and after the blast furnace shut down, Licen et al. (2016) built an in-house script in R environment to assign a density to particles of different size (OPC counts the particles in eight size bins centered in 0.3, 0.5, 0.7, 1.0, 2.0, 3.0, 5.0 and 10.0 μm mean diameter respectively). Considering that Fe density is 7.96 g cm^{-3} and that a density of 1.65 g cm^{-3} is considered to be related to urban traffic sources, they used 1-8 g cm^{-3} density to perform the calculation. High density found for particles <0.3 μm after the blast closing is compatible with the emissions of a steel plant and is possibly due to the long residence

time in atmosphere of UFPs. These results support our findings justifying the not negligible contribution of Fe concentration in the particle fraction <0.25 μm.

Moreover, in literature it is reported that the industrial fraction of Fe at the submicron and ultrafine size particles near iron and steel industries is estimated to range up to 95% which is most likely a result of emissions from high temperature thermal activities (Mohiuddin et al., 2014).

5. Conclusions

Despite some differences in the results between the "background" sites probably linked, at least in part, to different wind conditions, number concentration of particles in the range 10-300 nm in "Servola" site was about twice higher. On average little difference in mean diameter were observed.

A general observation on the real-time measurements performed in this study is that an increase of the PNC corresponds to a decrease of the particle size and vice versa. High PNC values for smaller particles (1-30 nm) could be compatible with nucleation events close to the emission source. On the other hand lower PNC values for bigger particles (20-100 nm) could be compatible with the growth or coagulation of nucleation mode particles (Kumar et al. 2010).

ED-μXRF analysis performed on filters sampled in "Servola" site showed the presence of Fe, Zn and Mn in the particulate matter. The same elements constituted agglomerates of nanoparticles observed by means of TEM-EDS and were those with a concentration ($\mu g\ m^{-3}$) higher than the limit of detection (LOD) in the quantitative analysis performed using ICP-AES.

The contribution of Fe concentration in the PM_1 and, in particular, in the particle fraction <0.25 μm seems to be not negligible in accordance with previous studies performed in similar environments (Mohiuddin et al., 2014; Licen et al., 2016). This result is highly significant from a toxicological point of view.

Fe is an essential element for the human body but not in the form of inhalable particles as iron-reach particles can stimulate the production of ROS that are major contributing factor in inflammation and toxicity (Gwinn and Vallyathan, 2006).

Servola district is densely inhabited and people live very close to the integrated steel plant that is a relevant emission source.

The aim of this study was a first approach to a topic of major concern such as UFPs emissions in ambient air from industrial activities.

Some improvements in the sampling strategy should be introduced to examine the topic deeper. First of all more suitable instruments for sampling size-resolved particles in ambient air continuously for longer period of time should be chosen (e.g. MOUDI, ELPI). This could increase the amount of sampled material and thus, using offline analytical techniques with higher sensitivity (e.g. ICP-MS), a more complete chemical characterisation could be performed also in terms of source apportionment evaluation.

At the same time an evaluation of the effects of particle bouncing-off phenomena inside cascade impactors should be performed in order to reduce the probability of overestimate the contribution of the finest particle fraction.

In order to have a statistical relevance, more TEM-EDS analyses should be performed for the morpho-chemical characterisation of the particles that is important in the evaluation of possible toxicological effects.

References

AQEG (2005). *Particulate Matter in the United Kingdom*. AQEG, Defra, London.

Asbach, C., Kaminski, H., Fissan, H., Monz, C., et al. (2009). Comparison of four mobility particle sizers with different time resolution for stationary exposure measurements. *J. Nanopart. Res.* 11: 1593-1609.

Bernardoni, V., Cuccia, E., Calzolai, G., Chiari, M., et al. (2011). ED-XRF set-up for size-segregated aerosol samples analysis. *X-Ray Spectrom*. 40: 79–87.

Birch, M. E., Ku, K., Evans, D. E. and Ruda-Eberenz, T. A. (2011). Exposure and Emission Monitoring during Carbon Nanofiber Production – Part I: Elemental Carbon and Iron-Soot Aerosols. *Ann. Occup. Hyg*. 55(9): 1016-1036.

Buonanno, G., Stabile, L., Avino, P. and Belluso, E. (2011). Chemical, dimensional and morphological ultrafine particle characterization from a waste-to-energy plant. *Waste Manag.* 31(11): 2253-2262.

Cernuschi, S., Giugliano, M., Ozgen, S. and Consonni, S. (2012). Number concentration and chemical composition of ultrafine and nanoparticles from WTE (waste to energy) plants. *Sci. Total Environ*. 420: 319-326.

Dahl, A., Gharibi, A., Swietlicki, E., Gudmundsson, A., et al. (2006). Traffic-generated emissions of ultrafine particles from pavement-tire interface. *Atmos. Environ*. 40: 1314-1323.

Dall'Osto, M., Booth, M. J., Smith, W., Fisher, R., et al. (2008). A Study of the size distributions and the chemical characterization of airborne particles in the vicinity of a large integrated steelworks. *Aerosol Sci. Technol*. 42(12): 981–991.

Donaldson, K., Tran, L., Albert Jimenez, L. A., Duffin, R., et al. (2005). Combustion-derived nanoparticles: a review of their toxicology following inhalation exposure *Part. Fibre Toxicol.* 5: 553-560.

ELPI (2017). DEKATI Electrical Low Pressure Impactor (ELPI). Download from: http://www.dekati.com.

Fernández-Camacho, R., Rodríguez, S., Rosa, J., Campa, A. M. S., et al. (2012). Ultrafine particle and fine trace metal (As, Cd, Cu, Pb and Zn) pollution episodes induced by industrial emissions in Huelva, SW Spain. *Atmos. Environ*. 61: 507–517.

Fernandez-Espinosa, A. J., Rodriguez, M. T., Rosa, F. J. B. and Sanchez, J. C. J. (2001). Size distribution of metals in urban aerosols in Seville (Spain). *Atmos. Environ*. 35: 2595-2601.

Giorio, C., Tapparo, A., Scapellato, M. L., Carrieri, M., et al. (2013). Field comparison of a personal cascade impactor sampler, an optical particle counter and CEN-EU standard methods for PM_{10}, $PM_{2.5}$ and PM_1 measurement in urban environment. *J. Aerosol Sci*. 65: 111-120.

Graskow, B. R., Kittelson, D. B., Abdul-Khaleek, I. S., Ahmadi, M. R., et al. (1998). Characterization of Exhaust Particulate Emissions from a Spark Ignition Engine. Soc. Autom. Eng. Warrendale, PA, 980528.

Gustafsson, M., Blomqvist, G., Gudmundsson, A., Dahl, A., et al. (2008). Properties and toxicological effects of particles from the interaction between tyres, road pavement and winter traction material. *Sci. Total Environ*. 393: 226-240.

Harris, S. J. and Maricq, M. M. (2001). Signature size distributions for diesel and gasoline engine exhaust particulate matter. *J. Aerosol Sci*. 32: 749-764.

Hedmer, M., Ludvigsson, L., Isaxon, C., Nilsson, P. T., et al. (2015). Detection of Multi-walled Carbon Nanotubes and Carbon Nanodiscs on Workplace Surfaces at a Small-Scale Producer. *Ann. Occup. Hyg*. 59(7): 836-852.

Hinds, W. C. (1999). *Aerosol Technology: Properties, Behaviour and Measurement of Airborne Particles.* John Wiley & Sons, UK. pp. 483.

Horvath, H. (1994). Atmospheric aerosols, atmospheric optics visibility. *J. Aerosol Sci*. 25: S23-S24.

Johansson, C., Norman, M. and Gidhagen, L. (2007). Spatial and temporal variations of PM_{10} and particle number concentrations in urban air. *Environ. Monit. Assess*. 127: 477-487.

Keogh, D. U., Ferreira, L. and Morawska, L. (2009). Development of a particle number and particle mass vehicle emissions inventory for an urban fleet. *Environ. Mod. Software*. 24: 1323-1331.

Kero, I., Naess, M. K. and Tranell, G. (2015). Particle Size Distributions of Particulate Emissions from the Ferroalloy Industry Evaluated by Electrical Low Pressure Impactor (ELPI). *J. Occup. Environ. Hyg*. 12: 37–44.

Kittelson, D. B. (1998). Engines and nano-particles: a review. *J. Aerosol Sci*. 29: 575-588.

Kulmala, M., Vehkamaki, H., Petaja, T., Dal Maso, M., et al. (2004). Formation and growth rates of ultrafine particles: a review of observations. *J. Aerosol Sci*. 35: 143-176.

Kumar, P., Robins, A., Vardoulakis, S. and Britter, R. (2010). A review of the characteristics of nanoparticles in the urban atmosphere and the prospects for developing regulatory controls. *Atmos. Environ.* 44: 5035–5052.

Kumar, P., Robins, A., Vardoulakis, S. and Quincey, P. (2011). Technical challenges in tackling regulatory concerns for urban atmospheric nanoparticles. *Particuology*. 9: 566-571.

Licen, S., Tolloi, A., Barbieri, G., Fabbris, A., et al. (2016). Ambient PM_{10} Concentration Reconstruction in an Inhabited Area Close to an Industrial Hot Spot by Using Particle Density and Optical Particle Counting Values. *JSM Environ. Sci. Ecol*. 4(1): 1026.

Lingard, J. J. N., Agus, E. L., Young, D. T., Andrews, G. E., et al. (2006). Observations of urban airborne particle number concentrations during rush-hour conditions: analysis

of the number based size distributions and modal parameters. *J. Environ. Monit*. 8: 1203-1218.

Malandrino, M., Casazza, M., Abollino, O., Minero, C. and Maurino, V. (2016). Size resolved metal distribution in the PM matter of the city of Turin (Italy). *Chemosphere*. 147: 477-489.

Manoli, E., Voutsa, D. and Samara, C. (2002). Chemical characterization and source identification/apportionment of fine and coarse air particles in Thessaloniki, Greece. *Atmos. Environ*. 36: 949-961.

Marconi, A., Cattani, G., Cusano, M. C., Ferdinandi, M., et al. (2007). Two years fine and ultrafine particles measurements in Rome, Italy. *J. Toxicol. Environ. Health A*. 70: 213–221.

Marple, V. A, Rubow, K. L. and Behm, S. M. (1991). A Microorifice Uniform Deposit Impactor (MOUDI): Description, Calibration, and Use. *Aerosol Sci. Technol*. 14(4): 434-446.

Mbengue, S., Alleman, L. Y. and Flament, P. (2014). Size-distributed metallic elements in submicronic and ultrafine atmospheric particles from urban and industrial areas in northern France. *Atmos. Res*. 135-136: 35-47.

Misra, C., Singh, M., Shen, S. Sioutas, C., et al. (2002). Development and evaluation of a personal cascade impactor sampler (PCIS*). J. Aerosol Sci.* 33(7): 1027-1047.

Mohiuddin, K., Strezov, V., Nelson, P. F., Stelcer, E., et al. (2014). Mass and elemental distributions of atmospheric particles nearby blast furnace and electric arc furnace operated industrial areas in Australia*. Sci. Total Environ*. 487: 323-334.

Morawska, L., Ristovski, Z., Jayaratne, R., Keogh, D. U., et al. (2008). Ambient nano and ultrafine particles from motor vehicle emissions: characteristics, ambient processing and implications on human exposure. *Atmos. Environ*. 42(35): 8113-8138.

Moroni, B. and Viti, C. (2009). Grain size, chemistry, and structure of fine and ultrafine particles in stainless steel welding fumes. *Aerosol Sci.* 40: 938 – 949.

Oberdorster, G. (2001). Pulmonary effects of inhaled ultrafine particles. *Int. Arch. Occup. Environ. Health*. 74:1–8.

Pey, J., Querol, X., Alastuey, A., Rodríguez, S., et al. (2009). Source apportionment of urban fine and ultrafine particle number concentration in a Western Mediterranean City. *Atmos. Environ*. 43: 4407-4415.

Reche, C., Querol, X., Alastuet, A., Viana, M., et al. (2011). New considerations for PM, Black Carbon and particle number concentration for air quality monitoring across different European cities. *Atmos. Chem. Phys*. 11: 6207-6227.

Riffault, V., Arndt, J., Marris, H. (2015). Fine and ultrafine particles in the vicinity of industrial activities: A review. *Crit. Rev. Environ. Sci. Technol.* 45(21): 2305-2356.

Saffari, A., Daher, N., Shafer, M. M., Schauer J. J., et al. (2013). Seasonal and spatial variation of trace elements and metals in quasi-ultrafine ($PM_{0.25}$) particles in the Los

Angeles Metropolitan area and characterization of their sources. *Environ. Pollut*. 181: 14-23.

Sanderson, P., Delgado-Saborit, J. M. and Harrison, R. M. (2014). A review of chemical and physical characterisation of atmospheric metallic nanoparticles. *Atmos. Environ.* 94: 353–365.

Shi, J. P., Evans, D. E., Khan, A. A. and Harrison, R. M. (2001). Sources and concentration of nanoparticles (<10 nm diameter) in the urban atmosphere. *Atmos. Environ*. 35: 1193-1202.

Strawa, A. W., Kirchstetter, T. W., Hallar, A. G., Ban-Weiss, G. A., et al. (2010). Optical and physical properties of primary on-road vehicle particle emissions and their implications for climate change. *J. Aerosol Sci*. 41: 36-50.

Tolocka, M. P., Lake, D. A., Johnston, M. V. and Wexler, A. S. (2005). Size-resolved fine and ultrafine particle composition in Baltimore, Maryland. *J. Geophys. Res. Atmos*. 110: D07-S04.

Vecchi, R., Chiari, M., D'Alessandro, A., Fermo, P., et al. (2008). A mass closure and PMF source apportionment study on the submicron sized aerosol fraction at urban sites in Italy. *Atmos. Environ*. 42; 2240-2253.

Wehner, B., Uhrner, U., von Löwis, S., Zallinger, M., et al. (2009). Aerosol number size distributions within the exhaust plume of a diesel and a gasoline passenger car under on-road conditions and determination of emission factors. *Atm. Environ*. 43: 1235-1245.

WHO. (2013). *Review of evidence on health aspects of air pollution– REVIHAAP. Project*. World Health Organization, Regional Office for Europe.

SECTION 3

Dermal and meningeal absorption of metal oxides nanoparticles

In Section 1 aluminium-containing ultrafine particles were found both airborne and deposited on working surfaces in two factories committed in the manufacturing of aluminium-based products.

In the same section it has been reported that the most representative particles emitted by GTAW of steel had a mean diameter of 47 nm and were mainly constituted by iron/manganese oxide, followed by smaller iron oxide nanoparticles (21 nm on average).

Ultrafine particles containing Fe and Mn were also observed in the study about the characterisation of airborne particles in proximity of an integrated steel plant presented in Section 2.

Stating that in all these studies a possible source of exposure to UFPs was identified, portal of entry in human body should be investigated.

Inhalation may be the major route of exposure for NPs, but dermal exposures need to be considered as well.

In the past years several studies about dermal permeation of metal and/or metal oxides nanoparticles were performed in our research group. For example, palladium and nickel NPs permeation through human skin was recently evaluated (Larese Filon et al., 2016; Crosera et al., 2016).

Starting from this background nanoparticles with characteristics compatible with those found in the studies presented in the previous sections of this thesis were tested *in vitro*.

Transdermal absorption of Al_2O_3 nanoparticles is evaluated in the first part of this section. The results of this work have been submitted to *Toxicology in Vitro*.

The aim of the second study presented in this section is to clarify the possible role of meningeal membranes in the mechanisms of absorption of metal oxides NPs through the olfactory route. Porcine meninges were used in an *in vitro* study given their high histological similarities with human ones. The results of this work have been submitted to *Chemico-Biological Interaction*.

1. In vitro transdermal absorption of Al_2O_3 nanoparticles

1.1 Introduction

Aluminium oxide (Al_2O_3) is commonly used in manufacturing production of abrasives, refractories materials, ceramics, electrical insulators, catalysts, paper, spark plugs, light bulbs, alloys, glass and heat resistant fibres (Krewski et al., 2007). It has been estimated that working population can be exposed to aluminum (Al) up to three times higher if compared with the general population (ACGIH, 1987; Stokinger, 1981; Van Oostdam et al., 1990), but data are lacking as regards exposure to nano Al, which use keeps growing Najafpour et al., 2012; Patra et al., 2012; Stadler et al., 2010; Monteiro-Riviere et al., 2010; Li et al., 2011).

Concern is supported by the fact that nanoparticles (NPs) may behave in a different way if compared with their homologous bulk material, due to their high surface/volume ratio, which confers different surface chemical properties (Royal Society & Royal Academy of Engineering, 2004), and therefore different toxicological potential after interaction with biological media.

Conflicting opinions are present in literature over whether nanoscale alumina presents health risks. The most investigated effects are cell viability and DNA damage. Some authors demonstrated Al_2O_3NPs cytotoxicity and genotoxicity on different cell lines (Zhang et al., 2011; Park et al., 2017; Srikanth et al., 2015: Alshatwi et al., 2012; Rajeshwari et al., 2015; Hashimoto et al., 2015; Di Virgilio et al., 2010), while others found minimal to non-existing cyto- and genotoxic effects (Ivask et al., 2015; Demir et

al., 2013; Canli et al., 2017; Rajiv et al., 2016; Sadiq et al., 2014; Razdium et al., 2011; Balasubramanyam et al., 2010; Kim et al., 2010; Tsaousi et al., 2010). Zhang and coworkers (2017) showed a higher genotoxicity of these NPs with respect to bulk alumina and Mirshafa and colleagues (2017) showed a size-dependent neurotoxicity of Al_2O_3, which seems to increase as particles size decrease, reaching highest effects in nano-size range. Al is a trace element in the human organism (Krizek et al., 1997), but Al overload can be dangerous for human health. The main health issues relate to Al exposure are (i) the possible onset of neurodegenerative diseases after chronic Al exposure, such as Alzheimer dementia (McDowell et al., 2001; Tomljenovic et al., 2011; Campdelacreu et al., 2012; Killin et al., 2016) and (ii) the onset of occupational contact dermatitis (Hall, 1944; Purello-D'Ambrosio et al., 2000) and irritant dermatitis (Johannessen et al., 1980), which have been reported among workers exposed to Al alloys and Al dust (Krewski et al., 2007). The issue of a possible linking of breast cancer to the use of underarm antiperspirant or deodorant products containing Al has been arised by some authors (Darbre, 2005), but the scientific community thoroughly debated this point and stated there is no plausible evidence regarding humans (CIR, 2014).

Almost all available *in vitro* studies on Al were performed using animal (Putterman et al., 1981) or human skin (Blank et al., 1958) exposed to Al chlorohydrate (ACH) and found that the metal slightly penetrates the skin. Al forms complexes with skin proteins (Hostynek et al., 1993) and the greatest amount of the metal can ultimately be found in the sweat ducts (Quatrale et al., 1981) and in the stratum corneum. On the other hand, *in vivo* studies showed that after Al dermal application a statistically significant increase of the metal was detectable in urine and serum of exposed animals (Anane et al., 1995), while in humans an excretion of 0.012% was detectable in the urine after underarm single

antiperspirants-containing-Al application (Flarend et al., 2001), meaning that a small absorption through skin happened. Pineau and colleagues (2012) confirmed this data by means of an *in vitro* study using Al salts - derived from different commercial antiperspirants formulations - applied on human excised skin biopsies mounted on Franz diffusion cells. The results showed that Al concentrations in the receptor fluid corresponded to only 0.012% of the applied Al, while Al amount in stripped skin was significantly higher. But also a case report of systemic hyperaluminemia (plasma Al = 104.7 μg L^{-1}) presenting with complaints of bone pain after 4 years of daily ACH deodorant application has been described (Guillard et al., 2004).

Data on Al and Al oxide nanoparticles skin penetration and permeation are currently lacking and the aim of the present study was to assess this issue (Larese Filon et al., 2015), investigating the transdermal absorption of Al_2O_3NPs through intact and damaged human skin using an *in vitro* method (Mauro et al., 2015; Larese Filon et al., 2016).

1.2 Materials and methods

1.2.1 Chemicals

All chemicals were analytical grade. Urea, sodium chloride, sodium hydrogenphosphate, potassium dihydrogenphosphate, were purchased from Carlo Erba (Milan, Italy); lactic acid (90% w/w) was bought from Acros Organics (Geel, Belgium); nitric acid (69% w/w), hydrogen peroxide (30% w/w), ammonium hydroxide (25% w/w), boric acid, hydrochloric acid (37% w/w) and hydrofluoric acid (48% w/w) from Sigma Aldrich (Milan, Italy). Water reagent grade (milliQ water) was produced with a Millipore purification pack system.

The commercially available dispersion of aluminium oxide (Al_2O_3) nanoparticles (30-60 nm) was provided by Sigma Aldrich (Milan, Italy). The nanoparticle concentration was 20 wt % in water.

1.2.2 Nanoparticles characterisation

Al_2O_3NPs have been visualized, once they were dispersed in synthetic sweat and at the end of the experiments (after a 24 h exposure time) to confirm the dimensions of the NPs and the aggregation state of the donor phase, by Transmission Electron Microscope (EM208; Philips, Heidhoven, The Netherlands) with a high definition acquisition system SIS Quemesa (Olympus Soft Imaging Solutions) and a digital image acquisition system iTEM (FEI Italia, Milan, Italy).

1.2.3 Nanoparticles dissolution

In order to evaluate the ions release from NPs once they were put in synthetic sweat, 4 mL of the donor phase (the Al_2O_3NPs dispersion diluted ten times with synthetic sweat), have been ultrafiltered using Amicon Ultra-4 centrifugal filters (10K MWCO) supplied by Millipore Corporation (USA). The ultrafiltration has been performed in centrifuge at 5000 rpm for 30 min in order to remove the Al_2O_3NPs, but not aluminium ions, from the solution (Crosera et al., 2016).

The solution has been analysed by means of ICP-AES (Inductively Coupled Plasma-Atomic Emission Spectroscopy) to quantify the aluminium concentration. This operation has been repeated on three different aliquots of donor solution.

1.2.4 Preparation of skin membranes

Human abdominal full thickness skin was obtained as surgical waste from 2 female patients aged 45–65 years, after having obtained ethical committee approval. After the skin excision subcutaneous fat has been removed with a scalpel blade and hair was shaved from the epidermis, then skin samples were stored at −25 °C for a period up to, but not exceeding, 4 months. It has been demonstrated that this procedure does not damage skin barrier properties. On the day of the experiment skin samples were defrosted in physiological solution at room temperature for a 30 minutes period and then 4 × 4 cm^2 pieces were cut from each skin specimen and mounted separately on the diffusion cells. Thickness of the membranes were < 1mm.

Skin integrity was tested before and after each experiment using electrical conductivity by means of a conductometer (Metrohm, 660, Metrohm AG Oberdorfstr. 68 CH-9100 Herisau) operating at 300 Hz and connected to two stainless steel electrodes. The conductibility data in μS were converted into KΩ cm^{-2}. Cells with a resistance lower than 3.95 ± 0.27 KΩ cm^{-2} were considered to be damaged and rejected, as suggested by Davies et al. (2004).

1.2.5 *In vitro* diffusion system

Percutaneous absorption studies were performed using static diffusion cells following the Franz method (Franz, 1975). The receptor compartment had a mean volume of 14.0 mL and was maintained at 32 °C by means of circulation of thermostated water in the jacket surrounding the cell. This temperature value was chosen in order to reproduce the hand physiological temperature at normal conditions. The physiological solution used as the

receptor phase was prepared by dissolving 2.38 g of Na_2HPO_4, 0.19 g of KH_2PO_4 and 9 g of NaCl into 1 L of milliQ water (final pH 7.35). The synthetic sweat solution used as donor fluid consisted in 0.5% sodium chloride, 0.1% urea and 0.1% lactic acid in milliQ water; pH 4.5 was adjusted with ammonia.

The salt concentration in the receiving fluid was approximately the same that can be found in blood. The physiological solution used as receiving phase was continuously stirred using a Teflon coated magnetic stirrer. Each piece of skin was clamped between the donor and the receptor compartment; the mean exposed skin area was 3.29 cm^2 and the average membranes thickness was 1 mm. Two different experiments were conducted using intact (exp. 1) and damaged skin (exp. 2) as described below.

1.2.5.1 Experiment 1

The donor solution was prepared just before the experiment, diluting the Al_2O_3NPs dispersion ten times with synthetic sweat (final concentration of 20 g L^{-1}). The aluminium concentration in the donor phase was confirmed by ICP-AES analysis: the Al_2O_3NPs were dissolved by addition of 1 mL of hydrofluoric acid (48% w/w). After the addition of 6 mL of boric acid, the solution was diluted to 50 mL with milliQ water.

At time 0, the exposure chambers of six Franz diffusion cells were mounted with intact skin samples and filled with 1 mL of the donor suspension (6.06 mg cm^{-2}) to ensure an infinite dose. The experiment was run for 24 h, when the receiving and the donor phases of each diffusion cell were recovered for analysis.

1.2.5.2. Experiment 2

Experiment 1 was repeated in parallel using an abraded skin protocol as suggested by Bronaugh and Steward (1985): skin was abraded by drawing the point of a 19-gauge hypodermic needle across the surface (20 marks in one direction and 20 perpendiculars).

1.2.5.3. Blanks

For each experiment, two cells were added as blank. The blank cells were treated as the other cells with the exception that only synthetic sweat was used in the donor compartment.

1.2.5.4. Skin digestion after the experiment

After the experiment the skin pieces were washed three times with physiological solution to remove residual Al_2O_3NPs from the skin surface, then removed from the diffusion cells and separated into epidermis and dermis by heat shock, immerging in water at 60 °C for 1 min before freezing at −25 °C. At the time of the analysis, the skin membranes were dried for 2 h at room temperature, weighed and acid-digested in a closed microwave system (Multiwave PRO, Anton Paar) using a mixture of 4 mL of HNO_3 (69 %) and 0.5 mL of HF (48%). The mineralization was performed through two heating steps. In the second step H_3BO_3 was added in order to buffer the excess of HF. The solutions obtained from the mineralization process were diluted up to a volume of 15 mL by adding Milli-Q water before ICP-AES analysis.

1.2.6. Analytical measurements

An Inductively Coupled Plasma Mass Spectrometer (ICP-MS) 7500 CE Agilent Technologies Inc., Santa Clara, CA, USA instrument (with integrated autosampler) was used to determinate the total aluminum concentration in the receiver phases.

A six-points standard curve, obtained by dilution of aluminium standard solution for ICP-MS analyses (by Merck, Germany) was used for ICP-MS measurements (0.1, 0.5, 1, 5, 10, and 100 μg L^{-1}, ion mass 27 u.m.a.). The limit of detection of aluminum was 0.1 μg L^{-1} for ICP-MS and the precision of the measurements as repeatability (RSD %) for the analysis was always <5%. Total aluminium concentration in the donor phases and in the solutions resulting from the mineralization of the skin samples was determined by ICP-AES using an Optima 8000 Spectrometer (PerkinElmer, U.S.A.), equipped with an S10 Autosampler. Analyses were conducted using a calibration curve obtained by dilution (range: 0 - 10 mg L^{-1}) of aluminium standard solution for ICP-AES analyses (by Sigma Aldrich, Milan, Italy). The limit of detection (LOD) at the operative wavelength of 396.153 nm was 0.01 mg L^{-1}.

The precision of the measurements expressed as relative standard deviation (RSD %) for the analysis was always less than 5%.

1.2.7. Statistical analysis

Aluminium concentration data (μg cm^{-3}) in the receptor solution were converted to the total amount that penetrated (μg cm^{-2}), with a correction for dilution due to sample removal.

Data analysis was performed with Excel for Windows, release 2007 and Stata Software, version 11.0 (StataCorp LP, College Station, TX, USA). Skin absorption data were reported as mean ± standard deviation (SD). The difference among independent data was assessed by means of the Mann-Whitney test. A p value <0.05 was considered significant.

1.3. Results

1.3.1 Nanoparticles characterisation

Representative TEM images of Al_2O_3NPs suspension, diluted in synthetic sweat, before and after the experiments, and their size distribution, are presented in Fig. 3.1.1 (a, b, c, respectively). The mean size of the NPs was 53 ± 15 nm in accordance with the declared dimension (number of NP measured = 100), but tended to form bigger aggregates reaching the micrometer range. Aggregation was similar before and after experiments. NPs were stable in synthetic sweat and results derived from the ultrafiltration of the NPs suspension showed that the aluminium concentration was always less than 0.1% of the original NPs dispersion**.**

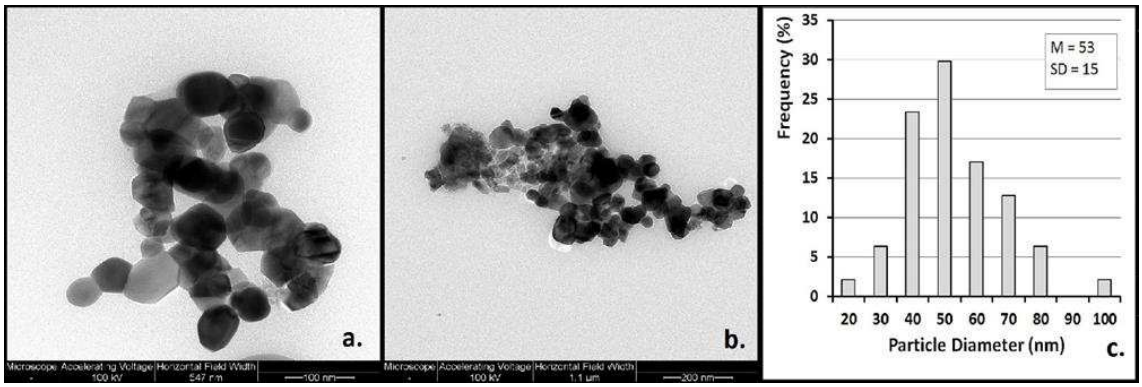

Figure 3.1.1 Representative TEM images of Al_2O_3NPs (a, b) and NPs size distribution (c). Note: Scale bar (a) 100 nm, (b) 200 nm.

1.3.2 Franz diffusion cells experiments

After 24 hours of exposure only traces of Al were detectable in the receiving solution of cells exposed to NPs (35.1 ± 6.1 ng cm^{-2} for intact and 88.5 ± 34.2 ng cm^{-2} for damaged skin, results expressed as mean and SD) and in blank cells too (36.3 ± 7.0 ng cm^{-2}). The difference between damaged skin samples exposed to NPs and blanks did not reach statistical significance (p = 0.08, Mann-Whitney test), meaning that the average amount of the metal found could be present as impurity (Fig. 3.1.2).

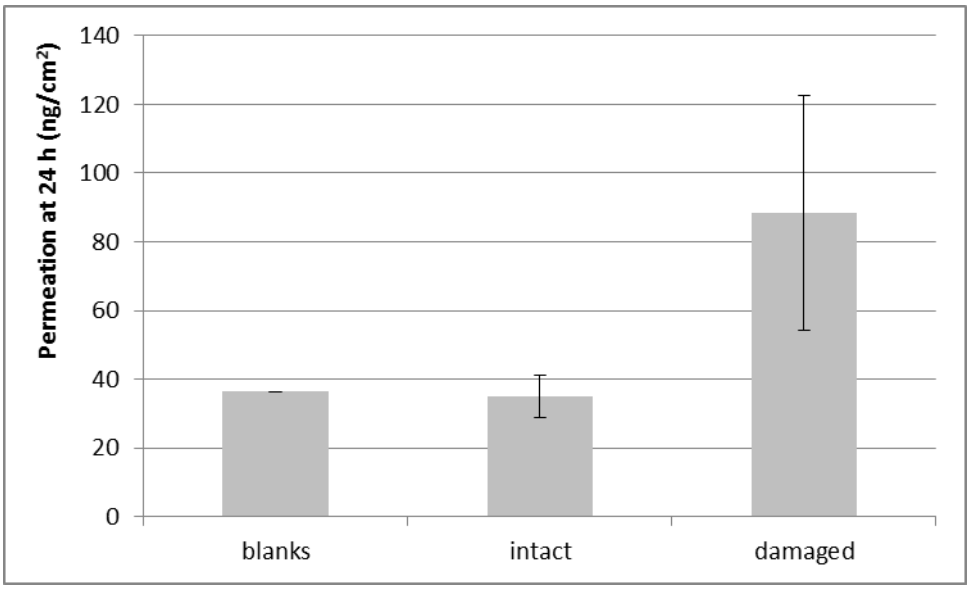

Figure 3.1.2 Aluminium content (ng cm^{-2}) in receiving solutions of cells exposed to Al_2O_3NPs (intact skin and damaged skin) and in cells exposed to physiological solution (blanks). Mean and standard deviation of 6 cells each for NPs and 4 cells for blanks.

The average amount of Al in intact and damaged whole thickness skin samples was 3.96 ± 0.21 µg cm^{-2} and 4.36 ± 0.48 µg cm^{-2}, respectively (p = 0.08). Al content was similar in epidermal and dermal layers of both intact and damaged skin samples (1.95 ± 0.13 µg cm^{-2} and 2.31 ± 0.12 µg cm^{-2} for epidermal layer, 2.01 ± 0.25 µg cm^{-2} and 2.05 ± 0.35 µg

cm^{-2} for dermal layer). Al penetration in blank cells was 2.16 µg cm^{-2} (1.70 for epidermal layer and 0.46 µg cm^{-2} for dermal layer) (Fig. 3.1.3).

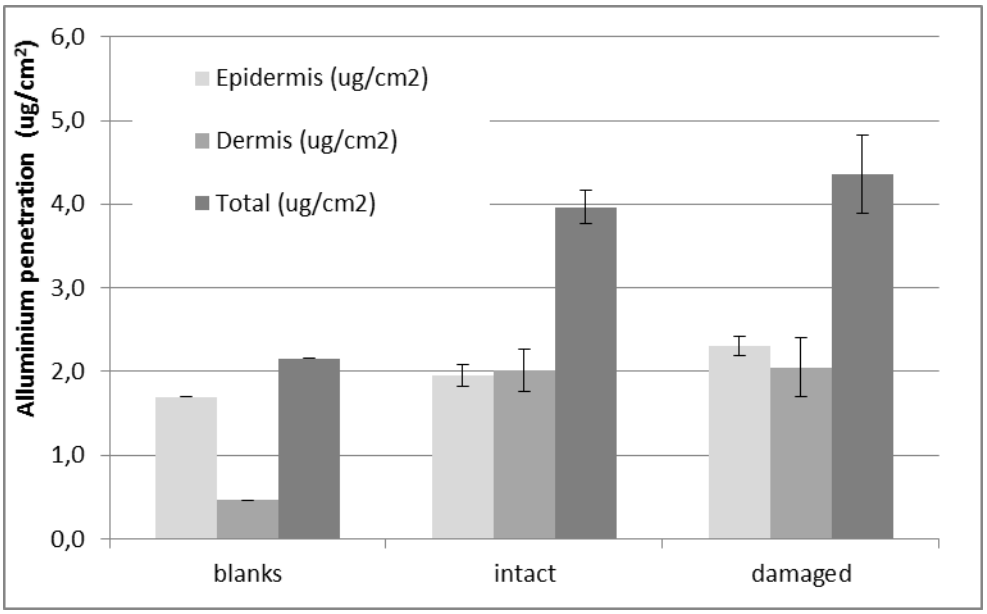

Figure 3.1.3 Aluminium content (µg cm^{-2}) inside the skin (whole thickness, epidermis, dermis) of blank cells (exposed to physiological solution), intact skin and damaged skin (exposed to Al_2O_3NPs). Mean and standard deviation of 6 cells each for NPs and 4 cells for blanks.

The two donors specific values of penetration and permeation through intact and damaged skin samples are shown in Table 3.1.1.

Donor	Penetration (ug/cm²)				Permeation (ng/cm²)			
	Intact	(mean ± SD)	Damaged	(mean ± SD)	Intact	(mean ± SD)	Damaged	(mean ± SD)
#1	4,14		4,75		30,90		98,30	
	3,91	3,95 ± 0,17	4,51	4,35 ± 0,50	43,20	35,25 ± 6,90	38,70	64,60 ± 30,56
	3,80		3,79		31,65		56,80	
#2	3,64		4,82		30,75		116,30	
	4,03	3,96 ± 0,29	3,73	4,38 ± 0,57	42,57	34,87 ± 6,67	93,98	112,39 ± 16,80
	4,21		4,58		31,30		126,90	
Total		3,96 ± 0,21		4,36 ± 0,48		35,06 ± 6,07		88,5 ± 34,23

Table 3.1.1 Donor specific values of penetration and permeation through intact and damaged skin samples as mean and SD.

1.4 Discussion and conclusions

Dermal exposure to Al can occur in some occupational scenarios, as seen in section 2 of this thesis, and also using personal care products (PCP).

Al micro- and nano-powders (diameter in the range of 10-300 nm) can be intentionally added in the production of automobile paints (Hong and Kim, 2002), as fuel additives in propellants, explosives and pyrotechnics (Dinman, 1987; Meda et al., 2004; Trunov et al., 2005), or can represent a waste product in some occupational activities such as friction stir, flame, and solid-state welding on Al (Curwin and Bertke, 2011; Dasch and D'Arcy, 2008; Gomes et al., 2012a; Gomes et al., 2012b; Pfefferkorn et al., 2010), sanding painted surfaces (Koponen et al., 2010) and in electric arc thermal sprays (Bémer et al., 2010).

Al can be found in PCP in the form of salts, mostly as ACH, because its capacity to block secretion of sweat is exploited (Quartrale, 1988).

Experimental data on Al dermal absorption are limited and all of them investigated the behavior of Al salts, while actually no data at all exist as regard to transdermal permeation of Al and Al oxides nanoparticles.

Our study investigated *in vitro* on human excised skin samples - intact and damaged - the permeation of 30-60 nm Al_2O_3NPs and results showed that the average Al amount found in the receiver chambers of exposed cells was very low and similar to the one found in blank cells. This result can be justified by the fact that Al is a trace element in human body and a small background level of Al is expected to be found in receiving solution, although this does not mean that in cells exposed to Al_2O_3NPs a metal permeation through skin did occur.

This is in line with results of Putterman and colleagues (1981), who investigated *in vitro* on guinea pigs stratum corneum the absorption and desorption of Al chloride and Al chlorohydrate solutions. Moreover, their results showed that the desorption of Al chlorohydrate is lower if compared with Al chloride, which means that this species is retained inside the outer skin layer for a longer time. Blank and colleagues (1958) investigated *in vitro* on human excised skin a 23h exposure to 20% Al chlorohydrate solution by means of tape stripping and found that very little Al reached the dermis. They hypothesized a possible strong binding of Al complexes to the outer stratum corneum layers.

In vivo studies on humans and animals showed different results between acute and chronic exposure. Lansdown and coauthors (1973) investigated *in vivo* on animals a 5 consecutive days dermal exposure to six different Al salts (aluminum chloride 10%, nitrate 10%, sulphate 10%, hydroxide 10%, acetate 10% and chlorhydrate 10% and 25%) and found different kind of inflammatory skin reactions only for exposure to Al chloride and nitrate, but no data on transdermal absorption were collected. Anane and colleagues (1995) investigated *in vivo* on mice chronic exposure (130 days) to Al chloride. The Al amount tested was similar to the one expected in a one day antiperspirants use. Results showed a significant increase of Al content in urine and serum of treated mice, meaning that a small fraction of topical antiperspirants might produce measurable increase in urine and tissue Al levels. Reassuring results were instead provided by Flarend and colleagues (2001), who investigated *in vivo* on two volunteers (underarm) the absorption of a single radiolabeled Al chlorohydrate (^{26}Al) exposure by means of blood and urine samples collection for 7 weeks. Results indicated that only 0.012% of the applied Al was absorbed through the skin, which is about 2.5% of the Al typically absorbed by the gut from food

over the same time period. The same Al transdermal permeation percentage was confirmed *in vitro* by Pineau and colleagues (2012), who investigated the permeation of Al salts contained within commercial antiperspirants through excised human skin using Franz cells apparatus.

Comparing our results with the latter cited study (Pineau et al., 2012), we found a percentage of metal permeated through the skin after 24 hours approximately five orders of magnitude lower using intact skin and approximately four orders of magnitude lower using damaged skin. This could be due to different reasons, the most important of which is the different dissolution potential in biological media. Al salts are by definition water soluble, while our results showed an Al_2O_3NPs dissolution value in donor solution lower than 0.1%. This is in line with other metal oxides NPs (Crosera et al., 2015; Mauro et al., 2015). This different behavior reflects and justifies different uses of these substances. Al salts are the main ingredient inside antiperspirants, since they can form hydroxide precipitates of denatured keratin in the cornified layer that surrounds and occludes the opening of sweat ducts, leading to a sweating reduction (Quartrale, 1988). On the other hand Al oxide NPs do not show this feature and are not commonly used in PCP products, but may originate as waste product of industrial processes, and therefore come in contact with the skin of workers employed in manufacturing processes. Moreover, the Al_2O_3NPs tested were quite big in size (30-60 nm) and hence even the possibility of their passage through the damaged skin samples is actually unlikely (Larese et al., 2015). It could be interesting to compare Al_2O_3NPs permeation results with the ones obtained in previous studies conducted using other metal oxide NPs such as Co_3O_4NPs and TiO_2NPs using similar experimental protocol (Crosera et al., 2015; Mauro et al., 2015). Both Al_2O_3NPs and Co_3O_4NPs slightly permeate the skin, reaching fully comparable final values through

damaged skin, while permeation through damaged skin was slightly higher for Al_2O_3NPs, but still in the same order of magnitude of ng cm^{-2}. Instead TiO_2NPs do not permeate and only barely penetrate the skin.

Therefore, although with the limitations due to the *in vitro* test procedure - which cannot take into account any active uptake mechanism - our study supports the hypothesis of a reassuring permeation profile as regards transdermal permeation of Al_2O_3NPs, which may be generated in different working scenarios.

2. In vitro meningeal permeation of $MnFe_2O_4$ nanoparticles

2.1 Introduction

The wide production and use of nanomaterials occurred in recent decades motivates the interest of the scientific community investigating possible unknown nano-toxicological effects. Nanoparticles, indeed, are expected to exert more severe health effects than bulk counterparts (Colvin, 2003) given their higher surface area to volume ratio (Kreyling et al., 2006; Oberdorster, 2001), which means that a greater interaction with biological matrices could take place after all routes of exposure.

Manganese nanoparticles (MnNPs) could easily come in contact with human bodies either when intentionally produced (engineered NPs) or as a by-products of other manufacturing processes. In the first case, MnNPs can be found in the wastewater treatment, in catalysis processes, in batteries, sensors and supercapacitors production (Ma et al., 2004; Cheng et al., 2006; Cao et al., 2011). In the second case, as reported in Section 1 and 2 of this thesis, Mn-containing NPs can be found in arc-welding fumes, in ferroalloy metallurgy workplaces, iron and steel foundries and also as components of combustion emissions of power plant and coke oven. In all the aforementioned scenarios, the main exposure for workers is through inhalation pathway (Flynn and Susi, 2009; Stefanescu et al., 2009).

While lung absorption has been quite extensively studied, very little is known regarding a possible absorption through the olfactory route, which may take place after NPs mucosal deposition in the upper airways (Oberdorster et al. 2009).

The central nervous system (CNS) has a direct connection with the external environment through the olfactory nerves. Throughout this route, from the upper portion of the nasal cavity to the olfactory bulb, passing through the ethmoidal cribriform lamina, the bundles of the olfactory nerve are enveloped by the meninges, whose permeation properties are unknown.

Magnetite NPs that are combustion derived pollutants often associated with other transition metal particles were found in human brain (Maher et al., 2016) but the uptake mechanism is still unknown.

The mechanism of uptake and transport of metals into the olfactory system has been studied for different particles (Tjalve and Henriksson, 1999; Rao et al., 2003) and Mn was found to be taken up preferentially via the olfactory pathway.

In physiological conditions manganese is a cofactor for several enzymes required in neuronal and glial cell function (Butterworth, 1986; Erikson and Aschner, 2003), but an overexposure to this metal may cause a bioaccumulation in the caudate nucleus and hippocampus (Katsnelson et al., 2015). This leads to a progressive and permanent neuro-degenerative damage of the dopaminergic neurons, symptoms of which resemble Parkinson's disease (Erikson and Aschner, 2003; Quintanar, 2008). The affected workers develop fatigue, headache, muscle cramps, loss of appetite, apathy, dystonia, hypokinesia, rigidity, and muscle tremors (Pal et al., 1999; Bowler et al., 2006; Ellingsen et al., 2008; Flynn and Susi, 2009; Bowler et al., 2011), which altogether define a condition called "manganism" (Ingersoll et al., 1999; Cerosimo and Koller, 2006; Aschner et al., 2007; Ordonez-Librado et al., 2008; Katsnelson et al., 2015). The same symptoms have been described in rats exposed to MnO_2 NPs (Li et al., 2014).

The aim of the present study was to assess the permeability properties of meningeal membranes, currently undefined, towards $MnFe_2O_4$NPs, which represent a common by products in the arc-welding fumes (Andujar et al., 2014) and may exert chronic neurotoxic effects on humans. Experimental data are actually lacking and results may increase the knowledge in the field of occupational health and safety.

2.2 Material and methods

2.2.1 Chemicals

All chemicals used were of analytical grade. Sodium chloride, sodium hydrogen phosphate, potassium dihydrogen phosphate, hydrogen peroxide (30% w/w), and nitric acid (69% w/w) were purchased from Sigma Aldrich (Milan, Italy). Water reagent grade was produced with a Millipore purification pack system (milliQ water).

The physiological solution used as receptor fluid was prepared by dissolving 2.38 g of Na_2HPO_4, 0.19 g of KH_2PO_4 and 9 g of NaCl into 1 L of milliQ water (final pH = 7.35).

2.2.2 $MnFe_2O_4$ nanoparticles characterisation

Manganese ferrite nanopowder ($MnFe_2O_4$) used for the experiments was supplied by Sigma-Aldrich (Milano, IT), and was formed by 50 nm mean size nanoparticles, datum confirmed by Transmission Electron Microscopy (EM208; Philips, Eindhoven, The Netherlands, operating at 200 kV) analysis.

2.2.3 Donor phases preparation

Two different donor phases were prepared just before the experiments in order to distinguish the permeation of $MnFe_2O_4$NPs and that of Mn and Fe ions released from the

NPs. The first donor phase consisted of the $MnFe_2O_4$NPs dispersion, prepared using 100 mg of $MnFe_2O_4$ nanopowder dispersed by sonication in 50 ml of physiological solution (final concentration of 2.0 g L^{-1}).

The second donor phase was prepared by ultrafiltration of the first one, to obtain only the water-soluble species present in the first donor phase at the moment of the experiment. Four mL of the $MnFe_2O_4$NPs dispersion were ultrafiltered in centrifuge at 5000 rpm for 30 min by means of Amicon Ultra-4 centrifugal filters (with a molecular weight cut-off at 10 KDa) in order to separate the $MnFe_2O_4$NPs from the aqueous solution. The filtration has been repeated on five different aliquots that were mixed for a total of 20 mL in order to obtain an adequate solution volume to perform metals quantification analysis by means of Inductively Coupled Plasma Atomic Emission Spectrometry (ICP–AES) and the permeation experiments.

2.2.4 Preparation of meningeal membranes

Porcine meninges were used given their high histological similarities with human ones (Groenen et al., 2012; Amitrano and Tortora, 2012). The membranes were collected immediately after the slaughter of pigs up to 1 year old in a slaughterhouse in Trieste, IT. The tissue was excised from the ventral surface of the animal skull after the opening of the bone along the cranium caudal line. The membranes were detached from the underlying bone with surgical forceps. Two pieces of meninges (approximately 5 cm diameter) for each animal were obtained. The tissue was stored at 4°C during the transport to laboratory and then in freezer at −80°C for a period of time up to, but not exceeding, 1 week. On the day of the experiments tissues were removed from the freezer and soaked in physiological solution at room temperature for about 30 minutes before starting the

permeation experiments. The integrity of the membranes was tested before and after each experiment by filling the donor chamber with water MilliQ and by monitoring the presence of the solution in the receiving chamber for a period of 30 minutes (Lestari et al., 2009).

2.2.5 *In vitro* diffusion system

The method of static Franz diffusion cells (Franz, 1975) was used to study the meningeal permeation properties. The donor solutions were different in exp. 1 and 2, in order to evaluate whether permeation capability was different between NPs and their ultrafiltered solution, while the receiving phase was composed in both cases by warm physiological solution to reproduce the same conditions that can be found in the blood. In order to do this the receiver compartments were maintained at 37°C by means of circulation of thermostated water in the jacket surrounding the cells throughout the experiment and the receiving solution was kept stirred in each receiving cell using a Teflon coated magnetic stirrer.

The sheets of meninges were clamped between the donor and the receptor compartment placing the dura mater side facing the donor compartment, with a final mean exposed area of the meningeal membranes of 3.29 cm^2. Experiments were carried out for 4 h and conducted as follows:

Experiment 1: At time 0, the exposure chambers of 4 Franz diffusion cells were filled with 1.5 mL of $MnFe_2O_4$NPs suspension (0.91 mg cm^{-2}), corresponding to a concentration of 0.44 mg cm^{-2} of Fe e 0.22 mg cm^{-2} of Mn, in order to provide an infinite dose: the concentration in each cell was confirmed at the end of the experiments by means of ICP-AES analysis.

At selected intervals (20, 40, 60, 80, 100, 120, 180, 240 min) 1 mL of the receiving bathing solution was withdrawn and collected for the analysis, and immediately replaced with an equal volume of fresh made physiological solution. At the end of the experiment the meninges pieces were removed, washed three times with 3 mL of milli-Q water, and subsequently stored in the freezer at −25°C together with meningeal bathing solutions and the donor solutions for the following analysis.

Experiment 2: The exposure chambers of 4 Franz diffusion cells were filled with 1.5 mL of the ultrafiltered solution to verify differences between ions and nanoparticles permeation. The other test conditions were the same of the exp. 1.

Blanks: For each experiment two cells were added as blank. The experimental conditions were the same with the exception of the donor solution, which was composed only by physiological solution.

2.2.6 Meningeal digestion after the experiment

The meningeal membranes were cut into small pieces after being dried for 2 hours at room temperature and weighed. The sections were subsequently put into glass tubes with 10 mL of HNO_3 and 1.0 mL of H_2O_2 for digestion. The resulting solutions were heated at 80° C for 8 h and then a final volume of 10.0 mL was restored with MilliQ water. The analyses were performed by means of ICP-AES.

2.2.7 Quantitative analysis

An Inductive Coupled Plasma Mass Spectrometer NEXION 350D (Perkin Elmer; Waltham, MA, USA) with an integrated auto sampler, was used to determinate the total manganese and iron concentrations in the receiver phases (ion mass selected: 55 u.m.a.

for Mn and 54 and 57 u.m.a. for Fe). ^{103}Rh has been used as internal standard for all the samples. The analyses were carried out in kinetic energy discrimination (KED) mode using ultra-high purity helium (flow rate of 4.1 mL min^{-1}) to minimize polyatomic interferences.

A seven-point standard curve was used for ICP-MS measurements (range 0–100 µg L^{-1}). The limit of detection of iron and manganese was 0.5 µg L^{-1} for ICP-MS and the precision of the measurements expressed as repeatability (RSD %) was always lower than 5%.

The total iron and manganese concentrations in the donor phases and in the solutions resulting from the tissue mineralization were performed by ICP–AES using an Optima 8000 ICP-OES Spectrometer (PerkinElmer, USA) equipped with an S10 Autosampler (PerkinElmer, USA). The measurements were conducted using a calibration curve obtained by dilution of iron and manganese standard solutions for ICP–AES analysis (Sigma–Aldrich, Italy). The limit of detection at the operative wavelength of 238.204 nm for Fe and 257.610 nm for Mn was 0.010 mg L^{-1} for both metals. The precision of the measurements expressed as repeatability (RSD %) was always lower than 5%.

2.2.8 Data analysis

Data analysis was performed with Excel for Windows, release 2007 and Stata Software, version 11.0 (StataCorp LP, College Station, TX, USA). All data are reported using the mean as a measure of central tendency and the standard deviation (SD) as a measure of dispersion. The difference between independent data was assessed by means of the Mann-Whitney test. A p value of <0.05 was considered as the limit of statistical significance.

2.3. Results

2.3.1 Characterisation of $MnFe_2O_4$NPs suspension

TEM analysis performed on the donor solution, at the moment of the preparation, confirmed the average particle size of the NPs. After a 4 hours' exposure time, no modification of the dispersion was visible at the transmission electronic microscopy analysis. (Fig. 3.2.1)

The dissolution test of the nanopowder by ultrafiltration indicated that $MnFe_2O_4$NPs were very stable in physiological solution since the amount of Fe and Mn detected in the liquid derived from the ultrafiltration was lower than 0.1% of the starting nanopowder dispersion for both the elements, meaning that no significant ionisation of the metals occurred.

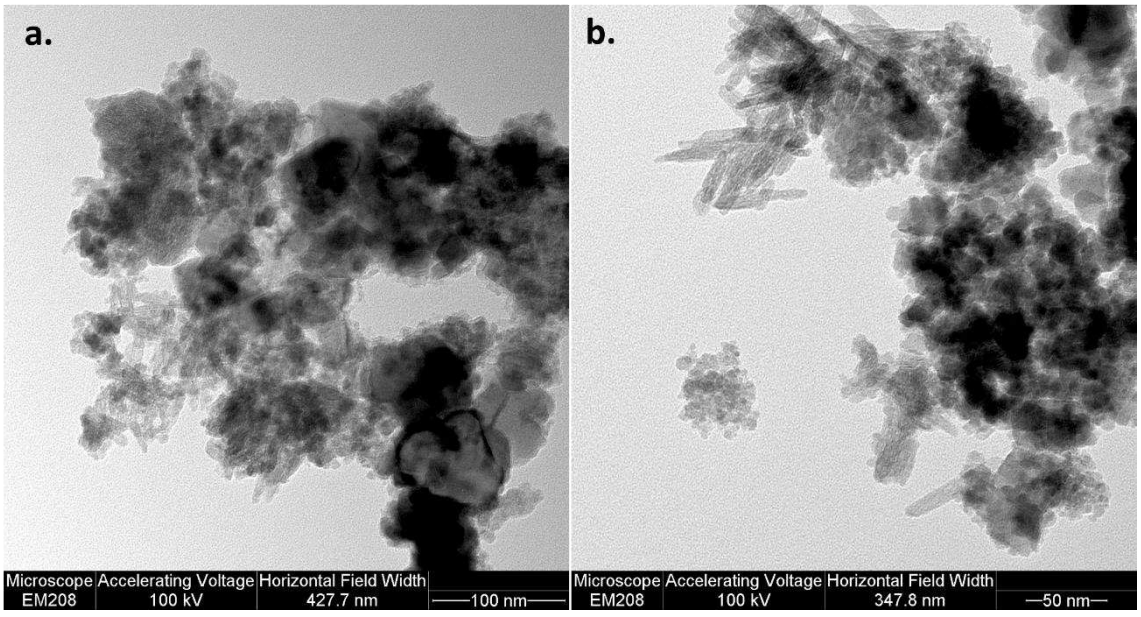

Figure 3.2.1 TEM images of the $MnFe_2O_4$NPs dispersed in physiological solution before (a) and after a 4 hours' exposure (b): NPs had mean diameter of 50 nm, appeared not uniform in shape and tend to form aggregates (a: bar=100nm; b: bar=50nm).

2.3.2 Metals permeation through meningeal membrane

Mn and Fe have been detected only in small traces in the receiving solutions of both experiments (exp. 1 and 2), meaning that a significant permeation of the metals did not occur.

Mn concentrations at 4 hours were 5.5 ± 4.4 ng cm^{-2}, 3.5 ± 3.2 ng cm^{-2}, 2.1 ± 1.2 ngcm^{-2} (mean and SD) in cells exposed to $MnFe_2O_4$NPs, to ultrafiltered solution, and blank cells (Fig. 3.2.2) respectively, and differences between them did not reach the statistical significance.

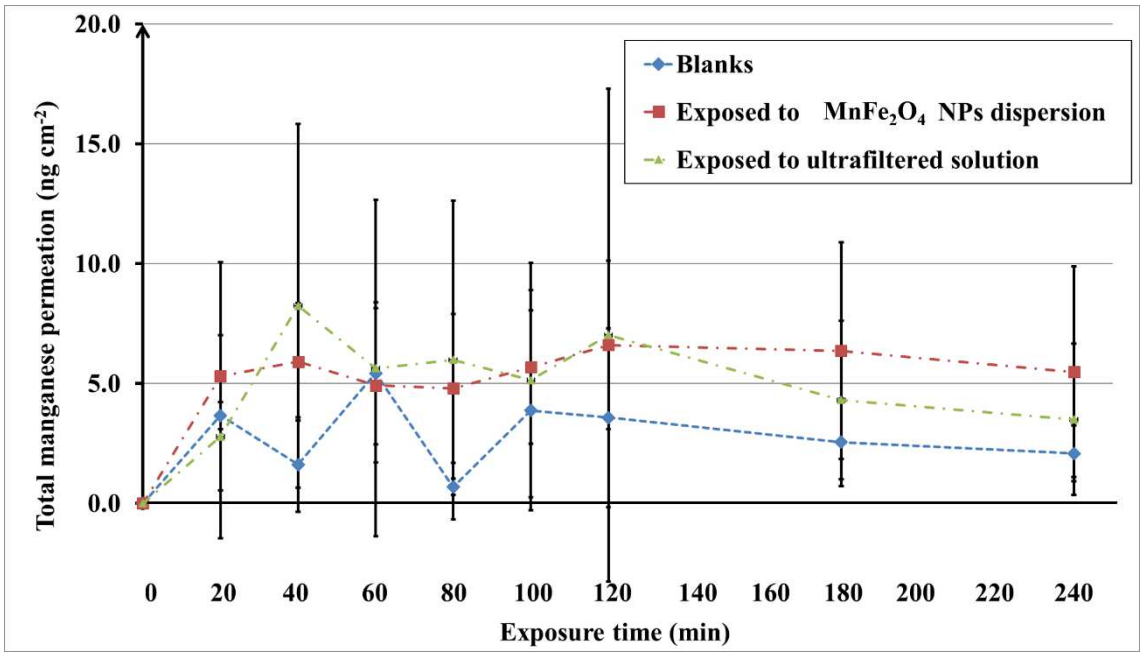

Figure 3.2.2 Manganese permeation profile in receiving phases of 4 cells exposed to $MnFe_2O_4$NPs (red) and of 4 cells exposed to $MnFe_2O_4$ ultrafiltered solution (green) and blanks (blue).

Fe concentrations were slightly higher and respectively equal to 64.4 ± 32.1 ng cm^{-2}, 59.3 ± 30.8 ng cm^{-2} and 45.9 ± 13.5 ng cm^{-2} (mean and SD) in the same cells (Fig. 3.2.3).

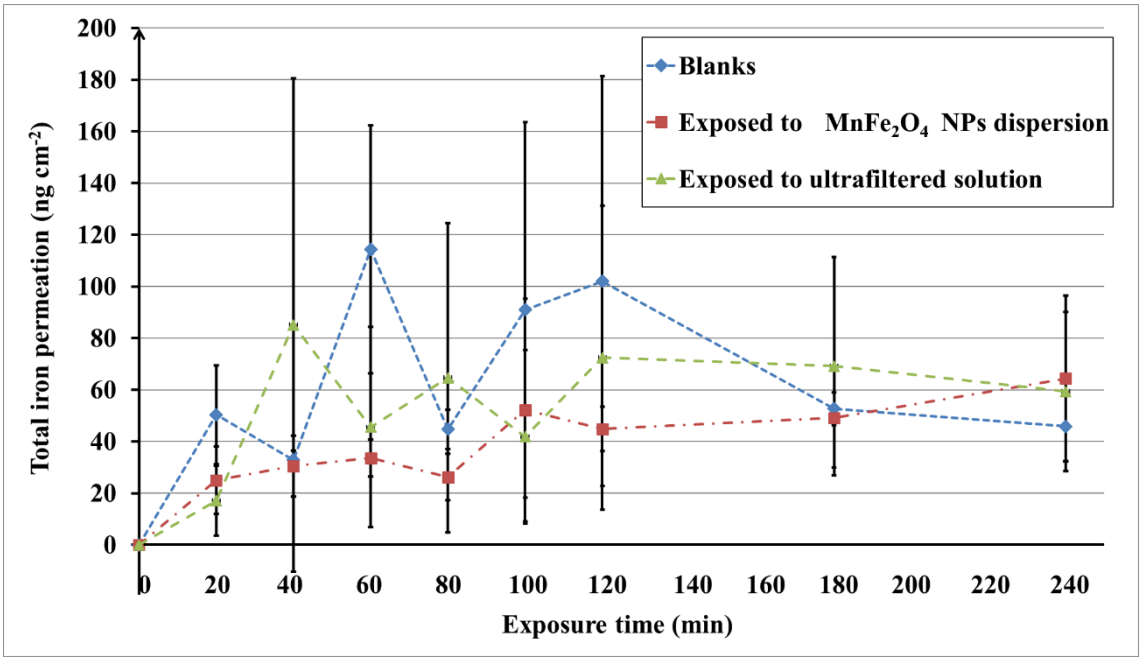

Figure 3.2.3 Iron permeation profile in receiving phases of 4 cells exposed to $MnFe_2O_4$NPs (red) and of 4 cells exposed to $MnFe_2O_4$ ultrafiltered solution (green) and blanks (blue).

Mn and Fe amounts in the tissue of cells exposed to $MnFe_2O_4$NPs were 9.36 ± 7.13 µg cm^{-2} and 19.19 ± 14.54 µg cm^{-2} respectively (Fig. 3.2.4), while no traces of both metals were detected in tissues exposed to ultrafiltered solution and in tissues of the blank cells. Only Fe concentration inside tissue exposed to $MnFe_2O_4$NPs reached statistical significance (Mann - Whitney test, p = 0.01). In cells exposed to $MnFe_2O_4$NPs the Fe concentration was double of that of Mn as expected from the Fe/Mn ratio in the nanopowder, while it was higher in the receiving solutions meaning a different source of the metals.

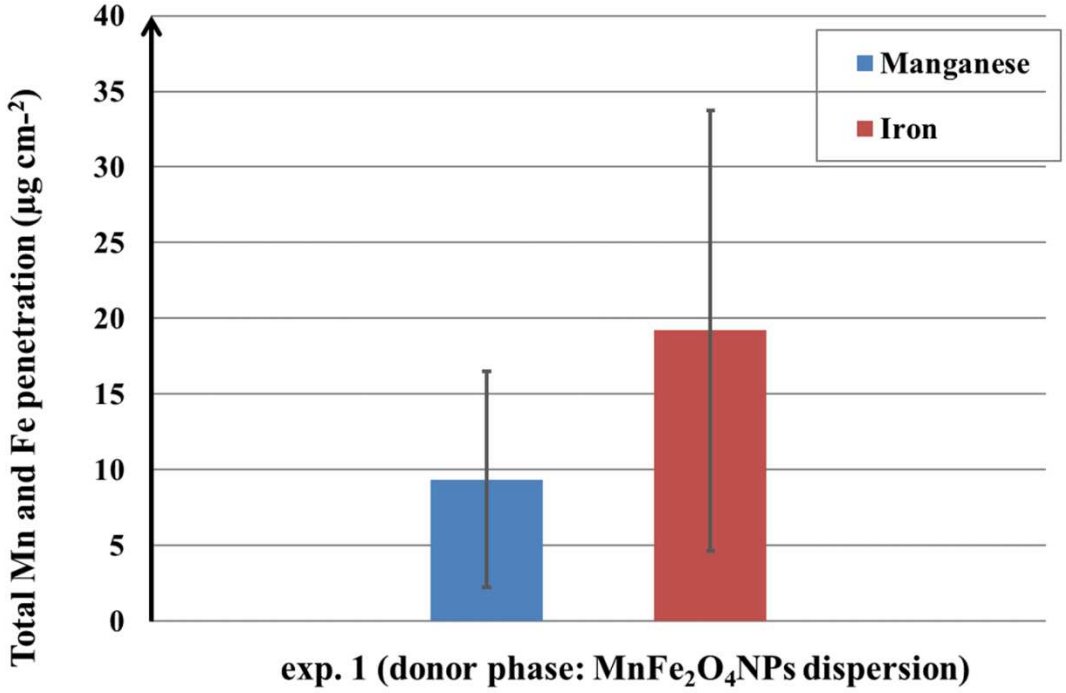

Figure 3.2.4 Manganese and iron concentration in the meninges of 4 cells exposed to $MnFe_2O_4$NPs (mean and SD).

2.4 Discussion and conclusions

Occupational exposure to Mn is likely in some professional scenarios, and can reach high concentrations under certain occupational settings, such as arc-welding (Zimmer et al., 2002), where concentrations of Mn could reach 0.01–5 mg m^{-3} (Korczynski, 2000; Li et al., 2004; Sinczuk-Walczak et al., 2001). NPs can represent a significant constituent of welding fumes (Cena et al., 2014). Usually the predominant particle size diameter resulting from welding processes is below microns (Cena et al., 2014), and these particles are generally agglomerated in chain structures and bound in compounds like $KMnF_3$, $MnFe_2O_4$ or K_2MnO_4.

Other hazardous working scenarios are represented by alloys production, rock mining activities for Mn extraction, steel and dry batteries production (Cheng et al., 2006), wastewater treatment (Cao et al., 2011) and the agricultural sector, where Mn is used as pesticides constituent (Ferraz et al., 1988).

Manganese is an essential cofactor in several human enzyme activities (ATSDR, 2000; Crowley et al., 2000), but long-term exposure to excessive levels can cause central nervous system bioaccumulation, leading to Parkinson-like symptoms (Racette et al., 2001; Antonini et al., 2006).

Inhaled NPs deposit partially in pharynx and nasopharynx and partly in the lungs, with a ratio between these fractions that increases with reducing the diameter of the NPs (International Committee on Radiological Protection, 1994; Oberdorser et al., 2009).

Given the higher surface to volume ratio compared to bulk materials, NPs can potentially interact more with biological fluids, with subsequent toxicological effects still poorly evaluated (Oberdorster et al., 2005; Li et al., 2014).

The present study investigated the permeation properties of meningeal membrane, which envelops the olfactory nerves throughout their course from the upper nasal cavity to the olfactory bulb (Valentin and Antonelli, 1844; Nieuwenhuys et al., 2010; Lochhead and Thorne, 2012), towards $MnFe_2O_4$NPs, which are commonly produced during arc welding activities.

Results shows that Mn concentrations in receiving phases of cells exposed to NPs, to ultrafiltered solution and to blank cells were similar and extremely low. Fe concentrations were slightly higher but the results were almost the same.
This means that a negligible, if any, Mn and Fe permeation occurred.

Mn is a trace element normally present in the body, therefore the amount demonstrated in blank cells receiving phases could be released from meningeal tissue. Iron, instead, is naturally present in blood.

Moreover, Mn and Fe concentration was very low in ultrafiltered donor solution, meaning that this kind of NPs do not release high amount of ions when dispersed in biological fluids. This is in line with results of other in vitro studies on metal oxide NPs permeation through biological membranes (Crosera et al., 2015; Mauro et al., 2015). Moreover, since Fe/Mn ratio in receiving solution of cells exposed to $MnFe_2O_4$NPs was higher compared to the ratio demonstrated in donor solution and inside the tissue (Fe/Mn = 2), a translocation of the NPs through meningeal membrane is definitely unlikely. A similar result was obtained in a previous study of our group on meningeal permeability towards 19 nm silver nanoparticles (Mauro et al., 2016).

In vivo studies on rats demonstrated that the olfactory neurons could serve as an entry pathway for soluble manganese compounds from the nasal mucosa to the olfactory bulb (Dorman et al., 2004; Henriksson and Tjälve, 2000; Tjälve et al., 1996; Tjälve and Henriksson, 1999) after inhalation or intranasal instillation exposures.

Lochlane and Thorne (2012) demonstrated that at least 3 different pathways exist (intracellular, paracellular and transcellular), but it is very difficult to define which one of these, if any, is more involved in NPs absorption. In a study of Elder and coworkers (2006) rats were intranasally exposed to 31 nm Mn oxide NPs for 12 days with both or one nostril patent. Results showed that traces of manganese were found only in the olfactory bulb corresponding to the pervious nostrils. They also made a comparison between intranasally instilled Mn oxide and soluble $MnCl_2$ and results, surprisingly, demonstrated similar final metal amount inside the olfactory bulb, thus making the

hypothesis unlikely that the absorption is given by a transmembrane ions passage (very low for metal oxides) and supporting the hypothesis of an active intraneuronal absorption.

Our results show that $MnFe_2O_4$ NPs meningeal permeation is negligible, confirming the hypothesis that a transcellular and paracellular absorption is far-fetched and supporting the thesis that an active intra axonal NPs transport is more likely (not tested in the study). Another issue to consider is that in *in vitro* study no active membrane uptake mechanisms could be studied, and so the role of specific receptors could not be investigated. Mn and Fe in fact compete for the transferrin receptor, which activity in case of iron deficiency may favor the entry of Mn in various brain regions (Andersen et al., 1999; Aschner et al., 1999) and which role in the meningeal membrane has not been investigated yet.
Considering the foregoing and the limitations of an *in vitro* study, our results lean towards a reassuring transmeningeal absorption profile of $MnFe_2O_4$NPs in physiological conditions.

References

ACGIH. (1987). Threshold Limit Values and Biological Exposure Indices. American Conference of Governmental Industrial Hygienists. Cincinatti, U.S.A.

Agency for Toxic Substances and Disease Registry (ATSDR). (2012). *Toxicological profile for Manganese*. Atlanta, GA: U.S. Department of Health and Human Services, Public Health Service.

Alshatwi, A. A., Vaiyapuri Subbarayan, P., Ramesh, E., Al-Hazzani, A. A., et al. (2012). Al_2O_3 nanoparticles induce mitochondria-mediated cell death and upregulate the expression of signaling genes in human mesenchymal stem cells. *J. Biochem. Mol. Toxicol*. 26(11): 469-476.

Amitrano, R. and Tortora, G. (2012). *Update: Laboratory Exercises in Anatomy and Physiology with Cat Dissections*. Cengage Learning, pp. 312.

Anane, R., Bonini, M., Grafeille, J. and Creppy, E. (1995). Skin absorption and hippocampal bioaccumulation of water soluble aluminum chloride in mice. *Hum. Exp. Toxicol*. 14: 531.

Andersen, M. E., Gearhart, J. M. and Clewell, H. J. 3rd. (1999). Pharmacokinetic data needs to support risk assessments for inhaled and ingested manganese. *Neurotoxicology*. 20(2-3): 161-171.

Andujar, P., Simon-Deckers, A., Galateau-Sallé, F., Fayard, B., et al. (2014). Role of metal oxide nanoparticles in histopathological changes observed in the lung of welders. *Part. Fibre Toxicol*. 11: 23-35.

Antonini, J. M., Santamaria, A., Jenkins, N., Albini, E., et al. (2006). Fate of manganese associated with the inhalation of welding fumes: potential neurological effects. *Neurotoxicology*. 27(3): 304-310.

Aschner, M., Guilarte, T. R., Schneider, J. S. and Zheng, W. (2007). Manganese: recent advances in understanding its transport and neurotoxicity. *Toxicol. Appl. Pharmacol*. 221: 131‑147.

Aschner, M., Vrana, K. E. and Zheng, W. (1999). Manganese uptake and distribution in the central nervous system (CNS). *Neurotoxicology*. 20(2-3): 173-180.

Balasubramanyam, A., Sailaja, N., Mahboob, M., Rahman, M. F., et al. (2010). In vitro mutagenicity assessment of aluminium oxide nanomaterials using the Salmonella/microsome. *Toxicol. In Vitro*. 24(6): 1871-1876.

Bémer, D., Régnier, R., Subra, I., Sutter, B., et al. (2010). Ultrafine particles emitted by flame and electric arc guns for thermal spraying of metals. *Ann. Occup. Hyg*. 54: 607–614.

Blank, I. H., Jones, J. L. and Gould, E. (1958). A study of the penetration of Aluminium salts into excised human skin. *Proc. Sci. Sect. Toilet Goods Assoc*. 29: 32-35.

Bowler, R. M., Gocheva, V., Harris, M., Ngo, L., et al. (2011). Prospective study on neurotoxic effects in manganese-exposed bridge construction welders. *Neurotoxicology*. 32(5): 596-605.

Bowler, R. M., Gysens, S., Diamond, E., Nakagawa, S., et al. (2006). Manganese exposure: neuropsychological and neurological symptoms and effects in welders. *Neurotoxicology*. 27(3): 315-326.

Bronaugh, R. and Steward, R. (1985). Methods for in vitro percutaneous absorption studies V: Permeation through damaged skin. *J. Pharm. Sci*. 15: 1062–1066.

Butterworth, J. (1986). Changes in nine enzyme markers for neurons, glia, and endothelial cells in agonal state and Huntington's, disease caudate nucleus. *J. Neurochem*. 47: 583‑587.

Campdelacreu, J. (2014). Parkinson disease and Alzheimer disease: environmental risk factors. *Neurologia*. 29(9): 541-549.

Canli, E. G., Atli, G. and Canli, M. (2017). Response of the antioxidant enzymes of the erythrocyte and alterations in the serum biomarkers in rats following oral administration of nanoparticles. *Environ. Toxicol. Pharmacol*. 50: 145-150.

Cao, J., Mao, Q. H., Shi, L. and Qian, Y. T. (2011). Fabrication of γ-MnO_2/α- MnO_2 hollow core/shell structures and their application to water treatment. *J. Mater. Chem*. 21: 16210–16215.

Cena, L. G., Keane, M. J., Chisholm, W. P., Stone, S., et al. (2014). A novel method for assessing respiratory deposition of welding fume nanoparticles. *J. Occup. Environ. Hyg*. 11(12): 771-780.

Cerosimo, M. G. and Koller, W. C. (2006). The diagnosis of manganeseinduced Parkinsonism. *Neurotoxicology*. 27: 340‑346.

Cheng, F. Y., Zhao, J. Z., Song, W., Li, C., et al. (2006). Facile controlled synthesis of MnO_2 nanostructures of novel shapes and their application in batteries. *Inorg. Chem*. 45: 2038–2044.

CIR, *Cosmetic Ingredient Review, Safety Assessment of Alumina and Aluminum Hydroxide as Used in Cosmetics*. Final report 2014.

Colvin, V. L. (2003). The potential environmental impact of engineered nanomaterials. *Nat. Biotechnol*. 21(10): 1166 – 1170.

Crosera, M., Adami, G., Mauro, M., Bovenzi, et al. (2016). In vitro dermal penetration of nickel nanoparticles. *Chemosphere*. 145: 301-306.

Crosera, M., Prodi, A., Mauro, M., Pelin, M., et al. (2015). Titanium Dioxide Nanoparticle Penetration into the Skin and Effects on HaCaT Cells. *Int. J. Environ. Res. Public Health*. 12(8): 9282-9297.

Crowley, J. D., Traynor, D. A. and Weatherburn, D. C. (2000). In: A. Sigel, H. Sigel (Eds.), *Metal Ions in Biological Systems*, vol. 37, Marcel Dekker, Inc., New York, pp. 209–278.

Curwin, B. and Bertke, S. (2011). Exposure characterization of metal oxide nanoparticles in the workplace. *J. Occup. Environ. Hyg*. 8: 580–587.

Darbre, P. D. (2005). Aluminium, antiperspirants and breast cancer. *J. Inorg. Biochem*. 99(9): 1912-1919.

Dasch, J. and D'Arcy, J. (2008). Physical and chemical characterization of airborne particles from welding operations in automotive plants. *J. Occup. Environ. Hyg*. 5: 444–454.

Davies, D. J., Ward, R. J. and Heylings, J. R. (2004). Multi-species assessment of electrical resistance as a skin integrity marker for in vitro percutaneous absorption studies. *Toxicol. In Vitro*. 18(3): 351–358.

Demir, E., Burgucu, D., Turna, F., Aksakal, S., et al. (2013). Determination of TiO_2, ZrO_2, and Al_2O_3 nanoparticles on genotoxic responses in human peripheral blood lymphocytes and cultured embyronic kidney cells. *J. Toxicol. Environ. Health A*. 76(16): 990-1002.

Di Virgilio, A. L., Reigosa, M. and de Mele, M. F. (2010). Response of UMR 106 cells exposed to titanium oxide and aluminum oxide nanoparticles. *J. Biomed. Mater. Res. A*. 92(1): 80-86.

Dinman, B. D. (1987). Aluminum in the lung: the pyropowder conundrum. *J. Occup. Med*. 29: 869–876.

Dorman, D. C., McManus, B. E., Parkinson, C. U., Manuel, C. A., et al. (2004). Nasal toxicity of manganese sulfate and manganese phosphate in young male rats following subchronic (13-week) inhalation exposure. *Inhal. Toxicol*. 16: 481–488.

Elder, A., Gelein, R., Silva, V., Feikert, T., et al. (2006). Translocation of inhaled ultrafine manganese oxide particles to the central nervous system. *Environ. Health Perspect*. 114(8): 1172-1178.

Ellingsen, D. G., Konstantinov, R., Bast-Pettersen, R., Merkurjeva, L., et al. (2008). A neurobehavioral study of current and former welders exposed to manganese. *Neurotoxicology*. 29(1): 48-59.

Erikson, K. M. and Aschner, M. (2003). Manganese neurotoxicity and glutamate-GABA interaction. *Neurochem. Int*. 43: 475–480.

Ferraz, H. B., Bertolucci, P. H., Pereira, J. S., Lima JG, Andrade, L. A. (1988). Chronic exposure to the fungicide maneb may produce symptoms and signs of CNS manganese intoxication. *Neurology*. 38: 550–553.

Flarend, R., Bin, T., Elmore, D. and Hem S. L. (2001). A preliminary study of the dermal absorption of aluminum from antiperspirants using aluminum-26. *Food Chem. Toxicol*. 39: 163-168.

Flynn, M. R. and Susi, P, (2009). Neurological risks associated with manganese exposure from welding operations—a literature review. *Int. J. Hyg. Environ. Health*. 212: 459–469.

Franz, T. J. (1975). On the relevance of in vitro data. *J. Invest. Dermatol*. 93: 633-640.

Gomes, J. F., Albuquerque, P. C., Miranda, R. M, Santos, T. G., et al. (2012b). Comparison of deposited surface area of airborne ultrafine particles generated from two welding processes. *Inhal. Toxicol*. 24: 774–781.

Gomes, J. F., Albuquerque, P. C., Miranda, R. M. and Vieira, M. T. (2012a). Determination of airborne nanoparticles from welding operations. *J. Toxicol. Environ. Health A*. 75: 747–755.

Groenen, M. A., Archibald, A. L., Uenishi, H., Tuggle, C. K., et al. (2012). Analyses of pig genomes provide insight into porcine demography and evolution. *Nature.* 491: 393–398.

Guillard, O., Fauconneau, B., Olichon, D., Dedieu, G., et al. (2004). Hyperaluminemia in a woman using an aluminum-containing antiperspirant for 4 years. *Am. J. Med*. 117(12): 956-959.

Hall, A. F. Occupational contact dermatitis among aircraft workers. (1944). *J. Am. Med. Assoc*. 125: 179–185.

Hashimoto, M. and Imazato, S. (2015). Cytotoxic and genotoxic characterization of aluminum and silicon oxide nanoparticles in macrophages. *Dent. Mater*. 31(5): 556-564.

Henriksson, J. and Tjälve, H. (2000). Manganese taken up into the CNS via the olfactory pathway in rats affects astrocytes. *Toxicol. Sci*. 55: 392–398.

Hong, S. H. and Kim, B. K. (2002). Effects of lifter bars on the ball motion and aluminum foil milling in tumbler ball mill. *Mater. Lett*. 57: 275–279.

Hostynek, J. J., Hinz, R. S., Lorence, C. R., Price, M. et al. (1993). Metals and the skin. *Crit. Rev. Toxicol*. 23: 171–235.

Ingersoll, R. T., Montgomery, E. B. and Aposhian, H. V. (1999). Central nervous system toxicity of manganese. II: Cocaine or reserpine inhibit manganese concentration in the rat brain. *Neurotoxicology*. 20(2‑3): 467‑476.

International Committee on Radiological Protection. (1994). *Human Respiratory Tract Model for Radiological Protection*. Oxford, UK. Pergamon Press.

Ivask, A., Titma, T., Visnapuu, M., Vija, H., et al. (2015). Toxicity of 11 Metal Oxide Nanoparticles to Three Mammalian Cell Types In Vitro. *Curr. Top. Med. Chem*. 15(18): 1914-1929.

Johannessen, H. and Bergan-Skar, B. (1980). Itching problems among potroom workers in factories using recycled alumina. *Contact Dermatitis*. 6: 42-43.

Katsnelson, B. A., Minigaliyeva, I. A., Panov, V. G., Privalova, L. I., et al. (2015). Some patterns of metallic nanoparticles' combined subchronic toxicity as exemplified by a combination of nickel and manganese oxide nanoparticles. *Food Chem. Toxicol*. 86: 351-364.

Killin, L. O., Starr, J. M., Shiue, I. J. and Russ, T. C. (2016). Environmental risk factors for dementia: a systematic review. *BMC Geriatr*. 16(1): 175.

Kim, I. S., Baek, M. and Choi, S. J. (2010). Comparative cytotoxicity of Al_2O3, CeO_2, TiO_2 and ZnO nanoparticles to human lung cells. *J. Nanosci. Nanotechnol*. 10(5): 3453-3458.

Koponen, I. K., Jensen, K. A. and Schneider, T. (2010). Comparison of dust released from sanding conventional and nanoparticle-doped wall and wood coatings. *J. Expos. Sci. Environ. Epidemiol*. 21: 450–463.

Korczynski, R. E. (2000). Occupational health concerns in the welding industry. *Appl. Occup. Environ. Hyg*. 15(12): 936–945.

Krewski, D., Yokel, R. A., Nieboer, E., Borchelt, D., et al. (2007). Human health risk assessment for aluminium, aluminium oxide, and aluminium hydroxide. *J. Toxicol. Environ. Health B Crit. Rev.* 10(1): 1-269.

Kreyling, W. G., Semmler-Behnke, M. and Möller, W. (2006). Ultrafine particle–lung interactions: does size matter? *J. Aerosol Med*. 19: 74–83.

Krízek, M., Senft, V. and Motán, J. (1997). Aluminum and the human body. *Cas Lek Cesk*. 136(17): 544-547.

Lansdown, A. B. (1973). Production of epidermal damage in mammalian skins by some simple aluminum compounds. *Br. J. Dermatol*. 89: 67–76.

Larese Filon, F., Crosera, M., Mauro, M., Baracchini, E., et al. (2016). Palladium nanoparticles exposure: Evaluation of permeation through damaged and intact human skin. *Environ. Pollut*. 214: 497-503.

Larese Filon, F., Mauro, M., Adami, G., Bovenzi, M. and Crosera, M. (2015) Nanoparticles skin absorption: New aspects for a safety profile evaluation. *Regul. Toxicol. Pharmacol*. 72(2): 310-322.

Lestari, M. L., Nicolazzo, J. A. and Finnin, B. C. (2009). A novel flow through diffusion cell for assessing drug transport across the buccal mucosa in vitro. *J. Pharm. Sci*. 98(12): 4577–4588.

Li, H., Li, Y., Jiao, J. and Hu, H. M. (2011). Alpha-alumina nanoparticles induce efficient autophagy-dependent cross-presentation and potent antitumor response. *Nature Nanotechnol*. 6: 645–650.

Li, T., Shi, T., Li, X., Zeng, S., et al. (2014). Effects of nano-MnO_2 on dopaminergic neurons and the spatial learning capability of rats. *Int. J. Environ. Res. Public. Health*. 11: 7918–7930.

Lochhead, J. J. and Thorne, R. G. (2012). Intranasal delivery of biologics to the central nervous system. *Adv. Drug. Deliv. Rev*. 64(7): 614-628.

Ma, R., Bando, Y., Zhang, L. and Sasaki, T. (2004). Layered MnO_2 nanobelts: hydrothermal synthesis and electrochemical measurement. *Adv. Mater*. 16: 918–922.

Maher, B., Ahmed, I., Karloukovski, V., Mac Laren, D., et aL. (2016). Magnetite pollution nanoparticles in the human brain. *PNAS*. 113(39): 10797-10801.

Mauro, M., Crosera, M., Bianco, C., Adami, G., et al. (2015). Permeation of platinum and rhodium nanoparticles through intact and damaged human skin. *J. Nanopart. Res*. 17: 253.

Mauro, M., Crosera, M., Bovenzi, M., Adami, G. and Filon, F. (2016). Pilot study on in vitro silver nanoparticles permeation through meningeal membrane. *Colloids Surf. B. Biointerfaces*. 146: 245-249.

Mauro, M., Crosera, M., Pelin, M., Florio, C., et al. (2015). Cobalt Oxide Nanoparticles: Behavior towards Intact and Impaired Human Skin and Keratinocytes Toxicity. *Int. J. Environ. Res. Public Health*. 12(7): 8263-8280.

McDowell, I. (2001). Alzheimer's disease: insights from epidemiology. *Aging (Milano)*. 13(3): 143-162.

Meda, L., Marra, G., Galfetti, L., Inchingalo, S., et al. (2004). Nano-composites for rocket and solid propellants. *Compos. Sci. Technol*. 65: 769-773.

Mirshafa, A., Nazari, M., Jahani, D. and Shaki, F. (2017). Size-Dependent Neurotoxicity of Aluminum Oxide Particles: a Comparison Between Nano- and Micrometer Size on the Basis of Mitochondrial Oxidative Damage. *Biol. Trace Elem. Res*. doi: 10.1007/s12011-017-1142-8.

Monteiro-Riviere, N. A., Oldenburg, S. J. and Inman, A. O. (2010). Interactions of aluminum nanoparticles with human epidermal keratinocytes. *J. Appl. Toxicol*. 30: 276–285.

Najafpour, M. M., Pashaei, B. and Nayeri, S. (2012). Nano-sized layered aluminum or zinc-manganese oxides as efficient water oxidizing catalysts. *Dalton Trans*. 41: 7134–7140.

Nieuwenhuys, R., Voogd, J. and van Huijzen, C. (2010). *The Central Nervous System*. Springer-Verlag, Italy. pp. 97.

Oberdorster, G. (2001). Pulmonary effects of inhaled ultrafine particles. *Int. Arch. Occup. Environ. Health*. 74:1–8.

Oberdörster, G., Elder, A. and Rinderknecht, A. (2009). Nanoparticles and the brain: cause for concern? *J. Nanosci. Nanotechnol*. 9(8): 4996-5007.

Oberdörster, G., Oberdörster, E. and Oberdörster, J. (2005). Nanotoxicology: an emerging discipline evolving from studies of ultrafine particles. *Environ. Health Perspect*. 113(7): 823-839.

Ordonez-Librado, J. L., Guiterrez-Valdez, A. L., Colin-Baranque, L., Anaya-Martinez, V., et al. (2008). Manganese inhalation as a Parkinson disease model. *Neuroscience*. 155: 7‑11.

Pal, P. K., Samii, A. and Calne, D. B. (1999). Manganese neurotoxicity: a review of clinical features, imaging and pathology. *Neurotoxicology*. 20: 227–238.

Park, E, J., Lee, G. H., Yoon, C., Jeong, U., et al. (2017). Tissue distribution following 28 day repeated oral administration of aluminum-based nanoparticles with different properties and the in vitro toxicity. *J. Appl. Toxicol*. 37(12): 1408-1419.

Patra, A. K., Dutta, A. and Bhaumik, A. (2012). Self-assembled mesoporous γ-Al_2O_3 spherical nanoparticles and their efficiency for removal of arsenic from water. *J. Hazard. Mater*. 201-202: 170-177.

Pfefferkorn, F. E., Bello, D., Haddad, G., Park, J. Y., et al. (2010). Characterization of exposures to nanoscale particles during friction stir welding of aluminum. *Ann. Occup. Hyg*. 54: 486–503.

Pineau, A., Guillard, O., Favreau, F., Marrauld, A., et al. (2012). In vitro study of percutaneous absorption of aluminum from antiperspirants through human skin in the Franz™ diffusion cell. *J. Inorg. Biochem*. 110: 21-26.

Purello-D'Ambrosio, F., Gangemi, S., Minciullo, P. L., Lombardo, G., et al. (2000). Aluminium allergy in a patient with occupational contact dermatitis. *Allergol. Immunopathol. (Madr)*. 28(2): 74-75.

Putterman, G. J., Strassburger, J. and Fitzgerald, J. J. (1981). In vitro sorption of aluminum complex to guinea pig stratum corneum. *J. Invest. Dermatol*. 77: 319-324.

Quartrale, R. P. (1988). *The mechanism of antiperspirant action in eccrine sweat glands*. In: Laden, K., Felger, C. B., editors. New York: Marcel Dekker. p. 89–118.

Quatrale, R., Coble, D., Stoner, K. and Felger, C. (1981). The mechanism of antiperspirant action by aluminum salts. II. Histological observation of human eccrine sweat glands inhibited by aluminum chlorohydrate. *J. Soc. Cos. Chem*. 32: 107-136.

Quintanar, L. (2008). Manganese neurotoxicity: a bioinorganic chemist's perspective. *Inorg. Chim. Acta*. 361: 875–884.

Racette, B. A., McGee-Minnich, L., Moerlein, S. M., Mink, J. W., et al. (2001). Welding-related parkinsonism. Clinical features, treatment, and pathophysiology. *Neurol*. 56: 8–13.

Radzium, E., Dudkiewicz-Wilczyńska, J., Ksiazek, I., Nowak, K., et al. (2011) Assessment of the cytotoxicity of aluminum oxide nanoparticles on selected mammalian cells. *Toxicol. In Vitro*. 25: 1694–1700.

Rajeshwari, A., Kavitha, S., Alex, S. A., Kumar, D., et al. (2015). Cytotoxicity of aluminum oxide nanoparticles on Allium cepa root tip--effects of oxidative stress generation and biouptake. *Environ. Sci. Pollut. Res. Int*. 22(14): 11057-11066.

Rajiv, S., Jerobin, J., Saranya, V., Nainawat, M., et al. (2016). Comparative cytotoxicity and genotoxicity of cobalt (II, III) oxide, iron (III) oxide, silicon dioxide, and aluminum oxide nanoparticles on human lymphocytes in vitro. *Hum. Exp. Toxicol*. 35(2): 170-183.

Rao, D. B., Wong, B. A., McManus, B. E., McElveen, A. M., et al. (2003). Inhaled iron, unlike manganese, is not transported to the rat brain via the olfactory pathway. *Toxicol. Appl. Pharmacol*. 193(1): 116-26.

Royal Society & Royal Academy of Engineering. (2004). *Nanoscience and nanotechnologies: opportunities and uncertainties*. The Royal Society, London.

Sadiq, R., Khan, Q. M., Mobeen, A. and Hashmat, A. J. (2015). In vitro toxicological assessment of iron oxide, aluminium oxide and copper nanoparticles in prokaryotic and eukaryotic cell types. *Drug. Chem. Toxicol*. 38(2): 152-161.

Sinczuk-Walczak, H., Jacubowski, M. and Matczak, W. (2001). Neurological and neurophysiological examinations of workers occupationally exposed to manganese. *Int. J. Occup. Med. Environ. Health*. 14(4): 329–337.

Srikanth, K., Mahajan, A., Pereira, E., Duarte, A. C., et al. (2015). Aluminium oxide nanoparticles induced morphological changes, cytotoxicity and oxidative stress in Chinook salmon (CHSE-214) cells. *J. Appl. Toxicol*. 35(10): 1133-1140.

Stadler, T., Buteler, M. and Weaver, D. K. (2010). Novel use of nanostructured alumina as an insecticide. *Pest. Manag. Sci*. 66: 577–579.

Stefanescu, D. M., Khoshnan, A., Patterson, P. H. and Hering, J. G. (2009). Neurotoxicity of manganese oxide nanomaterials. *J. Nanopart. Res*. 11: 1957–1969.

Stokinger, H. E. (1981). *The metals - aluminum*. In: G. D. Clayton and F. E. Clayton. *Patty's Industrial Hygiene and Toxicology*, 3rd ed. John Wiley and Sons, Toronto, Canada.

Tjälve, H. and Henriksson, J. (1999). Uptake of metals in the brain via olfactory pathways. *Neurotoxicology*. 20(2–3): 181–196.

Tjälve, H., Henriksson, J., Tallkvist, J., Larsson, B. S., et al. (1996). Uptake of manganese and cadmium from the nasal mucosa into the central nervous system via olfactory pathways in rats. *Pharmacol. Toxicol*. 79: 347–356.

Tomljenovic, L. (2011). Aluminium and Alzheimer's disease: after a century of controversy, is there a plausible link? *J. Alzheimer's Dis*. 23: 567–598.

Trunov, M. A., Schoenitz, M., Zhu, X. and Dreizin, E. L. (2005). Effect of polymorphic phase transformations in Al_2O_3 film on oxidation kinetics of aluminum powders. *Combust. Flame*. 140: 310-318.

Tsaousi, A., Jones, E., Case and C. P. (2010). The in vitro genotoxicity of orthopaedic ceramic (Al_2O_3) and metal (CoCr alloy) particles. *Mutat. Res*. 697(1-2): 1-9.

Valentin, G., Antonelli, G. (Ed.). (1844). *Treaty of Neurology*: First Italian translation by MG Dr., Levi Medical. Venice, pp. 220–228.

Van Oostdam, J. C., Zwanenburg, H. and Harrison, J. R. (1990). Canadian perspectives on aluminum. *Environ. Geochem. Health*. 12(1-2): 71-74.

Zhang, Q., Wang, H., Ge, C., Duncan, J., et al. (2017). Alumina at 50 and 13 nm nanoparticle sizes have potential genotoxicity. *J. Appl. Toxicol*. 37(9): 1053-1064.

Zhang, X. Q., Yin, L. H., Tang, M. and Pu, Y. P. (2011). ZnO, TiO_2, SiO_2 and Al_2O_3 nanoparticles-induced toxic effects on human fetal lung fibroblasts. *Biomed. Environ. Sci*. 24(6): 661-669.

Zimmer, A. T., Baron, P. A. and Biswas, P. (2002). The influence of operating parameters on number-weighted aerosol size distribution generated from a gas metal arc welding process. *J. Aerosol Sci*. 33: 519–531.

Conclusions

In this thesis UFPs found in working environments and ambient air were measured, characterised and, afterwards, possible exposure routes were explored. This can help enhancing knowledge on diseases that may be related to this kind of exposure.

In the first section two studies about the characterisation of ultrafine and submicron particles in working environments were presented.

In the first study morpho-chemical characteristics of Gas Tungsten Arc Welding (GTAW) fumes particles were determined by means of TEM-EDS. Differences between particles produced by an automatic and a manual process performed in an automotive plant were highlighted. The particles sampled during the automatic GTAW process were mainly constituted by iron/manganese oxide with a mean diameter of 47 nm, followed by smaller iron oxide nanoparticles (21 nm on average). During the manual welding process aggregates with larger diameters that showed an X-ray spectrum characteristic of different kinds of silicates were found as prominent. This study confirms that welders are exposed to ultrafine and submicron particles and that iron/manganese oxide nanoparticles are the most representative in automatic process, despite the low concentration of manganese in welding wires (about 1-2%).

After this first study a more comprehensive approach was used to assess the exposure of workers to ultrafine and submicron particles in three industrial settings where aluminium was used as raw material in different manufacturing processes. An integrated approach including air monitoring and the evaluation of skin and surface contamination was used in real workplace conditions. Our results showed exposure levels lower than the ACGIH limits for respirable aluminium (1 mg m^{-3}) in workplace air. However, our data

demonstrated that oxy-fuel welding and the die casting production cycle of aluminium products involve the release of UFPs with a chemical composition coherent with the raw materials. Even if agglomerates/aggregates of nanoparticles were present, a tendency to the aggregation in larger non-nano scaled aggregates were observed on working surfaces. Although we cannot exclude that Al could be contained in agglomerates of nanoparticles on the aluminium-contaminated skin of workers, surfaces and skin contamination seems to be a secondary source of exposure to UFPs, suggesting a possible increased risk mainly for inhalation in workers.

Regarding the evaluation of the presence of UFPs in ambient air, a study performed in proximity of an industrial "hot spot" in Servola district in Trieste where an integral cycle steel plant is located, was reported in the second section of this work. A "background" site, where UFPs emission from anthropogenic sources was expected to be minimum, was used to make a comparison.

In "Servola" site number concentration of particles in the range 10-300 nm was about twice higher than "background" values. Moreover an increase of the particle number concentration corresponding to a decrease of the particle size and vice versa was observed. ED-μXRF analysis performed on filters sampled in "Servola" site showed the presence of Fe, Zn and Mn in the particulate matter. The same elements constituted agglomerates of nanoparticles observed by means of TEM-EDS and they were those with a concentration higher than the limit of detection in the quantitative analysis performed using ICP-AES. The contribution of Fe concentration in the PM_1 and, in particular, in the particle fraction below 250 nm seems to be not negligible. This result is highly significant from a toxicological point of view. Servola district is densely inhabited and people live very close to the integrated steel plant.

Afterwards, in the third section, nanoparticles compatible with those found in the aforementioned studies were tested *in vitro* using the method of static Franz diffusion cells (Franz, 1975) in order to explore possible exposure routes.

Transdermal absorption of Al_2O_3 nanoparticles was evaluated and, albeit with the limitations due to the *in vitro* test procedure which cannot take into account any active uptake mechanism, our study supports the hypothesis of a reassuring permeation profile.

In a second study transmeningeal absorption of $MnFe_2O_4$ nanoparticles was investigated in order to clarify the possible role of meningeal membranes in the mechanisms of absorption of metal oxides NPs through the olfactory route. Our results show that $MnFe_2O_4$ meningeal permeation is negligible, confirming the hypothesis that a transcellular and paracellular absorption is far-fetched while an active intra axonal NPs transport from the nasal mucosa to the olfactory bulb is more likely.

In conclusion, all the aforementioned studies underline the importance of evaluating the presence of UFPs both in ambient air and in working environments. Our results confirm that the measure of metals mass concentration in the particulate matter is not enough when considering UFPs. Other parameters such as particle number concentration, size and morpho-chemical characteristics of UFPs should be evaluated.

We demonstrated that in some workplaces, besides inhalation, surfaces and skin contamination can be a secondary source of exposure to UFPs for workers highlighting the importance of studying all possible exposure routes.

Acknowledgments

I would like to thank the “Commissariato del Governo nella Regione Friuli Venezia Giulia” (“Fondo Trieste”) that funded this doctoral research.

Thanks to prof. Larese (Dipartimento Universitario Clinico di Scienze Mediche Chirurgiche e della Salute, Università di Trieste), prof. Belluso (Dipartimento di Scienze della Terra, Università di Torino) and prof. Canton (Dipartimento di Scienze Molecolari e Nanosistemi, Università Ca’ Foscari Venezia) for the scientific collaboration during these years.

Appendix – Scientific Contributions

Scientific publications

E. Baracchini, C. Bianco, M. Crosera, F. Larese Filon, E. Belluso, S. Capella, G. Maina, G. Adami, Nano- and Submicron Particles Emission during Gas Tungsten Arc Welding (GTAW) of Steel: Differences between Automatic and Manual Process, *Aerosol and Air Quality Research* (2017), DOI: 10.4209/AAQR.2017.07.0226.

E. Pavoni, S. Covelli, G. Adami, E. Baracchini, R. Cattelan, M. Crosera, P. Higueras, D. Lenaz, E. Petranich, Mobility and fate of Thallium and other potentially harmful elements in drainage waters from a decommissioned Zn-Pb mine (North-Eastern Italian Alps), *Journal of Geochemical Exploration* (https://doi.org/10.1016/j.gexplo.2018.01.005).

L. Fortuna, E. Baracchini, G. Adami, M. Tretiach, Melanization Affects the Content of Selected Elements in Parmelioid Lichens, *Journal of Chemical Ecology* (2017), (https://doi.org/10.1007/S10886-017-0899-8).

E. Pavoni, E. Petranich, G. Adami, E. Baracchini, M. Crosera, A. Emili, D. Lenaz, P. Higueras, S. Covelli, Bioaccumulation of thallium and other trace metals in Biscutella laevigata nearby a decommissioned zinc-lead mine (Northeastern Italian Alps), *Journal of Environmental Management* (2016), DOI: 10.1016/j.jenvman.2016.07.022.

F. Larese Filon, M. Crosera, M. Mauro, E. Baracchini, M. Bovenzi, T. Montini, P. Fornasiero, G. Adami, Palladium nanoparticles exposure: Evaluation of permeation through damaged and intact human skin, *Environmental Pollution* (2016), 214, 497-503. DOI: 10.1016/j.envpol.2016.04.077.

M. Crosera, G. Adami, M. Mauro, M. Bovenzi, E. Baracchini, F. Larese Filon, In vitro dermal penetration of nickel nanoparticles, *Chemosphere* (2016), 145, 301-306. DOI:10.1016/j.chemosphere.2015.11.076.

G. Adami, A. Gorassini, E. Prenesti, M. Crosera, E. Baracchini, A. Giacomello, Micro-XRF and FT-IR/ATR analyses of an optically degraded ancient document of the Trieste (Italy) cadastral system (1893): A novel and surprising iron gall ink protective action, *Microchemical Journal* (2016), 124, 96–103. DOI:10.1016/j.microc.2015.07.020.

Other scientific contributions

E. Baracchini, M. Crosera, B. Callegher, E. Prenesti, G. Adami, Analytical investigation on archaeological patina: a tool to shed light on the provenance of ancient bronze coins. XXVI Congresso Nazionale della Società Chimica Italiana (SCI). Paestum (SA), 10-14 settembre 2017. Poster. Presenting author: Matteo Crosera.

M. Crosera, M. Mauro, E. Baracchini, M. Bovenzi, F. Larese, G. Adami, In vitro meningeal permeation of $MnFe_2O_4$ nanoparticles. XXVI Congresso Nazionale della Società Chimica Italiana (SCI). Paestum (SA), 10-14 settembre 2017. Oral. Presenting author: Matteo Crosera.

E. Petranich, S. Croce, M. Crosera, E. Baracchini, E. Pavoni, A. Acquavita, J. Faganeli, S. Covelli, G. Adami, Mobility of trace elements at the sediment-water interface in two tourist port areas of the gulf of Trieste (Northern Adriatic Sea). XXVI Congresso Nazionale della Società Chimica Italiana (SCI). Paestum (SA), 10-14 settembre 2017. Poster. Presenting author: Matteo Crosera.

E. Baracchini, A. Prodi, M. Crosera, P. Canton, F. Larese Filon, G. Adami, Assessment of exposure to submicron and ultrafine particles during aluminium welding: an integrated approach for sampling and characterization. Convegno scientifico: "I giovani e la Chimica in Friuli Venezia Giulia" organizzato dalla Sezione Friuli Venezia Giulia della Società Chimica Italiana (SCI). Trieste 29 settembre 2016. Oral. Presenting author: Elena Baracchini.

E. Baracchini, A. Prodi, M. Crosera, P. Canton, F. Larese Filon, G. Adami, Sampling and characterization of submicron and ultrafine particles: an integrated approach in the exposure assessment during aluminium welding process. XXVI Congresso della Divisione di Chimica Analitica della Società Chimica Italiana (SCI). Giardini Naxos (ME) 18-22 settembre 2016. Oral. Presenting author: Elena Baracchini.

M. Crosera, M. Venier, J. Guo, A. Phillips, H. Stapleton, F. Filon Larese, E. Baracchini, G. Adami, Percutaneous absorption of flame retardants, XXVI Congresso della Divisione di Chimica Analitica della Società Chimica Italiana (SCI). Giardini Naxos 18-22 settembre 2016. Oral. Presenting author: Matteo Crosera.

L. Fortuna, J. Di Sarro, E. Baracchini, M. Crosera, G. Adami, M. Tretiach, The influence of melanins on iron accumulation in parmelioid lichens. The 8th IAL Symposium Lichens in Deep Time. Helsinki, Finland 1–5 agosto 2016. Poster. Presenting author: Lorenzo Fortuna.

C. Bianco, E. Belluso, E. Baracchini, S. Capella, V. Passini, M. Crosera, G. Adami, F. Larese Filon, Sampling and characterization of micro- and nanoparticles from Gas Tungsten Arc Welding (GTAW) fumes. XXV Congresso della Divisione di Chimica

Analitica della Società Chimica Italiana (SCI). Trieste 13-17 settembre 2015. Oral. Presenting author: Elena Baracchini.

G. Adami, A. Gorassini, E. Prenesti, M. Crosera, E. Baracchini, A. Giacomello, Chemical analysis of optically degraded documents of the Trieste cadastral system (1893): a surprising iron gall ink protective action. XXV Congresso della Divisione di Chimica Analitica della Società Chimica Italiana (SCI). Trieste 13-17 settembre 2015. Poster. Presenting author: Gianpiero Adami.

J. Di Sarro, L. Fortuna, E. Baracchini, M. Crosera, M. Tretiach, G. Adami, Iron distribution in lichens with different levels of melanization: a study by means of micro-XRF and ICP-AES. XXV Congresso della Divisione di Chimica Analitica della Società Chimica Italiana (SCI). Trieste 13-17 settembre 2015. Poster. Presenting author: Jessica Di Sarro.

E. Pavoni, E. Petranich, M. Crosera, G. Adami, E. Baracchini, M. Rusalen, D. Lenaz, A. Emili, P. Higueras, S. Covelli, Bioaccumulation of trace metals in plants growing nearby a decommisioned Zn-Pb mine (Salafossa, northeastern Italian Alps). XXV Congresso della Divisione di Chimica Analitica della Società Chimica Italiana (SCI). Trieste 13-17 settembre 2015. Poster. Presenting author: Elisa Petranich.